

ENSURING LARGE-DISPLACEMENT STABILITY IN AC MICROGRIDS

A Dissertation

Submitted to the Faculty

of

Purdue University

by

Thomas Craddock

In Partial Fulfillment of the

Requirements for the Degree

of

Doctor of Philosophy

August 2019

Purdue University

West Lafayette, Indiana

**THE PURDUE UNIVERSITY GRADUATE SCHOOL
STATEMENT OF DISSERTATION APPROVAL**

Dr. Oleg Wasynczuk, Chair

School of Electrical and Computer Engineering

Dr. Steven Pekarek

School of Electrical and Computer Engineering

Dr. Dionysios Aliprantis

School of Electrical and Computer Engineering

Dr. Martin Corless

School of Aeronautics and Astronautics

Approved by:

Dr. Dimitri Peroulis

Head of the School Graduate Program

ACKNOWLEDGMENTS

There are several people I would like to thank for their support during my time in graduate school. First, I would like to thank my advisor, Dr. Oleg Wasynczuk, for his guidance in my research as well as my courses. His courses during my undergraduate career not only made me want to pursue a Ph.D. in this field, but also inspired me to be a better teacher once I became a graduate teaching assistant. I would like to thank Dr. Steve Pekarek, Dr. Dionysios Aliprantis, and Dr. Martin Corless for their invaluable input on my research, as well as Dr. Scott Sudhoff and Dr. Stanislaw Zak for being thoughtful and engaging instructors, in and out of the classroom.

I would also like to thank my friends and fellow graduate students during my time at Purdue. All have helped me learn new things, challenged me, commiserated with me, celebrated with me, and supported me for many years. I truly would not be where I am without them. I am lucky enough to have too many to list here, but you know who you are.

Finally, I would like to thank my family; my mother Ruth for her unflinching and unyielding love and support; my father Chip for his steadfastness and faith in me; my sisters Hannah and Rachel for challenging me to leave my comfort zone and exposing me to new ideas; Steve and Kyle for becoming my brothers and supporting me; and finally Lily and Fletcher for always being able to make me smile. Each has helped make me a better man, and I couldn't be more grateful.

TABLE OF CONTENTS

	Page
LIST OF TABLES	vi
LIST OF FIGURES	vii
ABSTRACT	x
1 Introduction	1
1.1 Small-displacement Stability of dc Systems	1
1.2 Small-displacement Stability of ac Systems	7
1.3 Large-displacement Stability of dc Systems	12
1.4 Large-displacement Stability of ac Systems	13
2 Stability Definitions	15
3 Ensuring Large-Displacement Stability in Dc Systems	23
3.1 Single-Source System	23
3.2 RAS and RLDS Estimation	26
3.3 Reachable State Space Estimation	29
3.4 Permanent-Magnet Generator with Active Rectifier	36
4 Ensuring Large-Displacement Stability in Ac Systems	42
4.1 Ac System Model and Controller Design	43
4.2 Parameter-Space Search	50
4.3 Estimating Regions of Asymptotic Stability	55
4.4 RSS Estimation	58
4.5 Small-Displacement Criterion	70
5 Detailed System Study	76
5.1 Detailed Inverter Model	76
5.2 Simulation results	81
6 Summary, Conclusions, and Areas of Future Research	99

	Page
6.1 Summary and Conclusions	99
6.2 Hardware Implementation	101
6.3 Improved Algorithms for Estimating Regions of Interest	101
6.4 Higher Dimensional Systems	102
6.5 Examining Load Characteristics	102
REFERENCES	103
A Search Algorithm	106
VITA	108

LIST OF TABLES

Table	Page
3.1 Simulation Parameters for single-source dc system.	27
3.2 RSS search parameters for the dc system	34
3.3 Generator-Rectifier System Parameters	38
3.4 RSS search parameters for the machine-rectifier system	40
4.1 The range of parameters over which the parameter space was searched. . .	51
4.2 RSS search parameters for the 50 kHz system	67
4.3 RSS search parameters for the 100 kHz system	70
5.1 Simulation parameters and per unit bases	82
5.2 RSS search parameters for the 50 kHz system with relaxed gains	90

LIST OF FIGURES

Figure	Page	
1.1	Circuit diagram illustrating the dynamic relationship between source Thevenin and terminal (load) voltage in a dc system.	3
1.2	A graphical depiction of small-displacement dc stability criteria [4].	6
1.3	A three-phase ac system.	9
1.4	Block diagram illustrating dynamic relationship between source Thevenin and terminal (load) voltage.	10
2.1	Graphical interpretation of the RAS for a 2nd order system.	16
2.2	Graphical illustration of RLDS of a system that is single-step stable.	19
2.3	Graphical illustration of a system that is neither SSS nor LDS. 20	
2.4	A graphical interpretation of a two-dimensional system that is LDS. Here, LDSM is the large-displacement stability margin.	22
3.1	Simple dc system.	24
3.2	Minimum transient overload capacity with respect to normalized time constant.	26
3.3	The RAS for a $P = 1$ pu.	28
3.4	The trajectories of the system under a 1 pu step-change in CPL.	28
3.5	The RAS's corresponding to different inputs to the single-source dc system.	29
3.6	The RSS and RLDS of the two dimensional dc system. The given system is large-displacement stable (LDS) with a large-displacement stability margin (LDSM) of 0.091.	35
3.7	Three RAS boundaries superimposed. The $RLDS = RAS_{P=1}$. Since $RSSE \subset RLDS$, the system is single-step stable.	39
3.8	The RSS and RLDS of the machine rectifier system. Since $RSS \subset RLDS$; the system is defined to be large-displacement stable with a stability margin of 0.32.	41
4.1	3-phase ac system.	45

Figure	Page
4.2 A projection of the parameter-space boundary onto $i_{lim}, X_{Cac}, v_{q,min}$ space	52
4.3 A projection of the parameter-space boundary onto $f_{sw}, X_{Cac}, v_{q,min}$ space	53
4.4 A projection of the parameter-space boundary onto $f_{sw}, i_{lim}, v_{q,min}$ space	54
4.5 Projections of the RAS for the ac system with a load of $P = 0.5$ pu, $Q = 0$ pu, projected into (a) v_q, v_d, i_{qI} space and (b) v_q, v_d, i_{dI} space. The region above the tunnel is guaranteed to be inside the RAS, while the region inside the tunnel is guaranteed to be outside the RAS.	57
4.6 Projections of the RAS for the ac system with a load of $P = \sqrt{2}/4$ pu, $Q = \sqrt{2}/4$ pu, projected into (a) v_q, v_d, i_{qI} space and (b) v_q, v_d, i_{dI} space. The region above the tunnel is guaranteed to be inside the RAS, while the region inside the tunnel is guaranteed to be outside the RAS.	59
4.7 Projections of the RAS for the ac system with a load of $P = \sqrt{2}/4$ pu, $Q = -\sqrt{2}/4$ pu, projected into (a) v_q, v_d, i_{qI} space and (b) v_q, v_d, i_{dI} space. The region above the tunnel is guaranteed to be inside the RAS, while the region inside the tunnel is guaranteed to be outside the RAS.	60
4.8 Projections of the RAS for the ac system with a load of $P = 0$ pu, $Q = 0.5$ pu, projected into (a) v_q, v_d, i_{qI} space and (b) v_q, v_d, i_{dI} space. The region above the tunnel is guaranteed to be inside the RAS, while the region inside the tunnel is guaranteed to be outside the RAS.	61
4.9 Projections of the RAS for the ac system with a load of $P = 0$ pu, $Q = -0.5$ pu, projected into (a) v_q, v_d, i_{qI} space and (b) v_q, v_d, i_{dI} space. The region above the tunnel is guaranteed to be inside the RAS, while the region inside the tunnel is guaranteed to be outside the RAS.	62
4.10 A projection of the intersections of conservative over-approximations of the RAS's for 5 loads around the PQ -plane into (a) v_q, v_d, i_{qI} space and (b) v_q, v_d, i_{dI} space.	63
4.11 The RSS and RLDS projected into (a) i_{qI}, v_d, v_q space, and (b) i_{dI}, v_d, v_q space with inputs bounded by 0.5 pu.	68
4.12 The RSS and RLDS projected into (a) i_{qI}, v_d, v_q space, and (b) i_{dI}, v_d, v_q space with inputs bounded by 1 pu.	71
4.13 The Belkhat contours of the LDS system over a broad range of frequencies.	74
5.1 Detailed model of the source converter.	77
5.2 A diagram of the detailed load model	82
5.3 A comparison of the duty cycle signal, d , in detailed simulations.	84

Figure	Page
5.4 Comparison of q -axis voltage results from average-value model and detailed simulation including voltage command filters and reduced controller gains.	85
5.5 Comparison of d -axis voltage results from average-value model and detailed simulation including voltage command filters and reduced controller gains.	86
5.6 Comparison of q -axis current results from average-value model and detailed simulation including voltage command filters and reduced controller gains.	87
5.7 Comparison of d -axis current results from average-value model and detailed simulation including voltage command filters and reduced controller gains.	88
5.8 Projections of the RLDS and RSS projected into (a) i_{qI}, v_d, v_q space and (b) i_{dI}, v_d, v_q space.	91
5.9 Ac bus capacitor voltages in physical (abc) variables during load transients.	92
5.10 Inverter output currents in physical (abc) variables during load transients .	93
5.11 The a -phase load current and commanded load current.	94
5.12 The b -phase load current and commanded load current.	95
5.13 The c -phase load current and commanded load current.	96
5.14 Simulated and commanded real power consumed by the load.	97
5.15 Simulated and commanded reactive power consumed by the load.	98
A.1 Visualization of the linear search being performed	107

ABSTRACT

Craddock, Thomas E. Ph.D., Purdue University, August 2019. Ensuring Large-Displacement Stability in ac Microgrids. Major Professor: Oleg Wasynczuk.

Aerospace and shipboard power systems, as well as emerging terrestrial microgrids, typically include a large percentage of regulated power-electronic loads. It is well known that such systems are prone to so-called negative-impedance instabilities that may lead to deleterious oscillations and/or the complete collapse of bus voltage. Numerous small-displacement criteria have been developed to ensure dynamic stability for small load perturbations, and techniques for estimating the regions of asymptotic stability about specific equilibrium points have previously been established. However, these criteria and analysis techniques do not guarantee system stability following large and/or rapid changes in net load power. More recent research has focused on establishing criteria that ensure large-displacement stability for arbitrary time varying loads provided that the net load power is bounded. These Lyapunov-based techniques and recent advancements in reachability analysis described in this thesis are applied to example dc and ac microgrids to not only introduce a large-displacement stability margin, but to demonstrate that the selected systems can be designed to be large-displacement stable with practicable constraints and parameters.

1. INTRODUCTION

With higher penetration of renewable energy sources, and with electric loads being more tightly regulated, designing microgrids with stability in mind is becoming increasingly necessary. Distributed Energy Resources (DER's) are not limited by the inertial response of large generators, and as such can respond much more quickly to changes in load. However, due to this lack of inertia, converter-based DER's can be less stable than their electric machine counterparts. Furthermore, power electronics-driven loads often present themselves as constant-power loads (CPL's), which exhibit a negative-impedance effect that greatly impacts the stability of a system [1–3]. Numerous researchers have developed design criteria to ensure the stability of both dc and ac power systems [1, 2, 4–8].

1.1 Small-displacement Stability of dc Systems

Power systems with regulated power-electronic loads such as those used in ships, submarines, aircraft, and spacecraft are often subject to negative-impedance instabilities [1–3]. Specifically, dc-to-dc converters and dc-to-ac inverters are often designed so that their output power is unaffected by perturbations in the input voltage. Since the conversion efficiency is close to unity, the input power remains essentially constant even if the input voltage varies, at least for variations within a certain range. Such loads are commonly called constant-power loads (CPL's), even though the load power may vary as a function of time. For small perturbations, it can be readily shown that a CPL appears as a negative resistance within the regulation bandwidth of the converter, which has a potentially destabilizing effect on the overall power system. Consequently, considerable attention has been devoted to the study and mitigation of potential instabilities attributed to this effect.

A key first step in stability analysis is the development of average-value models that can be linearized and therefore can produce linear state-space models and/or transfer functions relating the output impedance of source converters, Z_s , and the input admittance of load converters, Y_l , to the frequency of the voltage/current perturbations. For a single source connected to a single load, such as that shown in Figure 1.1, small-signal stability is achieved if and only if the Nyquist criterion is satisfied. This criterion is certainly satisfied if the Nyquist contour of $Z_s(\omega)Y_l(\omega)$ remains inside the unit circle for all frequencies leading to the Middlebrook criterion [9], which is a sufficient but not necessary criterion for small-signal stability. Although it has been shown that this criterion introduces conservatism [1], it is readily applied. Specifically, given the source impedance, it is easy to set forth a bound on the load admittance that will ensure the system is stable for small-signal disturbances. The primary criticism of the Middlebrook criterion has been that it leads to a conservative design. Consequently, numerous less conservative small-displacement stability criteria have been developed [2], [1].

Many stability analysis techniques stem from the Nyquist Stability Criterion, such as the Nyquist Immittance Criterion, the Middlebrook Criterion, the Opposing Argument Criterion, the Gain Margin/Phase Margin Criterion, and the ESAC Criterion. These criteria define so-called “forbidden regions” of the phase plane in which the Nyquist Contour is not allowed. These are described briefly in the following paragraphs.

The Nyquist Stability Criterion can be stated as “The number of unstable, closed-loop poles of a system is equal to the number of unstable open-loop poles plus the number of clockwise encirclements of the $-1 + j0$ point by the Nyquist Contour,” where the Nyquist Contour is the mapping of the Nyquist Path onto the $F(s)$ plane as a closed curve [10]. Here, $F(s)$ is the characteristic polynomial of the closed-loop system, and the Nyquist Path is the clockwise contour consisting of the entire imaginary axis of the complex plane and a semicircular path of infinite radius in the right-half s plane.

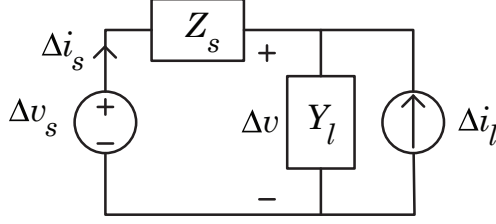


Fig. 1.1.: Circuit diagram illustrating the dynamic relationship between source Thevenin and terminal (load) voltage in a dc system.

The Nyquist Immittance Criterion (NIC) is derived from the Nyquist Stability Criterion for a system consisting of a Thevenin-equivalent source with impedance $Z_s(s)$ feeding a Norton-equivalent load with admittance $Y_l(s)$. The NIC states that a necessary and sufficient condition for this system to be stable is if the Nyquist evaluation of $Z_s(s)Y_l(s)$ does not encircle the $-1 + j0$ point [11].

The Middlebrook Criterion is a sufficient, but not necessary condition for stability of dc systems. It states that the ratio of source impedance Z_s to load impedance Z_l , known as the minor loop gain, is less than the reciprocal of the gain margin $\frac{1}{GM}$ for all frequencies [4, 11]:

$$\left| \frac{Z_s}{Z_l} \right| < \frac{1}{GM}, \quad GM > 1 \quad (1.1)$$

It is obvious that the Nyquist Contour can never encircle $-1 + j0$ if this criteria is met, due to the fact that it is contained by the unit circle. The forbidden region of the s -plane is shown in Figure 1.2. While easily applied, this criterion introduces an unnecessary degree of conservatism to designs.

The Gain-Margin/Phase-Margin (GMPM) criteria, whose forbidden region is shown in Figure 1.2, is less conservative than Middlebrook. GMPM stipulates that the minor loop gain be less than the reciprocal of the gain margin $\frac{1}{GM}$, or that the difference in angle between Z_s and Z_l be no greater than 180° less the phase margin [4, 11, 12].

$$\left| \frac{Z_s}{Z_l} \right| < \frac{1}{GM} \quad \text{or} \quad |\arg(Z_s) - \arg(Z_l)| \leq 180^\circ - PM \quad (1.2)$$

While less conservative than Middlebrook, GMPM is still restrictive, and requires knowledge of both magnitude and phase information for both the source and the load.

The Opposing Argument Criterion (OAC) was developed when GMPM was found to be difficult to generalize and scale. The OAC states that the real part of the minor loop gain is greater than the negative reciprocal of the gain margin:

$$\text{Re} \left(\frac{Z_s}{Z_l} \right) > -\frac{1}{GM} \quad (1.3)$$

The forbidden region this criteria defines is also shown in Figure 1.2. This criterion is particularly useful when paralleling loads, as the criterion can be modified slightly to obtain a criterion for each load individually. The modified criterion is

$$\text{Re} \left(\frac{Z_s}{Z_{l,k}} \right) > -\frac{1}{GM} \frac{P_s}{P_{l,k}} \quad (1.4)$$

Where P_s is the power delivered by the source and $P_{l,k}$ is the power delivered to the k th load. While the OAC is more general than GMPM, and less conservative than Middlebrook, it still requires both magnitude and phase information about the source and load/loads. Additionally, it still imposes a degree of conservatism [4, 11, 13–15].

The Energy Source Analysis Consortium (ESAC) criterion was developed to reduce the “forbidden region”, thereby limiting artificially introduced conservatism [2, 4, 11]. The forbidden region is shown in Figure 1.2. Furthermore, with the previous criteria, it was observed that component grouping was a critical decision when analyzing stability. It is possible for one definition of “source” and “load” to be stable, while another definition could be unstable, even if both systems are identical. The ESAC criterion is less sensitive to these definitions, though it does not entirely eliminate the issue. The ESAC criterion defines a 3-dimensional “forbidden volume” in the admittance space (magnitude, phase, and frequency) which the load admittance must not enter. Moreover, a generalized set of load admittances can be defined and

tested, which makes the ESAC criterion very well suited for regional stability analysis as well as local stability analysis. The ESAC criterion is difficult to apply, however, and still is only applicable to linear systems. Nonlinear systems require linearizing for its use, which calls into question the criterion's applicability in large-displacement stability analysis.

Similar to the ESAC criterion is the Root-Exponential Stability Criterion (RESC), which defines a forbidden region of the s -plane similar in shape to that defined by ESAC, but defined with a continuous function of s [16]. The function is given by

$$f(s) = \sqrt[n]{(\alpha \text{Im}(s))^n + (\beta e^{\gamma \text{Re}(s)})^n} \quad (1.5)$$

where α , β , and γ are constants defined in terms of the desired gain and phase margins, and n is an integer greater than or equal to 2. The edge of the forbidden region is defined by the points on which $f(s) = 1$. This criterion was developed to offer greater numerical stability during design, since the boundary of the forbidden region is well defined at all points. This boundary can be seen in Figure 1.2.

The previous stability criteria are used to analyze systems in the DC Stability Toolbox [11]. This toolbox allows for the modeling and analysis of a wide array of systems in an average value sense. The toolbox has routines capable of evaluating contours, evaluating stability criteria, and has built-in components useful for design and simulation. A graphical description of these criteria showing forbidden regions is shown in Figure 1.2.

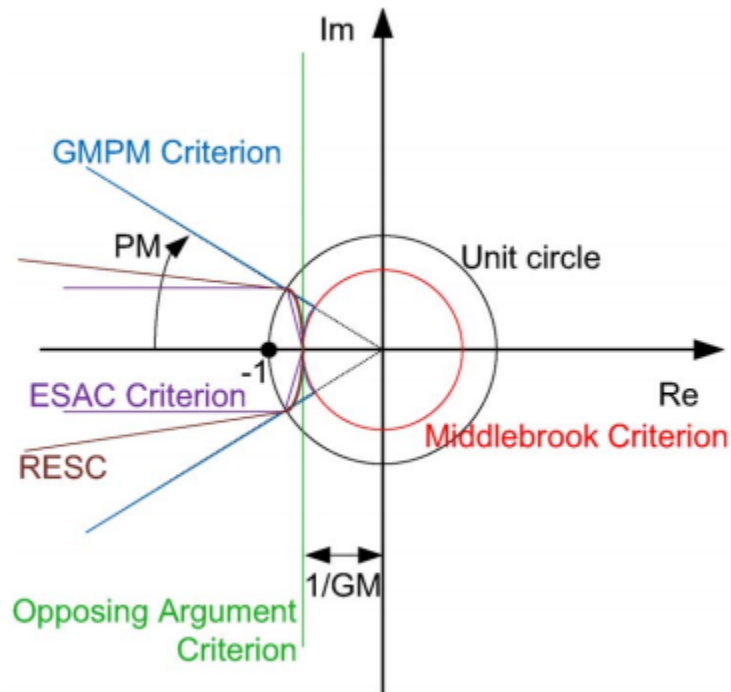


Fig. 1.2.: A graphical depiction of small-displacement dc stability criteria [4].

Other criteria have been proposed for small-signal stability analysis, such as the Three-Step Impedance Criteria (T-SIC) [17]. All previously discussed criteria assume a stable transfer function associated with the source, and are based on assessment of the minor-loop gain. An extended minor loop gain is defined and used in Nyquist contours, which affords the possibility of an unstable source. Furthermore, with the aforementioned stability criteria, it is possible to arrive at incorrect results when applying them to systems with regulated loads. With T-SIC, stability is guaranteed, even with regulated loads, due to a pure impedance mapping introduced in [17].

Finally, there is the Passivity-Based Stability Criterion (PBSC), which is not based on minor loop gain analysis. PBSC guarantees stability if Z_{bus} (the parallel combination of all source and load impedances on a given bus) has no Right-Half Plane (RHP) poles, and if the real part of that parallel combination is greater than

or equal to 0 [4, 18]. This is equivalent to requiring that the angle of Z_{bus} lies between -90 and 90 degrees for all frequencies.

While useful, these design criteria are considered to be “small-displacement” criteria due to the fact that they only apply to linear systems. In practicable power systems, there does not exist a truly linear system due to the presence of CPL’s and hard limits placed on control variables. When modeling systems and performing stability analysis, it is necessary to approximate the system’s behavior by linearizing about an equilibrium point or assuming that the system is operating within its physical limits.

However, the main disadvantages of small-displacement analysis are: (a) guaranteeing small-displacement stability, albeit over a range of operating conditions, does not guarantee stability following large disturbances such as pulsed loads, faults, component failures, or the connection/disconnection of large loads; and (b) they are generally difficult to apply to complex systems where the number of potential source/load configurations is very large. Each and every potential configuration must either be considered in the design phase, or an on-line strategy is needed to evaluate the stability before a new configuration is entered.

1.2 Small-displacement Stability of ac Systems

For ac systems, traditional stability analysis techniques are difficult to apply directly, since the physical variables vary as a function of time, even for steady-state operation. The Nyquist stability criterion and more general analysis techniques such as Lyapunov’s Direct and Indirect methods rely on the state settling out to a constant value in steady-state. Techniques taken from the study of orbital mechanics, such as Floquet Theory [19, 20], can be used, but are often difficult to understand and apply. As such, it is useful to define a reference frame transformation such that the states do in fact become dc in steady-state. For 3-phase systems, a commonly used transformation is defined as

$$\begin{bmatrix} f_q \\ f_d \\ f_0 \end{bmatrix} = \frac{2}{3} \begin{bmatrix} \cos \theta & \cos(\theta + 2\pi/3) & \cos(\theta - 2\pi/3) \\ \sin \theta & \sin(\theta + 2\pi/3) & \sin(\theta - 2\pi/3) \\ 1/2 & 1/2 & 1/2 \end{bmatrix} \begin{bmatrix} f_a \\ f_b \\ f_c \end{bmatrix} \quad (1.6)$$

where f is a placeholder for voltage, current, flux linkage, or any other 3-phase quantity in the system of interest, and $\theta = \omega t$ where ω is the speed of the reference frame in which the variables are expressed. The subscripts on the right-hand side of the equation denote the phase to which each variable corresponds, and the subscripts on the left-hand side denote the fictitious axes onto which the states are being projected.

An example three-phase power system is depicted in Figure 1.3. Therein v_{qs}^e and v_{ds}^e (i_{qs}^e and i_{ds}^e) denote the q and d components of terminal voltage (current) in a synchronously rotating frame of reference ($\theta = \omega_e t$ where ω_e is the ac frequency). During balanced, steady-state operating conditions, these variables are constant and the zero sequence variable is identically zero. For small perturbations, the dynamic relationship between source voltage and current relationships can be expressed in transfer function form as

$$\begin{bmatrix} \Delta v_q^e \\ \Delta v_d^e \end{bmatrix} = \begin{bmatrix} z_{qq} & z_{qd} \\ z_{dq} & z_{dd} \end{bmatrix} \begin{bmatrix} \Delta i_q^e \\ \Delta i_d^e \end{bmatrix} + \begin{bmatrix} h_{qq} & h_{qd} \\ h_{dq} & h_{dd} \end{bmatrix} \begin{bmatrix} \Delta v_{qS}^e \\ \Delta v_{dS}^e \end{bmatrix} \quad (1.7)$$

Symbolically,

$$\Delta \mathbf{v}_{qd}^e = \mathbf{Z}_S \Delta \mathbf{i}_{qd}^e + \mathbf{H} \Delta \mathbf{v}_{qdS}^e \quad (1.8)$$

where $\Delta \mathbf{v}_{qdS}^e$ may be viewed as a perturbation in the source's Thevenin voltage and \mathbf{Z}_S as the source impedance, which is now a 2×2 transfer function matrix. Similarly, for the load,

$$\Delta \mathbf{i}_{qd}^e = \mathbf{Y}_L \Delta \mathbf{v}_{qd}^e \quad (1.9)$$

where \mathbf{Y}_L is the load admittance. The preceding two equations can be placed into block-diagram form as shown in Figure 1.4.

The Nyquist criterion as described in the previous section is valid only for Single Input, Single Output (SISO) systems, but in 3-phase ac systems, there are 2 indepen-

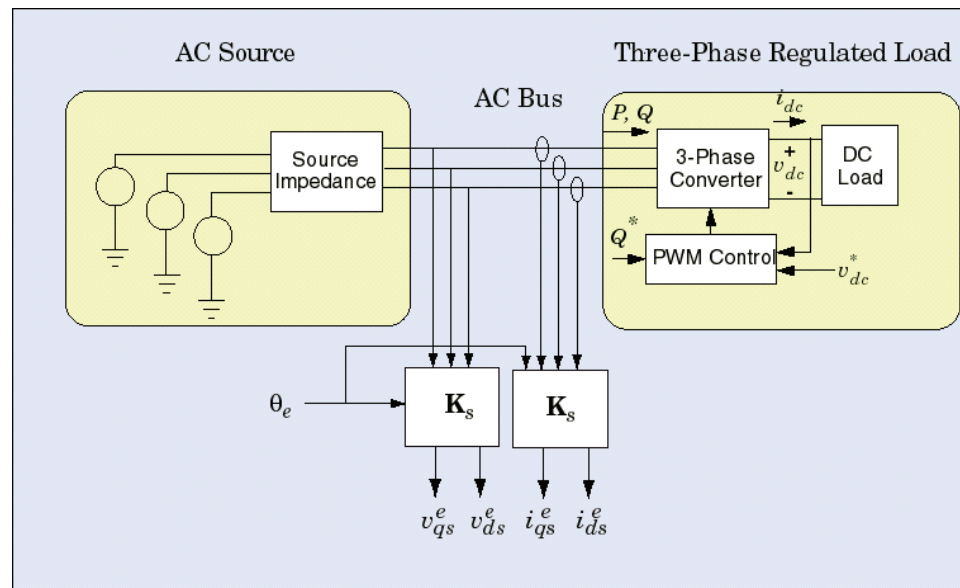


Fig. 1.3.: A three-phase ac system.

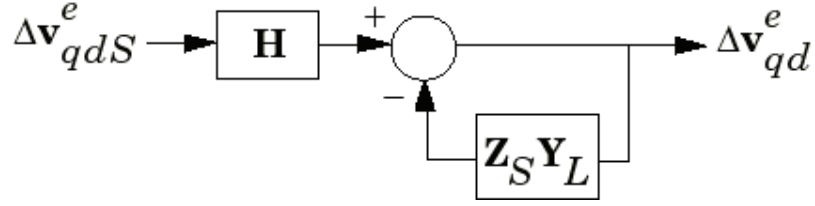


Fig. 1.4.: Block diagram illustrating dynamic relationship between source Thevenin and terminal (load) voltage.

dent voltages and 2 independent currents. The Nyquist Criterion can be generalized to handle such a problem [5, 6, 21], where the Nyquist contour is evaluated on the eigenvalues of the open-loop transfer matrix $\mathbf{Z}_S \mathbf{Y}_L$, which is analogous to the minor loop gain in the previous section. The loci that are generated are referred to as the eigen-loci, and if the eigen-loci never encircle -1, the system is said to be Bounded Input Bounded Output (BIBO) stable [5].

Several results from Linear Algebra are applied to this criterion to develop design-oriented design criteria that are more readily applied. In one case, the Gershgorin, or G -norm is defined for a matrix \mathbf{R} as

$$\|\mathbf{R}\|_G = \max_{i,j} (|r_{i,j}|) \quad (1.10)$$

If the G -norm of $\mathbf{Z}_S \mathbf{Y}_L$ is less than 1 for all frequencies, or

$$\|\mathbf{Z}_S \mathbf{Y}_L\|_G < \frac{1}{2} \quad (1.11)$$

then by Gershgorin's Circle Theorem, the eigenvalues of the return ratio will be within the unit circle, and the system will be BIBO stable, provided \mathbf{Z}_S and \mathbf{Y}_L have no poles in the right-half plane [5].

This approach can be advantageous, since it does not require the calculation of eigenvalues for the closed-loop system; however, it can be difficult to apply in the design process, since it is not clear how individual elements of \mathbf{Z}_S or \mathbf{Y}_L affect the

final outcome. The return ratio can be decoupled, and the G -norm criterion can be applied to each matrix individually, resulting a criterion expressed mathematically as

$$\|\mathbf{Z}_S\|_G \|\mathbf{Y}_L\|_G < \frac{1}{4} \quad (1.12)$$

This technique can be expanded by applying other norms, which can reduce conservatism in the design. For example, the induced infinity norm can be applied to \mathbf{Z}_S and the induced unity norm can be applied to \mathbf{Y}_L . Since each element of $\mathbf{Z}_S \mathbf{Y}_L$ is an inner product between a row of \mathbf{Z}_S and a column of \mathbf{Y}_L , the infinity norm is equivalent to the largest row sum of a matrix, and the unity norm is equivalent to the largest column sum of a matrix, it can be shown that if

$$\|\mathbf{Z}_S\|_{i,\infty} \|\mathbf{Y}_L\|_{i,1} < \frac{1}{2} \quad (1.13)$$

the system will be BIBO stable.

Finally, a criterion was developed based on the singular values of the return ratio. It may be shown that

$$\|\mathbf{Z}_S \mathbf{Y}_L\|_2 = \bar{\sigma}(\mathbf{Z}_S \mathbf{Y}_L, \omega) \quad (1.14)$$

where $\bar{\sigma}$ is the largest singular value of $\mathbf{Z}_S \mathbf{Y}_L$. It can be seen that if the induced norm of the return ratio is less than 1 for all frequencies, then the system will be BIBO stable. Furthermore, by the Cauchy Inequality,

$$\|\mathbf{Z}_S \mathbf{Y}_L\|_2 \leq \|\mathbf{Z}_S\|_2 \|\mathbf{Y}_L\|_2 \quad (1.15)$$

Thus, the system will be stable if

$$\bar{\sigma}(\mathbf{Z}_S, \omega) \bar{\sigma}(\mathbf{Y}_L, \omega) < 1 \quad (1.16)$$

for all frequencies [5]. Equation (1.16) is analogous to the well-known Middlebrook criterion used in dc systems.

These criteria have many of the same limitations as their dc counterparts. The system under study is assumed to be linear. Nonlinear systems can be studied with these techniques, yet it remains unclear how large of a perturbation can be applied

before the stability criteria are invalidated by large discrepancies between the linear approximation of the system behavior and the true system behavior. With this in mind, it is important to develop a definition for large-displacement stability in both ac and dc power systems, and is referred to in this thesis as the Belkhat criterion [6].

1.3 Large-displacement Stability of dc Systems

To address concerns raised with the negative-impedance effect, research was performed into estimating the Region of Asymptotic Stability (RAS) of dc systems for Naval ships [22]. In this research, several methods are set forth to generate Lyapunov functions for a given system, and subsequently these Lyapunov functions are used to estimate the RAS for a given equilibrium point using genetic algorithms.

This method presents several advantages over small-displacement methods, primarily by generating a subset of the RAS. One of the properties of the RAS is that it is impossible for the state to leave the RAS, and as such, if the equilibrium point remains the same, the state vector will always approach the equilibrium point asymptotically. This property holds true regardless of the linearity of the system.

This method of RAS estimation can be conservative. One is only guaranteed to be a subset of the RAS, not necessarily the whole region. Furthermore, the Lyapunov functions that were generated were all quadratic, which then creates an elliptical RAS estimate, which may not reflect the true shape of the RAS.

The RAS was established using a different approach in [3]. Therein, a brute force sweep of the state space was performed to find the boundary of the RAS for an equilibrium point of a single-source dc system feeding a constant-power load. It was observed that there exists a trade-off between source response time, dc link capacitance, and transient overload capacity, and this trade-off was quantified. A design paradigm was then set forth based upon this trade off. Many of the results described in this paper is repeated later in this document, and then expanded. “Large-

displacement Stability” was defined as maintaining stability for a single step-change in load power. This definition is revisited and revised later in this thesis.

1.4 Large-displacement Stability of ac Systems

Research has been performed in the realm of ac microgrids to address the limitations of small-displacement stability analysis techniques as well. In [23], Popov’s absolute stability criterion was applied to analyze an ac source supplying a constant-power load. To apply Popov’s criterion, the system model must take on the following form:

$$\dot{\mathbf{x}} = \mathbf{A}\mathbf{x} + \mathbf{B}\mathbf{u} \quad (1.17)$$

$$\mathbf{y} = \mathbf{C}\mathbf{x} + \mathbf{D}\mathbf{u} \quad (1.18)$$

$$\mathbf{u} = -\psi(\mathbf{y}) \quad (1.19)$$

where $\psi \in [0, \infty)$ is a continuous function in \mathbf{y} that is memoryless and locally Lipschitz, and accounts for the nonlinear behavior of the system. It has been shown that by careful selection of a Lyapunov function using the so-called Kalman-Yakubovich-Popov lemma, the system is asymptotically stable.

This technique is certainly attractive, due to the fact that the nonlinearities introduced with constant-power loads meet the criteria of $\psi(\mathbf{y})$, however, there is at least one major shortcoming of this approach. In practicable power systems, it is necessary to limit commanded values to be below a certain level. For example, it can be dangerous to allow the controller to command a dc link current values significantly greater than the source rating, since such a current may have a damaging effect on the system. Instead, the current command might be limited to say 120% of its rated value, so that if an overcurrent is commanded, there is less danger of damaging the system. Limiting commands in this fashion is common, however it introduces a nonlinearity that cannot be represented by (1.17)-(1.19), and therefore it can be difficult to analytically determine the stability of an operating point using Popov’s criterion.

Work was done in [24] to design 3-phase ac systems with large-displacement stability in mind. In that work, a region of stability was established numerically in the PQ plane, where P is real power and Q is reactive power. The way in which the size and shape of this region varied was investigated by adjusting system response time and controller constants, and a control paradigm was set forth for maintaining stability of a 3-phase bus voltage based on a timing signal present in different parts of the control.

Similar to the work done in [3], it was assumed that the system need only maintain stability for a single step-change in P and/or Q . The work set forth in this thesis diverges from and expands on this notion by defining large-displacement stability for any number of step changes in load, so long as the load is in an allowable set.

2. STABILITY DEFINITIONS

Average value models of power systems can typically be expressed mathematically as a set of coupled, first-order ordinary differential equations. Symbolically

$$\frac{dx}{dt} = f(x(t), u); \quad x(t_0) = x_0 \quad (2.1)$$

where $x(t) \in \mathbb{R}^n$ is an n -dimensional state vector with initial condition x_0 at time t_0 , and $u \in \mathbb{R}^m$ is an m -dimensional input vector. In the case of power systems, the state vector is frequently comprised of inductor currents, capacitor voltages, or control system states, while the input vector is made up of load currents, load power, or commanded steady-state values of states. In general, u need not be constant, however, the initial focus of this section is on a system with constant input (later, the implications of a time-varying input are discussed). Finally, $f(x, u)$ is assumed to be Lipschitz-continuous with respect to x and u . This ensures a unique solution to (2.1). If u is fixed, it can be seen that the right-hand side of (2.1) depends only on the state vector x , and is not an explicit function of time t .

In general, a system such as (2.1) may or may not have what is referred to as an equilibrium state x_e that satisfies $f(x_e, u) = 0$. In practicable power systems, it is all but essential that there exists one such equilibrium state, and so it is assumed that there is one for the following discussion. Often, a new state vector is defined as $\tilde{x} = x - x_e$ and (2.1) is reformulated so that the equilibrium state becomes $\tilde{x}_e = 0$. However, this common convention will not be followed in this thesis for reasons that will become apparent.

It is useful at this point to define certain terms that will be used in this thesis [25]. First, a system is said to be stable in the sense of Lyapunov (SISL) if for every $\epsilon > 0$ and any given initial time t_0 , there exists a scalar $\delta = \delta(\epsilon, t_0) > 0$ such that if $\|x(t_0) - x_e\| < \delta$, then $\|x(t; t_0, x_0) - x_e\| < \epsilon$ for all $t \geq t_0$. Here, $\|x\|$ is the

Euclidean-norm of x . An equilibrium point x_e of a system is said to be convergent if for any given t_0 there is a positive scalar $\delta_1 = \delta_1(t_0)$ such that if $\|x(t_0) - x_e\| < \delta_1$, then

$$\lim_{t \rightarrow \infty} x(t; t_0, x_0) = x_e \quad (2.2)$$

An equilibrium point of a system is said to be asymptotically stable in the sense of Lyapunov (ASISL) if it is both SISL and convergent. Furthermore, an equilibrium point of a system is said to be uniformly asymptotically stable (UASISL) if it is ASISL and δ is independent of t_0 . Finally, an equilibrium point is said to be globally uniformly asymptotically stable (GUASISL) if it is UASISL and δ is infinitely large.

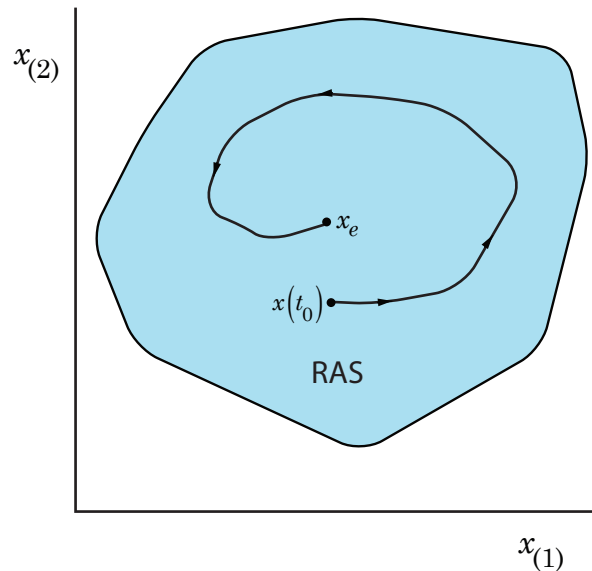


Fig. 2.1.: Graphical interpretation of the RAS for a 2nd order system.

A desirable, if not essential feature of a practicable power system is that the equilibrium state for any allowable operating condition is UASISL. However, due to voltage/current constraints or bandwidth limitations, it is generally not possible to design a system that is GUASISL. Therefore, in a practicable system, there exists a so-called the region of asymptotic stability (RAS), which is defined as the set of all x_0

for which the solution of (2.1) satisfies $\|x(t; t_0, x_0) - x_e\| \rightarrow 0$ as $t \rightarrow \infty$. A graphical interpretation of a RAS for a 2nd-order system ($x(t) \in \mathbb{R}^2$) is depicted in Figure 2.1 where $x_{(1)}$ and $x_{(2)}$ denote the system states. An important point to make is that all stable trajectories are wholly contained in the RAS and all unstable trajectories never enter the RAS. Because of these properties, it is desirable to establish the RAS for any given system.

Suppose now that the input u is allowed to vary within a set of allowable inputs $U \subset \mathbb{R}^m$. In practicable power systems, inputs are not assumed to be arbitrary. For example, during normal operation, the input power would not exceed rated power. It is assumed here that U is a path-connected topological space that is not necessarily convex. By designing the system appropriately, it can be assumed that for each $u_i \in U$, there exists a single corresponding x_{ei} satisfying $f(x_{ei}, u_i) = 0$. Again, by designing the control system well, the equilibrium point x_{ei} can be made to be locally asymptotically stable.

The dynamic behavior for small displacements from the equilibrium can be characterized by linearizing $f(x, u)$ about $x_{e,i}$ and u_i ,

$$\frac{d\Delta x}{dt} = \left. \frac{\partial f(x, u)}{\partial x} \right|_{x_{e,i}, u_i} \Delta x + \left. \frac{\partial f(x, u)}{\partial u} \right|_{x_{e,i}, u_i} \Delta u \quad (2.3)$$

where $\Delta x = x - x_{e,i}$ and $\Delta u = u - u_i$. Simplifying notation,

$$\frac{d\Delta x}{dt} = \mathbf{A}(x_{e,i}, u_i) \Delta x + \mathbf{B}(x_{e,i}, u_i) \Delta u \quad (2.4)$$

where $\mathbf{A}(x_{e,i}, u_i)$ is commonly called the Jacobian Matrix. In order for the equilibrium state $x_{e,i}$ to be locally ASISL, the eigenvalues of $\mathbf{A}(x_{e,i}, u_i)$ must have negative real parts. Under the assumption that a controller can be designed to ensure local asymptotic stability, this implies that \mathbf{A} is of full rank, and therefore invertible. By the Implicit Function Theorem [26], this implies that there is a continuously differentiable function $g(\cdot)$ such that $x_{e,i} = g(u_i)$ and that $f(g(u), u) = 0$ for all u .

It is useful to define the region of steady-state equilibria (RSSE) as

$$\text{RSSE} = \{x_{e,i} \forall u_i \in U\} \quad (2.5)$$

Since the mapping from u_i to $x_{e,i}$ is continuous and U is path connected, the RSSE will also be a path-connected topological space. So as u varies in U , the equilibrium state will move withing the RSSE. For each $x_{e,i} \in \text{RSSE}$, the corresponding RAS will be denoted as RAS_i . The establishment of RAS_i is, in general, difficult. As noted in the previous chapter, a method of establishing RAS estimates for a naval dc power system using genetic optimization is described in [22] and [27]. This method is limited by the fact that it can only determine an elliptical approximation of the RAS, and not the true RAS. Later sections of this thesis outline a procedure for establishing RAS_i . This is accomplished by brute-force searching the state space, which is readily and precisely done due to the small dimension of the system. If the numerical solution of (2.1) starting at the search point converges to $x_{e,i}$, the given state lies inside RAS_i . Otherwise, it does not. The boundary will be a 1-dimensional path if $n = 2$, a 2-dimensional surface if $n = 3$, or, in general, an $n - 1$ dimensional hypersurface. Subsequently, it is assumed that RAS_i is known for all $x_{e,i} \in \text{RSSE}$.

It is useful to define the region of large-displacement stability (RLDS) as

$$\text{RLDS} = \bigcap_{x_{e,i} \in \text{RSSE}} \text{RAS}_i \quad (2.6)$$

If the RLDS of a system is non-empty, and contains the RSSE and the reachable state space (RSS), the system is said to be single-step stable (SSS). An important feature of a system that is SSS is that the input u can be stepped from any $u_i \in U$ to any other arbitrary $u_j \in U$ with $x(t_0) = x_{e,i}$ with the resulting trajectory guaranteed to converge asymptotically to the new equilibrium $x_{e,j}$. This result is illustrated in the following paragraphs.

A graphical illustration of a 2nd order system ($n = 2$) that is SSS is depicted in Figure 2.2. The figure shows the RAS for two prototypical equilibrium states (out of infinitely many), the RLDS, and the RSSE. It can be seen that the RSSE is entirely contained in the RLDS, which is the intersection of all RAS_i corresponding to all possible inputs u_i . If u is stepped from u_1 to u_2 at $t = t_0$ with $x(t_0) \in \text{RLDS}$, then the ensuing trajectory will asymptotically converge to $x_{e,2}$ since $x(t_0) \in \text{RLDS} \subset \text{RAS}_2$.

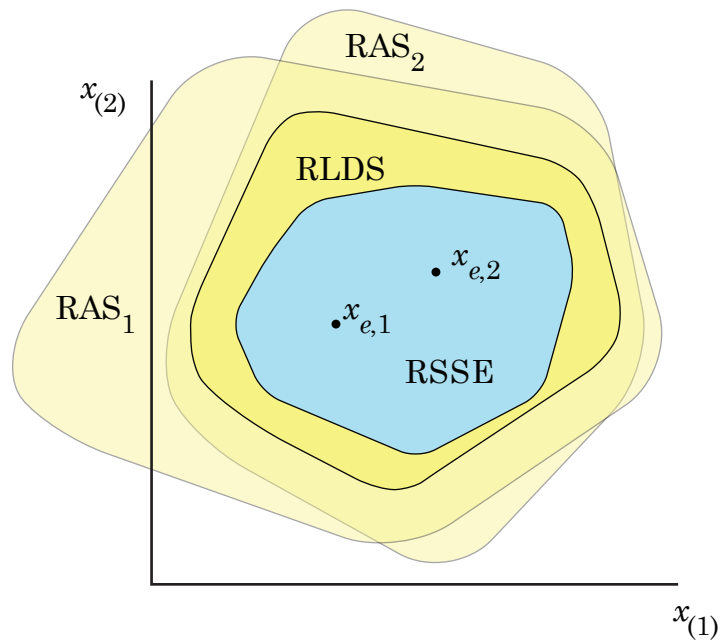


Fig. 2.2.: Graphical illustration of RLDS of a system that is single-step stable.

By extension, u can be stepped from any $u_j \in U$ and, as long as $x(t_0) \in \text{RLDS}$, the ensuing response will asymptotically approach $x_{e,j}$.

A graphical illustration of a system that is not LDS is depicted in Figure 2.3. Although the RLDS is not shown, it is a subset of $\text{RAS}_1 \cap \text{RAS}_2 \cap \text{RAS}_3$, which is a small region surrounding $x_{e,2}$. It should be apparent that the $\text{RSSE} \not\subset \text{RLDS}$. Additionally, only three RAS's are shown in the figure, while more obviously exists. It is assumed that the RLDS exists in this example, though it is not guaranteed in general. Therein, the system response for a step change from u_1 to u_2 with $x(t_0) = x_{e,1}$ will converge since $x_{e,1} \in \text{RAS}_2$. It can be seen, however, that the response for a step change from u_1 to u_3 with $x(t_0) = x_{e,1}$ will not converge since $x_{e,1} \notin \text{RAS}_3$. Although the step response from u_1 to u_3 is unstable, it is nonetheless possible to reach $x_{e,3}$ starting at $x_{e,1}$ by first stepping from u_1 to u_2 , allowing $x(t)$ enter into RAS_3 , and then stepping u to u_3 . Since all equilibria are locally asymptotically stable, the system could be stable if the input u is prevented from changing abruptly or too fast.

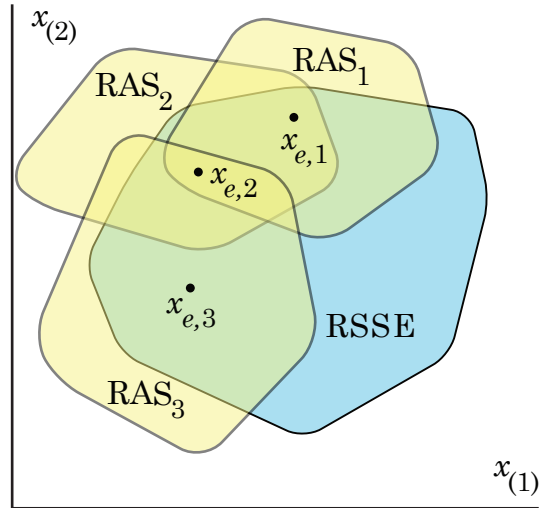


Fig. 2.3.: Graphical illustration of a system that is neither SSS nor LDS.

However, it lacks the robustness that a LDS system offers. Great care is required in determining input changes when the system is not LDS.

Next, suppose that the input $u(t)$ is a piecewise constant function of time with a finite number of steps from any value in U to any other value in U . Because the mapping from u to x_e is continuous, the corresponding equilibrium state $x_e(t)$ will then be a piecewise constant function of time that is constrained to the RSSE. As the number of steps is increased, u and x_e can be made to approximate piecewise continuous functions of time. It is useful to define the reachable state space (RSS) of a system as the set of states that are reachable from any $x \in \text{RSSE}$ for any $u(t) \in U$ as $t \rightarrow \infty$. A system is defined herein to be Large-Displacement Stable (LDS) if

$$\text{RSS} \subset \text{RLDS} \quad (2.7)$$

This definition is supported by the notion that leaving the RLDS implies that the state trajectory is outside at least one RAS. If the input is stepped to the value corresponding to that RAS at any time the trajectory is outside that RAS, the trajectory

is guaranteed to go unstable. Therefore, it is desirable for the reachable set to be inside the RLDS.

It is a necessary and sufficient condition for the RSS to be bounded to ensure that a given system is LDS. This is because the RSS can only be bounded if it is bounded by the RLDS, which can be understood following the same reasoning that motivates the definition. If a hypothetical RSS is bounded, though not contained by the RLDS, then state trajectories are possible that go outside the RLDS, and therefore the possibility of instability exists, which implies the RSS is not bounded. This contradiction illustrates that the only way for the RSS of a given system to be bounded is if the bound is within the space common to every RAS, which is the RLDS. This motivates the definition of Large-Displacement Stability.

In practice, a bounded RSS may not be sufficient for a designer to claim the actual physical system is LDS. This is due to the fact that both the RSS and the RLDS are established via numerical simulation or calculation based on average-value models of the system, which inherently contain assumptions and approximations. Therefore, to gain a sense of robustness relative to model uncertainties, a Large-Displacement Stability Metric (LDSM) is set forth as the minimum distance between the two boundaries:

$$\text{LDSM} = \min \|x_1 - x_2\|: x_1 \in \text{RSS}, x_2 \notin \text{RLDS} \quad (2.8)$$

A graphical interpretation of the LDSM can be seen in Figure 2.4.

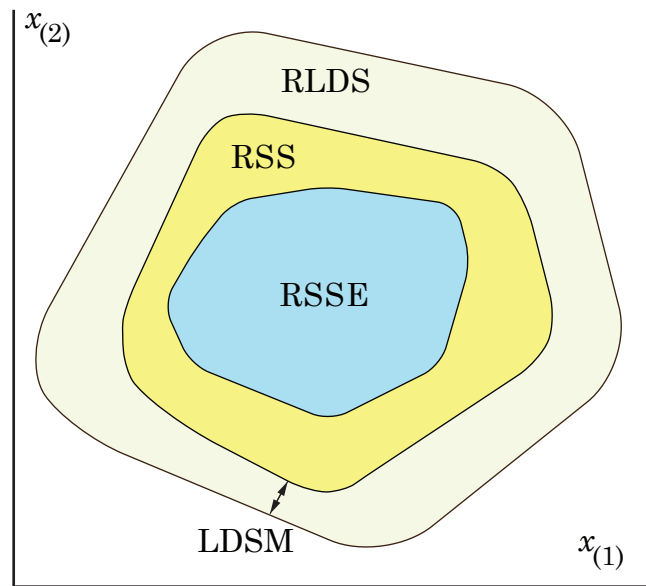


Fig. 2.4.: A graphical interpretation of a two-dimensional system that is LDS. Here, LDSM is the large-displacement stability margin.

3. ENSURING LARGE-DISPLACEMENT STABILITY IN DC SYSTEMS

In this chapter, two sample systems are discussed. The results of two system studies performed in [3] and [28] are reviewed. The first system studied in those works is a single-source dc power system with a constant-power load. The results of that study are extended in the following section, which investigates the stability of a dc system with electric machine dynamics taken into account. In both cases, the RLDS, RSSE, and RSS are readily visualized geometrically due to their low dimension.

3.1 Single-Source System

A simple dc system is shown in Figure 3.1 [3]. A controllable current source supplies a dc-link capacitor which, in turn, supplies an ideal constant-power load. The current source is considered non-ideal due to its non-zero response time and current limits. The current supplied by the source has a first-order response with respect to its command, which is generated with a simple proportional controller with a feed-forward term.

$$i_s^* = k_p(v_{dc}^* - v_{dc}) + i_{load} \quad (3.1)$$

Here, v_{dc}^* is the commanded dc voltage, which is set to $v_{dc}^* = 1$.

For generality, the study is performed in per-unit. That is, v_{dc} , i_{dc} , and P are all equal to 1 for rated steady-state conditions. It can be easily shown that the equations governing the system are identical in per-unit and in the International System of Units (SI units). Assuming that the limit on the current command is not reached, the state-space representation of Figure 3.1 can be expressed:

$$p \begin{bmatrix} i_s \\ v_{dc} \end{bmatrix} = \begin{bmatrix} -\frac{1}{\tau_s} & -\frac{k_p}{\tau_s} \\ \frac{1}{C} & 0 \end{bmatrix} \begin{bmatrix} i_s \\ v_{dc} \end{bmatrix} + \frac{1}{v_{dc}} \begin{bmatrix} \frac{1}{\tau_s} \\ \frac{1}{C} \end{bmatrix} P + \begin{bmatrix} \frac{k_p}{\tau_s} \\ 0 \end{bmatrix} v_{dc}^* \quad (3.2)$$

where p is the Heaviside operator for differentiation with respect to time.

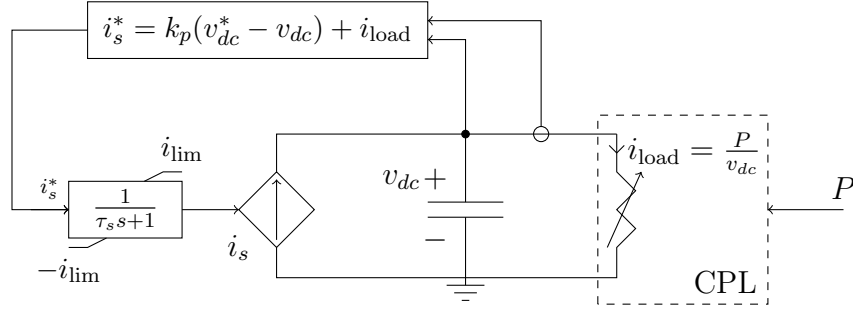


Fig. 3.1.: Simple dc system.

The term “constant-power Load” (CPL) can be ambiguous in its usage, and so it is necessary to discuss what is meant when that term is used in this thesis. An ideal CPL is a load whose current is equal to the net load power being consumed P divided by the voltage dropped across the load. In many cases, the net power delivered to the load can be assumed piecewise constant, though in general, this is not always true. It may be the case that the power delivered to the load is most conveniently modelled as some continuous function of time, and hence the input to the system should be represented as a function $P(t)$ rather than a constant P . Therefore the term “constant-power Load” is not strictly accurate in general, but is the most commonly used and convenient description for the load behavior being modelled in this thesis.

For convenience, a scaled-time $\tau' = \tau/C$ is introduced. This not only simplifies (3.2), but it also facilitates the examination of the trade-off that exists between transient-overload capacity and the source’s normalized response time τ'_s .

$$p' \begin{bmatrix} i_s \\ v_{dc} \end{bmatrix} = \begin{bmatrix} -\frac{1}{\tau'_s} & -\frac{k_p}{\tau'_s} \\ 1 & 0 \end{bmatrix} \begin{bmatrix} i_s \\ v_{dc} \end{bmatrix} + \frac{1}{v_{dc}} \begin{bmatrix} \frac{1}{\tau'_s} \\ 1 \end{bmatrix} P + \begin{bmatrix} \frac{k_p}{\tau'_s} \\ 0 \end{bmatrix} v_{dc}^* \quad (3.3)$$

where p' denotes differentiation with respect to normalized time. From (3.3), it can be seen that the equilibrium state is

$$i_{s,e} = P \quad (3.4)$$

$$v_{dc,e} = v_{dc}^* = 1 \quad (3.5)$$

The stability of the equilibrium point can be established by linearizing (3.3) about the equilibrium point, and plugging in selected values of k_p , τ'_s , and P . The Jacobian Matrix \mathbf{A} is shown below, where $v_{dc,e}$ has been replaced with its per-unit value of 1.

$$\mathbf{A} = \begin{bmatrix} -\frac{1}{\tau'_s} & -\frac{k_p+P}{\tau'_s} \\ 1 & P \end{bmatrix} \quad (3.6)$$

The characteristic polynomial can be found, and the poles of the system can be placed, ensuring small-displacement stability. Using Routh's Stability Criterion, it can be seen that if $k_p > 0$ and $\tau'_s > \frac{1}{P}$, then the system will be locally stable. The characteristic equation is:

$$0 = \tau'_s \lambda^2 + (1 - P\tau'_s)\lambda + k_p \quad (3.7)$$

Up until this point, it has been assumed that control limits have not been reached, and that the input disturbance is small. However, in the presence of large disturbances, i_s will overshoot its equilibrium point, which implies that the source must be able to handle power levels greater than 1 pu for short spans of time. Obviously, a source cannot handle arbitrarily large power pulses, regardless of duration, and as such, it becomes important to determine the minimum transient overload capacity required to maintain stability. In normalized time, a search was performed to find the minimum necessary transient overload capacity for a single step change in CPL, the results of which are shown in Figure 3.2. That is to say, for a given normalized time constant τ'_s , the source current must be allowed to go to 1 plus a number on or above the line shown.

Upon selecting a normalized time constant and appropriate transient overload capacity, the eigenvalues of the linearized state transition matrix can be evaluated to

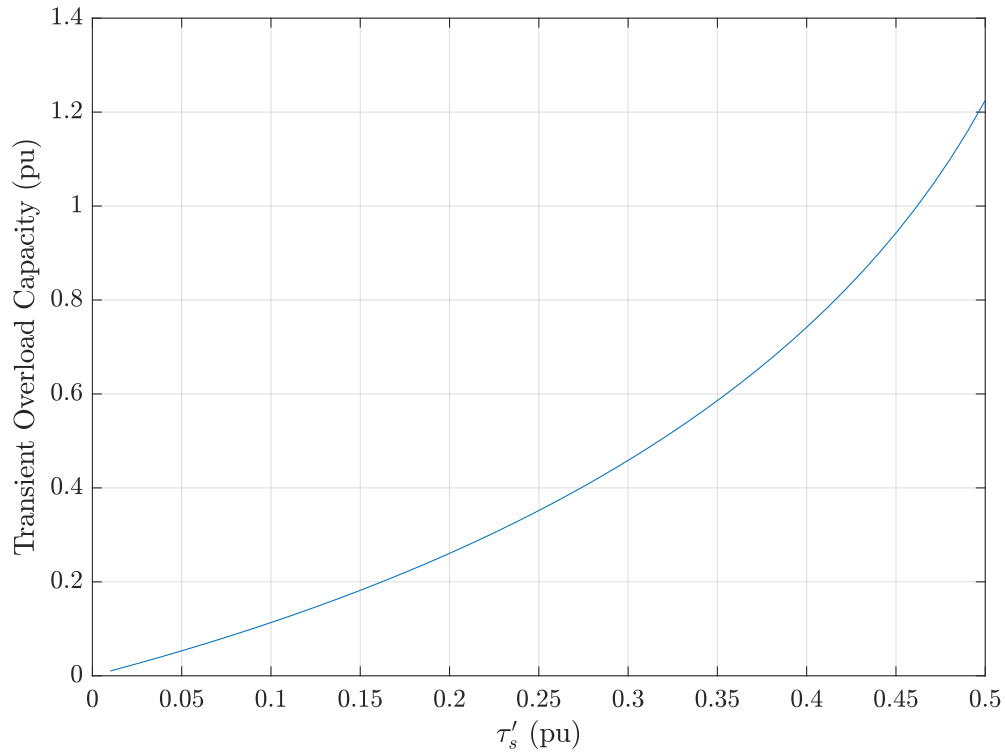


Fig. 3.2.: Minimum transient overload capacity with respect to normalized time constant.

determine if the equilibrium point is small displacement stable. The parameters in Table 3.1 were used to perform simulations. The eigenvalues of the Jacobian matrix of the scaled-time system were calculated to be $-1,027.40 \pm j1,906.77$, indicating that the system is small-displacement stable. With a locally stable equilibrium point, it is possible to numerically establish the RAS.

3.2 RAS and RLDS Estimation

The RAS for a 1-pu (rated) constant-power load applied to the single-source dc system is shown in Figure 3.3. To establish the RAS for a given equilibrium point, one state is initialized to a fixed value, and a bisection method search is implemented

Table 3.1.: Simulation Parameters for single-source dc system.

Parameter	Value (unit)
C	1.46 (ms)
τ_s	0.292 (ms)
k_p	5 (pu)

along the other state to search for the minimum value of that state to maintain stability. After that minimum value is established, the first state is incremented, and the search repeats.

To better illustrate the state vector's behavior during transients, several sample trajectories were superimposed on the RAS. This is shown in Figure 3.4. It can be seen that the state vector never leaves the RAS if it is inside the RAS, and it never enters the RAS if it starts outside the RAS.

The study performed to determine the RAS can be repeated for a range of inputs P to determine if the RLDS exists, and if it contains the RSSE. In this case, the RSSE is the line on which $v_{dc} = 1$ and $i_s = P$, where P can vary continuously from 0 to 1 pu. The RAS's for selected different loads on the single-source dc system are shown in Figure 3.5. While it is impossible to test every possible allowable input, and therefore impossible to say for certain that the RLDS exists and takes a certain shape, it is assumed that if there is a space common to a set of RAS's corresponding to a wide range of allowable inputs, we can claim with high confidence that the common space is the RLDS. It can be seen that the RAS for a P of 1 pu is the intersection of all RAS's displayed. Therefore, it can be concluded that the RLDS is the RAS for a 1 pu step change in constant-power load. It can also be seen that the RLDS wholly contains the RSSE in Figure 3.5. By the definitions set forth in Chapter 2, the system will be Single-Step Stable.

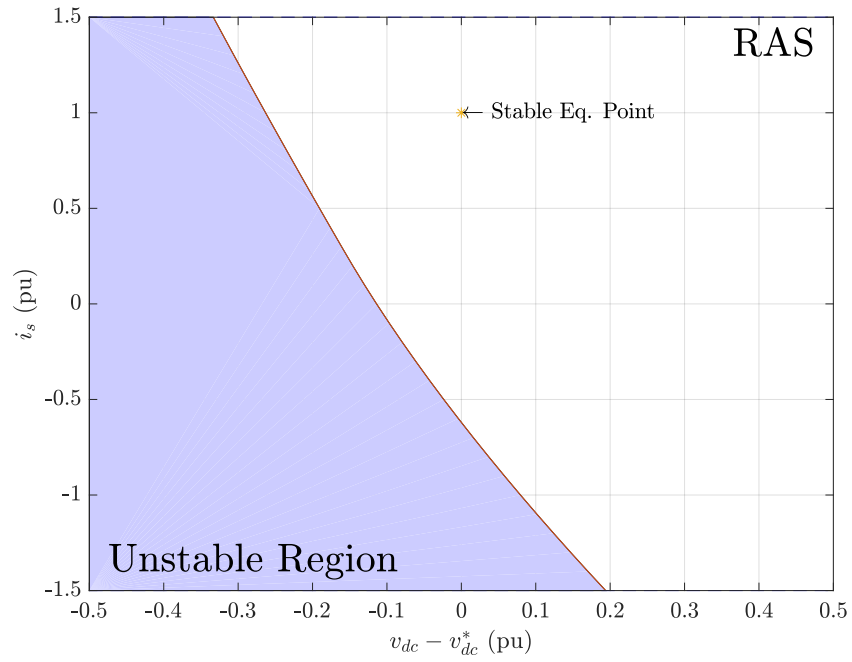


Fig. 3.3.: The RAS for a $P = 1$ pu.

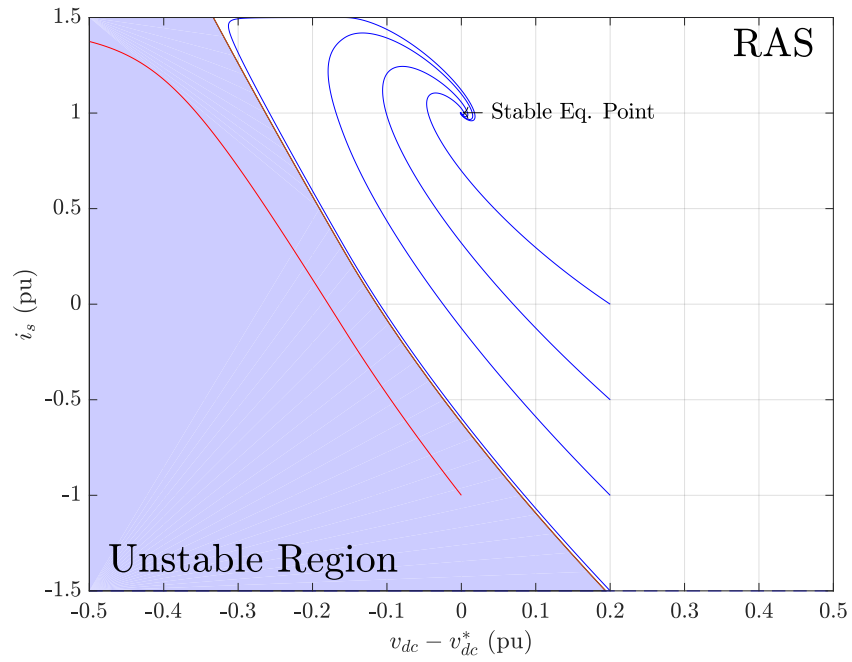


Fig. 3.4.: The trajectories of the system under a 1 pu step-change in CPL.

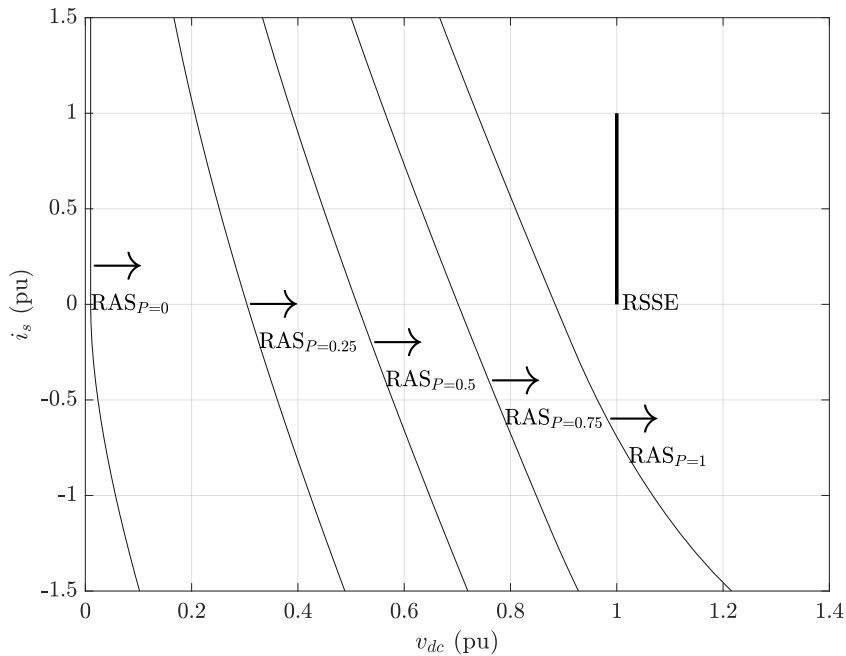


Fig. 3.5.: The RAS's corresponding to different inputs to the single-source dc system.

3.3 Reachable State Space Estimation

It is necessary to determine the boundary of the reachable state-space in order to determine the LDSM of the system, though this task is highly nontrivial. In general, establishing reachable sets of a dynamical system involves performing calculations based on initial states and finite time horizons. Several algorithms and toolboxes exist to perform these searches, notably CORA [29], but in general, these tools are developed to find the reachable set over a finite time horizon, and return convex over-approximations of the reachable set [30–32]. In this research, however, in order for the LDSM to exist, the RSS must be bounded over an infinite time horizon. Additionally, it is desired that the estimated RSS be as tight an approximation as possible, without assuming that the results are convex.

Assuming that such a boundary could be established, it is noted that the state-derivative would be either tangential to the boundary, or would point to the interior of

the space. Furthermore since there are many such closed surfaces that could satisfy this criteria, it is also noted that the boundary of the RSS should be the closed surface that satisfies the derivative condition, but also encloses the smallest possible area (or more generally, hypervolume). To understand this, it is helpful to consider a trajectory that starts on the inside of the RSS. If that trajectory were to come to intersect a surface on which the state derivative is tangential to or points inward for all possible inputs, the trajectory would continue to evolve, though not past the boundary with which it intersected, since the “velocity” of the state does not point past the boundary. Since the trajectory cannot exceed such a boundary, the first and only such boundary the trajectory could intersect would be the one that encloses the smallest possible hypervolume.

To estimate the boundary of the RSS for the given system, a brute-force recursive search can be implemented. Qualitatively, the algorithm can be summarized by applying every input to the system initialized to a certain point, and then applying every input to the system after each ensuing trajectory is allowed to evolve over a small time horizon. The state space is discretized into a set of rectangles (referred to as domains), each initially marked with a logical 0. As each simulated trajectory traverses the state space, each domain it traverses is marked a logical 1. When the trajectory arrives at the equilibrium point corresponding to the input that drives it, the search algorithm terminates. This process is summarized in Algorithms 1 and 2.

Algorithm 1 Main function to search for the reachable state-space of the dc system

reachable_set = false($N_{v_{dc}}, N_{i_s}$)

$x \leftarrow x_{eq}$

search_statespace(x, u_1)

search_statespace(x, u_2)

The shortcomings of this algorithm include the immense computational complexity as the number of inputs and states increase. Only a small sample of inputs can be tested while preserving memory, and as such the extremes of the input space are

Algorithm 2 search_statespace(x, u)

```
update  $x_{eq}$ 
while  $\|x - x_e\| > \epsilon$  do
   $px \leftarrow \text{state\_derivative}(x, u)$ 
   $x \leftarrow x + h px$ 
   $i, j \leftarrow \text{quantize}(x)$ 
  if reachable_set( $i, j$ ) = false then
    reachable_set( $i, j$ ) = true
    search_statespace( $x_k, u_1$ )
    search_statespace( $x_k, u_2$ )
  end if
end while
```

tested. However, since the input is changing at every fixed time-step, other inputs can be approximated as the average of two extreme inputs over several time-steps. For example, a step-change in load of 0.25 pu can be approximated by a repeating pattern of step changes in load, starting at 1 pu for one time-step, followed by a load of 0 pu for 3 time-steps. As the time-step is small, the average over a long time can reasonably approximate a wide array of continuously varying loads.

Furthermore, since this algorithm is memory intensive, the spatial discretization is limited. This limited resolution means that there is a degree of uncertainty in the final result. After the routine terminates, each domain index is mapped to the center of its corresponding rectangle in the state space, regardless of the path the trajectory took through that domain. As will be discussed in this section, the true boundary of the RSS, should it exist, will be within one domain-width of the final result obtained by the recursive search. In order to minimize uncertainty, a large number of domains and a small time-step is required. Taking this to extremes, however, will result in a significant computational burden, and so a balance is required.

Due to the discretization of the state space, it is difficult to numerically establish normal vectors to the established surface. As such, it is difficult to establish whether or not the state derivative lies tangential to the established surface. However, since the domains are recorded only when the state trajectory traverses that domain, and at each time-step of the simulation each input is applied to the trajectory, if it were possible for a trajectory to reach a new domain at the termination of the algorithm, it would do so. This can be seen by analyzing the state derivative at a fixed value of x . It can be seen in (3.2) that the state derivative is affine with respect to the input P . Since P is selected from a convex set U , and the state derivative is affine with respect to that input, the state derivative itself is a convex set at every fixed value

of x . To show this, a convex combination of $px = f(x, u)$ can be taken at different different inputs for the same x_k :

$$\begin{aligned} \alpha f(x_k, u_1) + (1 - \alpha)f(x_k, u_2) &= \\ \alpha \mathbf{A}x_k + \alpha \mathbf{B}_1(x_k)u_1 + \alpha \mathbf{B}_2 v_{dc}^* + (1 - \alpha)\mathbf{A}x_k + (1 - \alpha)\mathbf{B}_1(x_k)u_2 + (1 - \alpha)\mathbf{B}_2 v_{dc}^* &= \\ \mathbf{A}x_k + \mathbf{B}_1(x_k)(\alpha u_1 + (1 - \alpha)u_2) + \mathbf{B}_2 v_{dc}^* & \quad (3.8) \end{aligned}$$

where \mathbf{A} is the matrix premultiplying $[i_s \ v_{dc}]^T$ in (3.2), $\mathbf{B}_1(x)$ is the vector premultiplying P in (3.2), \mathbf{B}_2 is the vector premultiplying v_{dc}^* in (3.2), and $\alpha \in [0, 1]$. For brevity, the results from when the current command limit is reached are not discussed herein, though it can be seen that similar conclusions are established under such conditions.

Since u_1 and u_2 are taken from convex set U , $(\alpha u_1 + (1 - \alpha)u_2) \in U$. If u_1 and u_2 are taken to be the extremes of U , then the state derivative will vary between the derivative corresponding to u_1 to the derivative corresponding to u_2 as α varies from 1 to 0. It can be seen, then, that if there were an input that would drive the state trajectory in a direction beyond the boundary, the search would apply inputs that result in a derivative that points at least partially in that direction. Since the boundary is established, no applied input results in a derivative that points outside that boundary, and therefore the established boundary represents a conservative approximation of the boundary of the RSS. If there is a component of the derivative that points away from the boundary, it is small enough that the trajectory never enters a domain further away from what is established. The trajectory that traverses the boundary of the RSS might lead away from the center of the domain, however, and as such a maximum error introduced by the spatial discretization must be quantified. The maximum error produced by this method can be expressed:

$$\text{error} = \frac{1}{2} \sqrt{x_{1,\text{dom}}^2 + x_{2,\text{dom}}^2} \quad (3.9)$$

where $x_{i,\text{dom}}$ is the width of a domain along the i^{th} axis. This error corresponds to the distance from the center of a domain to the corner of a domain, which is the maximum

Table 3.2.: RSS search parameters for the dc system

Parameter	Value
$N_{v_{dc}}$	350
N_{i_s}	450
$v_{dc,\max}$ (pu)	1.5
$v_{dc,\min}$ (pu)	0.5
$i_{s,\max}$ (pu)	1.8
$i_{s,\min}$ (pu)	-1.8

distance a trajectory could be from the center of a domain while still marking that domain a 1.

For the system described in this chapter, this search was executed with parameters shown in Table 3.2, in which N_k refers to the number of domains along the k axis, and f_{\min} and f_{\max} refer to the upper and lower search bounds along the respective axes. With these search boundaries and domains, the maximum error between the estimated RSS and the true RSS boundary is 0.0042 pu. The RSS was estimated with 2 loads: $u_1 = 1$ pu and $u_2 = 0$.

The calculated RSS and RLDS can be seen in Figure 3.6. It can be seen that there is a separation between the boundaries. The smallest distance between these two boundaries can be calculated by a brute-force search. In nested `for` loops, the norm of the difference of each point along each boundary is calculated. Using this approach, the LDSM was calculated to be 0.066. Assuming conservatively that the true boundary of the RSS is maximally far from the estimated boundary, the LDSM for this system is 0.062.

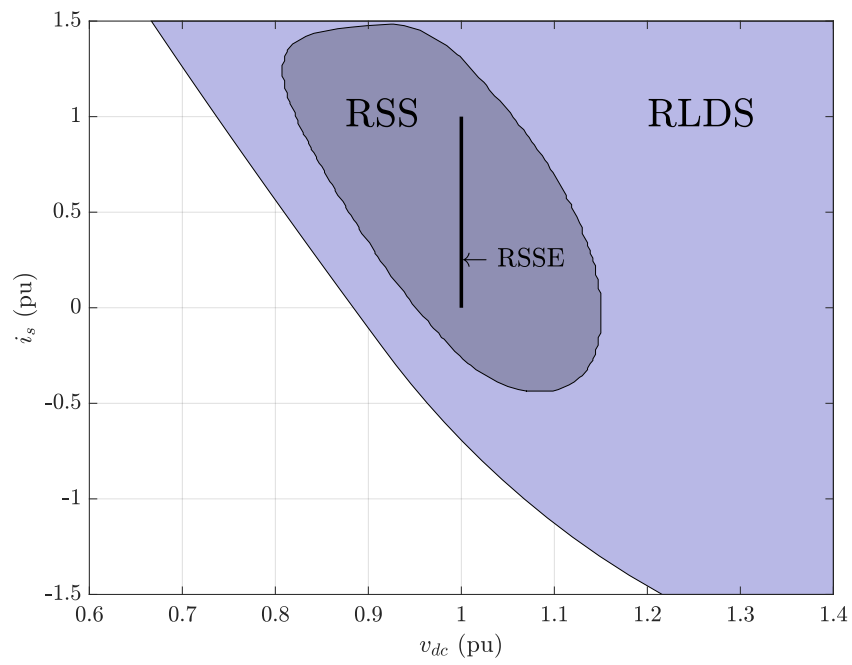


Fig. 3.6.: The RSS and RLDS of the two dimensional dc system. The given system is large-displacement stable (LDS) with a large-displacement stability margin (LDSM) of 0.091.

3.4 Permanent-Magnet Generator with Active Rectifier

The system studied in the previous section has two states. Consequently, the RSS and RLDS can be displayed in two dimensions. In a practicable implementation of the system depicted in Figure 3.1, the current source could be replaced with a permanent-magnet generator feeding an active rectifier. This system is studied in [3] and [28], and introduces additional states in the form of the q - and d -currents in the electric machine as described by Park's equations [33].

The dynamics of a P -pole permanent-magnet generator (neglecting the zero sequence) can be expressed with reasonable accuracy in the rotor reference frame as

$$v_{qs}^r = r_s i_{qs}^r + \omega_r L_d i_{ds}^r + \omega_r \lambda'_m + L_q \frac{di_{qs}^r}{dt} \quad (3.10)$$

$$v_{ds}^r = r_s i_{ds}^r - \omega_r L_q i_{qs}^r + L_d \frac{di_{ds}^r}{dt} \quad (3.11)$$

with the electromagnetic torque expressed as

$$T_e = \frac{3P}{2} (\lambda'_m i_{qs}^r + (L_d - L_q) i_{qs}^r i_{ds}^r) \quad (3.12)$$

where v_{qs}^r and v_{ds}^r are the q - and d -axis stator voltages, i_{qs}^r and i_{ds}^r are the q - and d -axis stator currents, r_s is the stator resistance, L_q and L_d are the q - and d -axis inductances, ω_r is the electrical rotor speed in radians per second, and λ'_m is the flux linkage due to the permanent magnet. These equations assume positive current flows into the machine.

To control the currents out of the machine, a control law is defined to set the stator voltages to achieve desired currents. First, feedforward terms are defined to decouple the respective current responses as follows:

$$v_{qs,ff}^{r*} = r_s i_{qs}^r + \omega_r L_d i_{ds}^r + \omega_r \lambda'_m \quad (3.13)$$

$$v_{ds,ff}^{r*} = r_s i_{ds}^r - \omega_r L_q i_{qs}^r \quad (3.14)$$

To place closed-loop poles in desired locations, feedback is incorporated into the control. To limit system dimension, a pure proportional controller is selected, though

commonly proportional-integral control is used. This choice results in steady-state error in the system response, though the error is small enough to be neglected. The control law for each current can be expressed

$$v_{qs}^{r*} = k_{p,ac}(i_{qs}^{r*} - i_{qs}^r) + v_{qs,ff}^{r*} \quad (3.15)$$

$$v_{ds}^{r*} = k_{p,ac}(i_{ds}^{r*} - i_{ds}^r) + v_{ds,ff}^{r*} \quad (3.16)$$

where $k_{p,ac}$ is the proportional gain. In a switching converter using Space-Vector Modulation or Sine-Triangle Modulation [33] to determine switch states, the commanded stator voltages can be substituted into (3.10) and (3.11) to arrive at a transfer function for the stator currents' response to their commands:

$$\frac{i_{qs}^r}{i_{qs}^{r*}} = \frac{1}{\frac{L_q}{k_{p,ac}}s + 1} \quad (3.17)$$

with a similar relationship between the d -axis current and its command.

The dc link voltage is controlled using the same control law as the two-dimensional system studied in the previous sections. The control law is given by (3.1). Since the dc current is a function of the ac current out of the machine, a relationship must be established to generate a q -axis current command. The commanded dc current is multiplied by the dc link voltage to generate a power command, which is then divided by the rotor speed ω_r to produce a torque command. The torque command is mapped to a current command using (3.12). The d -axis current is commanded to 0 to minimize losses in the generator. This mapping can be expressed as

$$i_{qs}^{r*} = -\frac{i_{dc}^* v_{dc}}{\frac{\omega_r}{\omega_b} \frac{3}{2} \frac{P}{2} \lambda'_m} \quad (3.18)$$

with the inclusion of the negative sign due to the dc current being defined as being positive into the load, and the q -axis current being defined as positive into the machine.

The load is modelled as an ideal step change, with the load current described by that step change divided by v_{dc} .

$$i_{\text{load}} = \frac{P}{v_{dc}} \quad (3.19)$$

Table 3.3.: Generator-Rectifier System Parameters

Parameter	Value (unit)	Description
P_b	50 (kW)	Rated Power
ω_b	$2\pi 400$ (rad/s)	base (rated) frequency
$V_{b,dc}$	270 (V)	base (rated) dc voltage
$I_{b,dc}$	185 (A)	base (rated) dc current
$V_{b,ac}$	108 (V)	rated peak ac phase-to-neutral voltage
$I_{b,ac}$	309 (A)	rated peak ac phase-to-neutral current
$\omega_b L_q$	0.33 (pu)	PMAC q -axis reactance
$\omega_b L_d$	0.33 (pu)	PMAC d -axis reactance
r_s	0.01 (pu)	PMAX stator resistance
$\omega_b \lambda'_m$	1 (pu)	PMAC back emf at rated speed
C	1.46×10^{-3} (pu)	dc bus capacitance
$k_{p,ac}$	5 (pu)	stator current regulator proportional gain
G	2 (pu)	dc voltage regulator proportional gain

The RAS's used to establish the RLDS, as well as the RSS, were established using an average-value model of this system with all variables expressed in per unit. The per unit bases used to normalize states, as well as system parameters in per unit are listed in Table 3.3. To find the surfaces of these spaces, similar algorithms to what were described earlier in this chapter were used.

To summarize finding the boundary of each RAS, two of the three states in the system were initialized to a fixed value, and a bisection method search was performed along the third state to establish the minimum required value of that state to maintain stability for a step change in load of a given value. The boundaries of each RAS can be superimposed, and the resulting volume common to all regions is taken to be the RLDS. It can be seen in Figure 3.7 that as the load increases, the size of the RAS

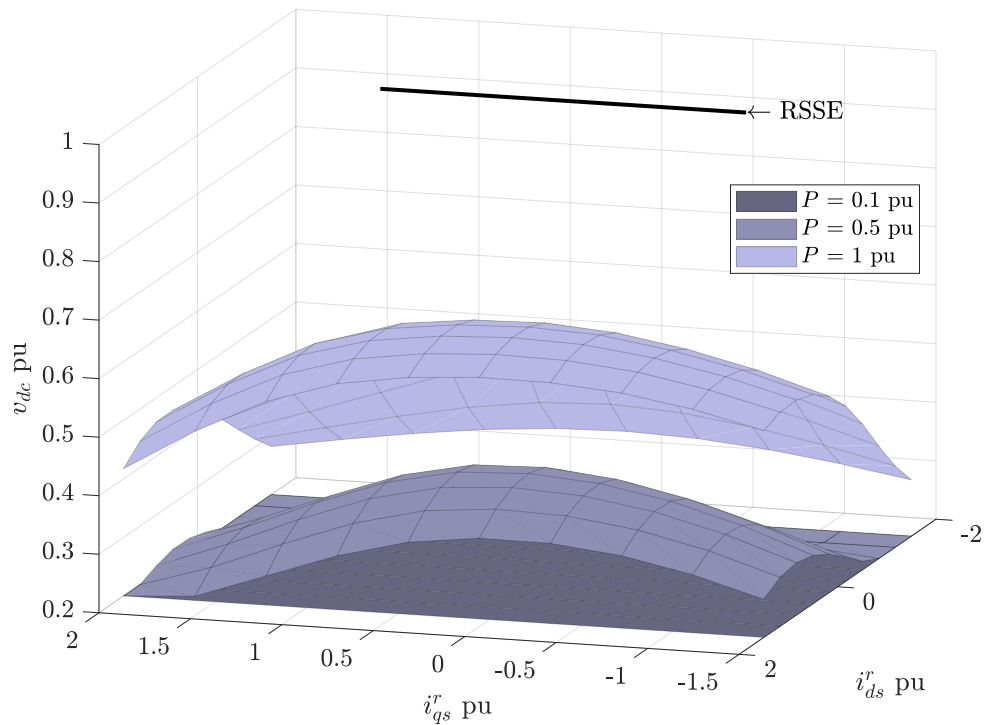


Fig. 3.7.: Three RAS boundaries superimposed. The RLDS = $RAS_{P=1}$. Since $RSSE \subset RLDS$, the system is single-step stable.

corresponding to that load shrinks and is contained by all RAS's corresponding to smaller loads. Therefore, the RAS corresponding to a P of 1 pu is the RLDS.

With the RLDS established, it is necessary to establish the RSS. Algorithm 1 can be implemented with a version of Algorithm 2 to account for the increase in system order. In the modified version of Algorithm 1, an additional index is added as an output of the quantize function, and the state derivative function is replaced with an the average-value model of the machine-rectifier system, rather than that of a simple current source.

The RSS can be seen above the boundary of the RLDS in Figure 3.8. The parameters used to establish this space can be found in Table 3.4. For this study, it was assumed that power could be supplied by the machine, or supplied to the machine.

Table 3.4.: RSS search parameters for the machine-rectifier system

Parameter	Value
$N_{v_{dc}}$	150
$N_{i_{qs}^r}$	150
$N_{i_{ds}^r}$	100
$v_{dc,\max}$ (pu)	1.5
$v_{dc,\min}$ (pu)	0.5
$i_{qs,\max}^r$ (pu)	1.8
$i_{qs,\min}^r$ (pu)	-1.7
$i_{ds,\max}^r$ (pu)	0.2
$i_{ds,\min}^r$ (pu)	-0.3

For this reason, the input power was bounded between positive and negative 1 pu. The extremes used in the search for the RSS boundary were $u_1 = 1$ pu and $u_2 = -1$ pu.

The true boundary of the RSS would be within one domain of the boundary shown in Figure 3.8. The maximum possible error between the two boundaries can be established by applying a version of (3.9) modified to include a third domain. Applying this equation with the parameters listed in Table 3.4, the maximum distance between the boundary established and the true boundary is 0.0124 pu.

To establish the LDS, a brute force search was implemented to calculate the norm of the distance between every combination of points on the boundary of the RSS and the RLDS, as was done in the two-dimensional case earlier in this chapter. The LDSM was found initially to be 0.3325, but since the true boundary could be as far as 0.0124 pu away from the points found in the search, the LDSM is stated conservatively to be 0.32 pu. Based upon these results, the given system is considered large-displacement stable with a sizable stability margin.

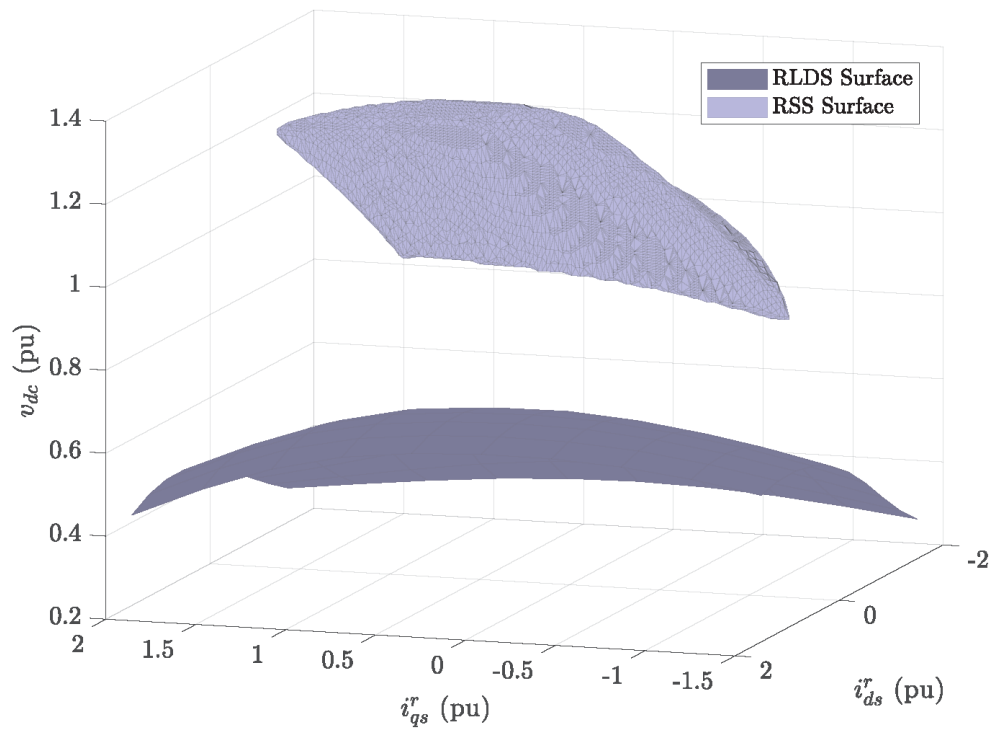


Fig. 3.8.: The RSS and RLDS of the machine rectifier system. Since $\text{RSS} \subset \text{RLDS}$; the system is defined to be large-displacement stable with a stability margin of 0.32.

4. ENSURING LARGE-DISPLACEMENT STABILITY IN AC SYSTEMS

In the previous chapters, it was observed for the dc system studied in [3] that selecting large values of voltage feedback constant, current limit, and dc bus capacitance, as well as a small value of current source time constant result in a larger RLDS and more stable system. The trade-off between capacitance and transient overload capacity was investigated for a particular value of voltage feedback constant, but the relationship between all variables and their impact on the size of the RLDS was not fully investigated. To explore the effect of increasing or decreasing a particular control parameter in the dc system with a given architecture, a space can be envisioned where each axis describes one parameter and the LDSM for that set of parameters. There are four independent and one dependent parameter that have an impact for the dc system, but if a traditional pole-placement-based controller design is used, it can be seen that both the voltage feedback constant and current source time constant depend directly on switching frequency, and hence for the variables of interest, the parameter-space is 4-dimensional. This boundary is important to establish not only to understand the trades that exist between different controller parameters, but also to understand the impact of parameters such as i_{lim} that do not appear in traditional eigenvalue analysis.

Extending this principle to the ac system, it is also easily seen that switching frequency, capacitive reactance, and current limits will be the variables of interest. In general, it is possible to limit the q -axis and current magnitude independently [24]. However, to simplify the description of the parameter space boundary in this thesis, it is assumed that the the q -axis current limit is the same as the current magnitude limit.

In this chapter, a control architecture is set forth for an example ac system with a three-phase current source feeding a capacitor bank, which in turn feeds a constant-apparent-power load. A brute-force search is then implemented to check each of a set of combinations of switching frequency, capacitance, and current limits for stability of the given system model. Parameters are selected from this search to result in a highly stable system, and the RLDS and RSS are established. Finally, the Belkhayat criterion is evaluated for the selected system to demonstrate that that an LDS system easily satisfies this small-displacement criterion.

4.1 Ac System Model and Controller Design

The system being studied is a non-ideal, three-phase current source feeding a wye-connected capacitor bank with floating neutral point, which in turn feeds a constant apparent-power load. The system is shown in Figure 4.1. As was the case in Chapter 3, the term “Constant-Apparent-Power Load” refers to a class of loads which draw current in such a way as to maintain a constant power draw. As such, as the voltage across the load decreases, the current draw will increase to compensate. It is sometimes true that the power drawn by the load is constant, though in general this need not be the case. Just as the dc system studied in Chapter 3 might undergo a time-varying power load $P(t)$, so too can the system studied in this chapter draw a load with real and reactive components $P(t)$ and $Q(t)$, respectively.

In a three-phase power system, the total power being delivered to any point in the system can be expressed

$$P_{\text{total}} = v_a i_a + v_b i_b + v_c i_c \quad (4.1)$$

where v_x , $x \in \{a, b, c\}$ is the peak line-to-neutral voltage of phase x and i_x is the peak current carried by line x [34]. Assuming that the sinusoidal voltages and currents have the same amplitude and are mutually displaced by 120° , and that time $t = 0$

is defined such that there is no phase shift on the a -phase voltage, the a -phase's contribution to power can be expressed

$$P_{a\text{-phase}} = \frac{1}{2}v_p i_p (\cos \phi (1 + \cos 2\omega t) + \sin \phi \sin 2\omega t) \quad (4.2)$$

where v_p is the peak line-to-neutral voltage of each phase, i_p is the peak line current of each phase, ω is the frequency of the voltages and currents in radians per second, and ϕ is the phase shift between the voltage and current waveforms. There are similar expressions for the b -phase and c -phase's power which include a phase shift in the time-dependent sinusoidal terms corresponding to the phase shift in the voltages and currents. In steady-state, ϕ will be constant, and it can be seen that the average value P of the total power being transferred on each individual phase, referred to as real power, is

$$P = \frac{1}{2}v_p i_p \cos \phi \quad (4.3)$$

The second term in (4.2) is referred to as the reactive component of the load, and represents the component of power that is not dissipated. The peak of the reactive power Q is defined on a per-phase basis as

$$Q = \frac{1}{2}v_p i_p \sin \phi \quad (4.4)$$

Additionally, it is noted that the square root of the sum of the squares of real and reactive power is equal to three halves the product of the peak line-to-neutral voltage and peak current of each phase. This product is henceforth referred to as apparent power.

$$S = \sqrt{P^2 + Q^2} = \sqrt{\left(\frac{1}{2}v_p i_p\right)^2 \cos^2 \phi + \left(\frac{1}{2}v_p i_p\right)^2 \sin^2 \phi} = \frac{1}{2}v_p i_p \quad (4.5)$$

Extending these results to three-phase systems, it can be seen that the total power transferred is equal to three times the average power transferred by each individual phase, and that the reactive power contribution from each phase cancel one another out. This is because reactive power represents the rate of change of energy stored in inductive and capacitive elements which is not converted to other forms of energy such

as thermal or kinetic energy. Despite the fact that reactive power is not transferred in a three-phase system, it is still necessary to define Q for a three-phase system to account for phase shifts in current which occur for different types of loads. Real and reactive power for a three-phase system can each be expressed as three times their single phase counterparts, or

$$P = \frac{3}{2}v_p i_p \cos \phi \quad (4.6)$$

$$Q = \frac{3}{2}v_p i_p \sin \phi \quad (4.7)$$

with three-phase apparent power defined as

$$S = \sqrt{P^2 + Q^2} = \frac{3}{2}v_p i_p \quad (4.8)$$

Performing system studies in real variables is often disadvantageous, since state variables in this frame of reference are sinusoidal, which presents challenges in designing controllers. The reference frame transformation defined by (1.6) is used to express variables in the synchronous reference frame, which ensures that they will be constant in the steady-state. All system studies in this chapter are performed in the synchronous reference frame, and as such it is necessary to express real and reactive power in terms of voltages and currents in that reference frame. To do this, (4.1) can be expressed in vector form as

$$P_{\text{total}} = \begin{bmatrix} i_a & i_b & i_c \end{bmatrix} \begin{bmatrix} v_a \\ v_b \\ v_c \end{bmatrix} = \mathbf{i}_{abc}^T \mathbf{v}_{abc} \quad (4.9)$$

Each vector \mathbf{f}_{abc} , $\mathbf{f} \in \{\mathbf{v}, \mathbf{i}\}$ can be substituted for its transformed counterpart multiplied by the inverse transformation matrix $\mathbf{K}_e^{-1} \mathbf{f}_{qd0}$ to arrive at

$$P = \frac{3}{2} (v_q i_q + v_d i_d + 2v_0 i_0) \quad (4.10)$$

In balanced or 3-wire ac systems, the zero-sequence component of voltage and current are both zero identically 0 by virtue of Kirchoff's voltage and current laws, and so the

zero-sequence component of power is henceforth neglected. It is important to note that the transformation into the synchronous reference frame only yields an expression for the real component of power P . To determine an expression for reactive power in terms of voltages and currents in the synchronous reference frame, (4.10) can be substituted into (4.8) along with the expressions $v_p = \sqrt{v_q^2 + v_d^2}$ and $i_p = \sqrt{i_q^2 + i_d^2}$. Simplifying this expression, Q can be expressed

$$Q = \frac{3}{2} (v_q i_d - v_d i_q) \quad (4.11)$$

The real and reactive power P and Q consumed by the load can be represented in per unit and in matrix form by:

$$\begin{bmatrix} P \\ Q \end{bmatrix} = \begin{bmatrix} v_q & v_d \\ -v_d & v_q \end{bmatrix} \begin{bmatrix} i_{qL} \\ i_{dL} \end{bmatrix} \quad (4.12)$$

where i_{qL} is the q -axis component of load current and i_{dL} is the d -axis component of load current in the synchronous reference frame, and v_q and v_d are the q - and d -axis bus voltages in the synchronous reference frame.

While a current source behavioral model is studied in this work, it is possible to arrive at identical results from a control and stability perspective with a current-regulated voltage source converter feeding an LC filter, given a sufficiently large dc link voltage. The dynamics of the filter inductor currents \mathbf{i}_{qdI} in the voltage source case can be expressed in the synchronous reference frame as

$$Lp\mathbf{i}_{qdI} = \mathbf{v}_{qdI} - \mathbf{v}_{qd} - \omega_e L \begin{bmatrix} 0 & 1 \\ -1 & 0 \end{bmatrix} \mathbf{i}_{qdI} \quad (4.13)$$

where \mathbf{v}_{qdI} are the line to neutral inverter voltages in the synchronous reference frame, \mathbf{v}_{qd} are the line to neutral capacitor voltages in the synchronous reference frame, \mathbf{i}_{qdI} are the inductor currents in the synchronous reference frame, L is the filter inductance and ω_e is the fundamental frequency of the output voltages and currents. A control

law is defined which determines \mathbf{v}_{qdI} such that the the closed-loop current response is first-order. This control law can be expressed as

$$\mathbf{v}_{qdI} = k_{pI} (\mathbf{i}_{qdI}^* - \mathbf{i}_{qdI}) + \mathbf{v}_{qd} + \omega_e L \begin{bmatrix} 0 & 1 \\ -1 & 0 \end{bmatrix} \mathbf{i}_{qdI} \quad (4.14)$$

In general, it is standard to place the closed-loop pole of the innermost loop a decade below the switching frequency of the converter. This is achieved by setting k_{pI} to $\frac{L2\pi f_{sw}}{10}$.

The inductors in the LC filter are included to lower current ripple in the output of the converter. Similarly, the capacitors are placed to limit voltage ripple, but there is the additional benefit of both components in the filter of energy storage. The capacitors will store much more energy than the inductors for the design considered in this thesis. For this reason, as well as the identical performance in respective average value models, for the remainder of this chapter a current source will be considered with a non-instantaneous response, rather than considering a voltage source feeding an inductor. The current source is assumed to have a transfer function of the form:

$$\mathbf{i}_{qdI} = \frac{1}{\tau s + 1} \mathbf{i}_{qdI}^* \quad (4.15)$$

where \mathbf{i}_{qdI}^* are the commanded q - and d -axis source currents in the synchronous reference frame.

The q - and d -axis filter capacitor voltage dynamics can be expressed in the synchronous reference frame as

$$p\mathbf{v}_{qd} = \omega_b X_{Cac} (\mathbf{i}_{qdI} - \mathbf{i}_{qdL}) + \omega_e \begin{bmatrix} 0 & -1 \\ 1 & 0 \end{bmatrix} \mathbf{v}_{qd} \quad (4.16)$$

where ω_b is the base frequency of the system, X_{Cac} is the reactance of the capacitor in per-unit, and \mathbf{i}_{qdL} are the q - and d -axis load currents in the synchronous reference frame. Under the assumption that \mathbf{i}_{qdI} changes near-instantaneously with respect to their commands, a controller can be designed to attain a first order response with respect to the commanded output voltages \mathbf{v}_{qd}^* .

Since it is required that the closed-loop pole of the current control loop be an order of magnitude faster than the voltage control loop, the controller gains can be determined to achieve a pole location at $-2\pi f_{sw}/100$. A proportion control law with a feedforward component can be defined as

$$\mathbf{i}_{qdI}^{**} = k_{pv}(\mathbf{v}_{qd}^* - \mathbf{v}_{qd}) + \mathbf{i}_{qdL} + \frac{\omega_e}{\omega_b X_{Cac}} \begin{bmatrix} 0 & 1 \\ -1 & 0 \end{bmatrix} \mathbf{v}_{qd} \quad (4.17)$$

Were it possible to command arbitrarily large currents, the controller design could stop here. However, a practicable inverter cannot be designed to handle arbitrary currents for, even in short bursts. There may be instances where the q - and d -axis current commands become too large, and so a limiting function is applied. The commands are limited using the **sat** function as follows:

$$i_{qI}^* = \mathbf{sat}(i_{qI}^{**}, i_{lim}) \quad (4.18)$$

$$i_{dI}^* = \mathbf{sign}(i_{dI}^{**}) \sqrt{\mathbf{sat}(i_{qI}^{*2} + i_{dI}^{**2}, i_{lim}^2)} - i_{qI}^{*2} \quad (4.19)$$

The **sat** function limits its first input to the second input when the first input is positive, and limits the first input to the negative of the second input when the first input is negative. The **sign** function returns a positive 1 when the input is positive, a negative 1 when the input is negative, and 0 when the input is 0.

Assuming that command limits are not reached, however, and that \mathbf{i}_{qdI} respond instantaneously to their command, a transfer function can be established of the form

$$\mathbf{v}_{qd} = \frac{1}{\frac{1}{k_{pv}\omega_b X_{Cac}}s + 1} \mathbf{v}_{qd}^* \quad (4.20)$$

It is desired for this loop of the control to have a closed-loop time constant of $\tau_v = 100/(2\pi f_{sw})$ and thus, k_{pv} must equal $2\pi f_{sw}/(100\omega_b X_{Cac})$ to achieve a closed-loop pole in the desired location.

To express the load currents in terms of net load power, (4.12) can be solved for \mathbf{i}_{qdL} to obtain

$$\begin{bmatrix} i_{qL} \\ i_{dL} \end{bmatrix} = \frac{1}{v_q^2 + v_d^2} \begin{bmatrix} v_q & -v_d \\ v_d & v_q \end{bmatrix} \begin{bmatrix} P \\ Q \end{bmatrix} \quad (4.21)$$

It can be seen that all control parameters using traditional pole-placement controller design strategies are directly dependent on switching frequency, ac bus capacitance, and current command limits. While the poles of the transfer functions depend on f_{sw} , and X_{Cac} , it is more difficult to take into account the effect i_{lim} has on system performance. Additionally, since the poles depends on the ratio of switching frequency and filter reactances, there are infinitely many combinations of those parameters that result in the same pole location, but different overall system performance. Finally, closed-loop poles are useful in stability analysis, though their impact is made less clear by the nonlinearities introduced by the CSL and current limits. It is known that in systems with constant power loads, the capacitor voltages change rapidly with respect to source current, which contradicts the assumption made in designing the controller that current would rise near instantaneously with respect to bus voltage, and hence analyzing the poles is not sufficient to determine the stability of the system response.

To facilitate understanding the impact of each parameter on Large-Displacement stability, a parameter space is defined in which the axes represent parameters of the system and the LDSM. A brute-force search was implemented to check a broad sampling of combinations of f_{sw} , X_{Cac} , and i_{lim} . At each combination of those three values, the minimum necessary q -axis capacitor voltage was established for a 1 pu step change in real power load.

4.2 Parameter-Space Search

For a given system architecture, it is desired to know the set of parameters that results in the largest possible LDSM. However, due to computational complexity, the LDSM was not established in the parameter space search performed in this thesis, since the algorithms used to establish the RLDS and the RSS are both computationally intensive. Instead, a search was performed to search for the minimum necessary q -axis voltage to maintain stability for a step-change in real-power load from 0 to 1

Table 4.1.: The range of parameters over which the parameter space was searched.

Parameter	minimum value (unit)	maximum value (unit)
f_{sw}	10 (kHz)	100 (kHz)
i_{lim}	1.1 (pu)	1.5 (pu)
X_{Cac}	5 (pu)	14 (pu)

pu with the state initialized to the origin. It is assumed in this search that having a small minimum-necessary v_q results in a large LDSM.

A vector was defined for each parameter of interest, with elements spanning a broad range of possible values for that parameter. For each combination of parameters, the system was initialized to the equilibrium point associated with zero load, and a trajectory was simulated for a real-power load of 1 pu stepped at $t = 0$. Depending on the stability of the ensuing trajectory, the simulation is repeated with the q -axis voltage reinitialized based on a bisection method search, in which the initial voltage is reduced if the previous trajectory was stable, and increased if it was not. After a fixed number of iterations, the system parameters are updated, and the search begins anew.

The average value model was exercised over 125 sets of parameters, corresponding to five values of each individual parameter. The range of each parameter is shown in Table 4.1. At each combination of values, the bisection method search was executed 12 times.

A projection of the parameter space boundary estimate can be seen in Figure 4.2. It can be seen in that figure that as switching frequency decreases, the minimum necessary q -axis voltage generally increases. This implies that faster switching frequencies, which enable faster poles to be placed, lend themselves well to designing systems for stability. Additionally, it can be seen that for a switching frequency of 10 kHz, it is impossible at any value of i_{lim} or X_{Cac} to maintain stability for a 1 pu step

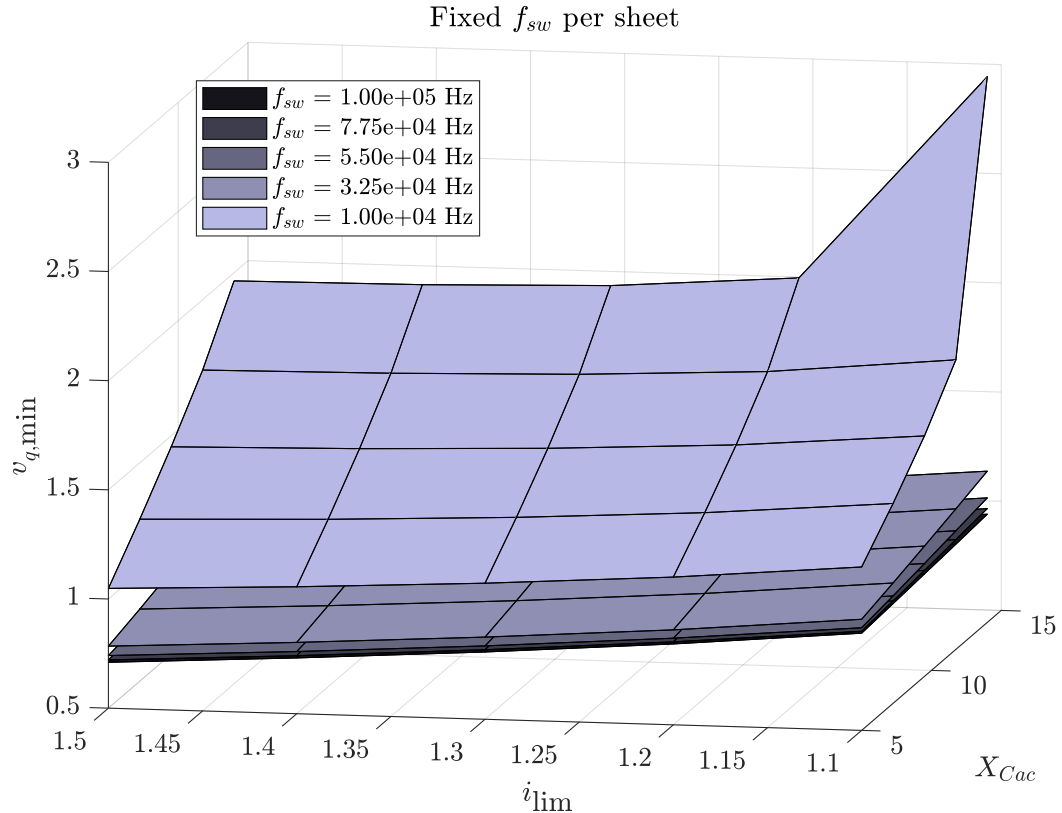


Fig. 4.2.: A projection of the parameter-space boundary onto i_{lim} , X_{Cac} , $v_{q,min}$ space

change in real-power load. Lastly, it can be seen that as switching frequency increases, each “sheet” tends to get closer together, implying that switching frequency, and by extension closed-loop controller bandwidth, is the dominant parameter associated with Large-Displacement Stability.

Alternate projections of this boundary can be seen in Figures 4.3 and 4.4. From these figures, it can be observed that the “sheets” are grouped at approximately uniform distances from each other at higher switching frequencies in both cases, indicating that the ability to maintain stability depends directly on each of these values. Since the separation between the sheets is greater in Figure 4.3 than in Figure 4.4, it can be claimed that as long as switching frequency is sufficiently high, the current command limit has a greater impact on stability than capacitance.

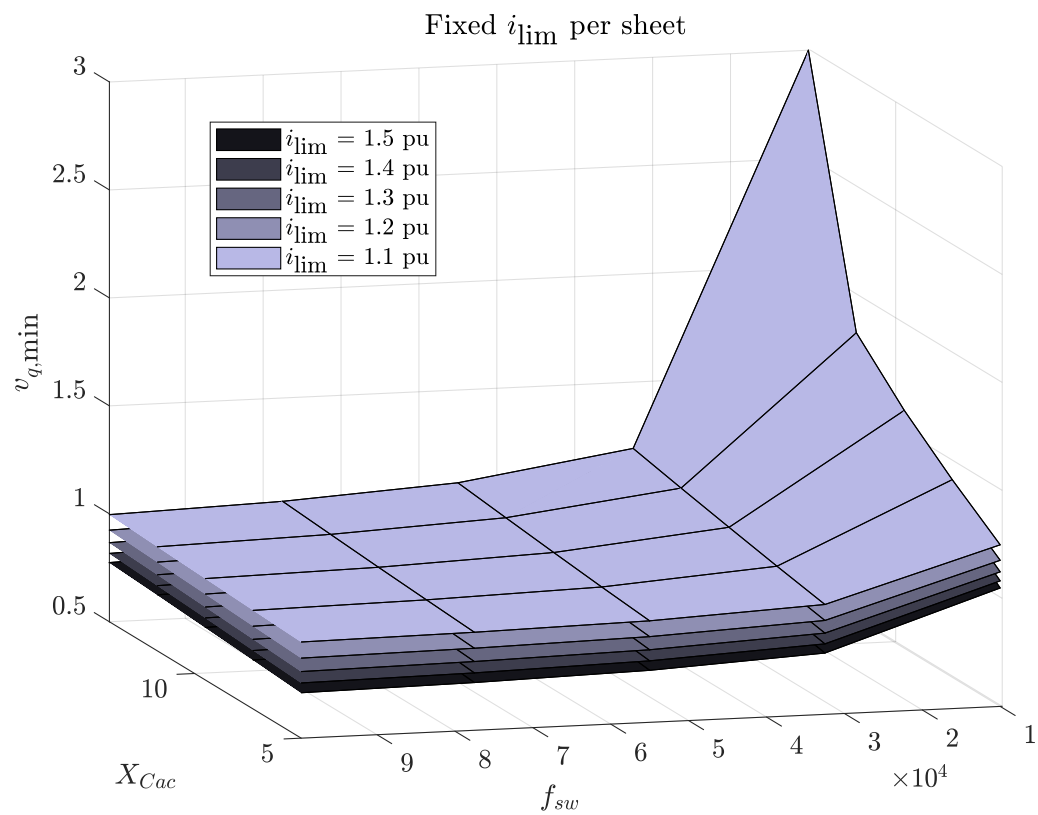


Fig. 4.3.: A projection of the parameter-space boundary onto f_{sw} , X_{Cac} , $v_{q,\text{min}}$ space

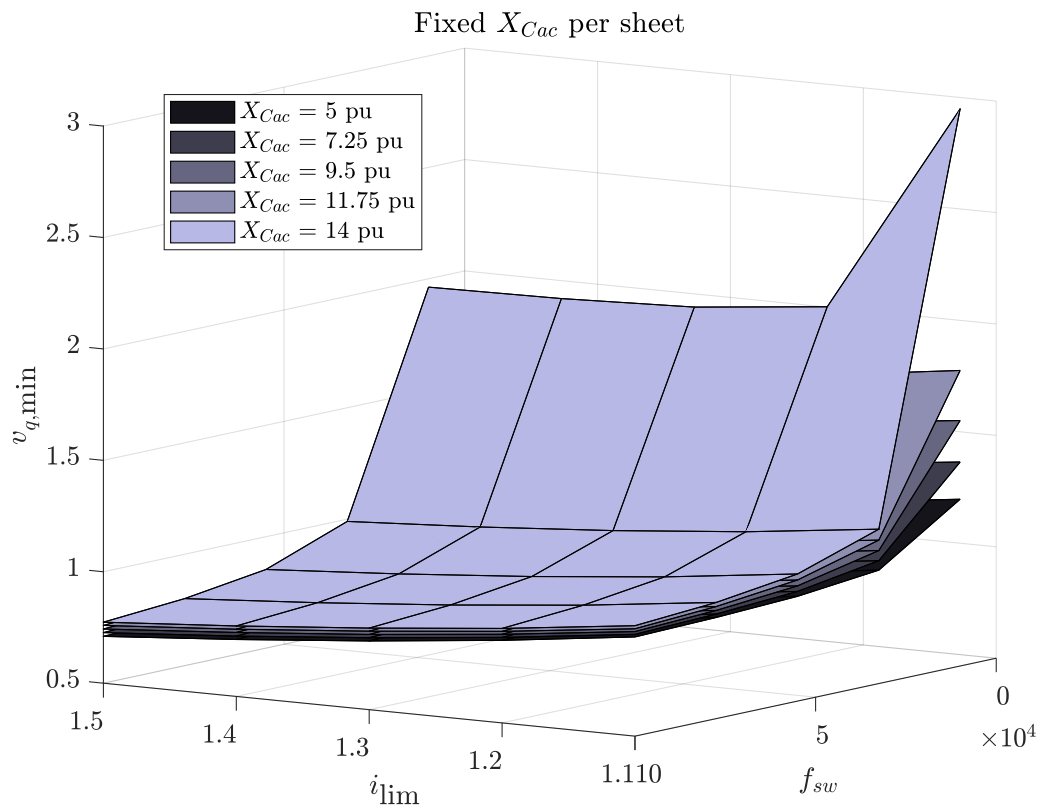


Fig. 4.4.: A projection of the parameter-space boundary onto f_{sw} , i_{lim} , $v_{q,min}$ space

These figures confirm what might intuitively be understood by an engineer designing a control system for a 3-phase current source: larger switching frequencies enable faster closed-loop poles, larger capacitors lead to less required initial voltage to maintain stability for larger transients, and larger transient overload limits lead to more stable systems. What is gained by showing them is that capacitance is, out of the three parameters investigated, the least important when it comes to designing for stability past a certain threshold of f_{sw} , and that switching frequency dominates the system performance.

4.3 Estimating Regions of Asymptotic Stability

In practicable power systems, maintaining stability for step changes in load up to 1 pu may not be required. Power systems tend to be oversized for safety reasons, and therefore within the following work, it is assumed that the load is bounded in magnitude by 0.5 pu, and in angle by $-\pi/2$ to $\pi/2$ in the PQ -plane. It is assumed that the system being analyzed is designed only to source power, not to sink power, which increases the size of the RAS and decreases the size of the RSS. To generate the results in this chapter, a switching frequency of 50 kHz was applied, along with a capacitive reactance of 5 pu and a transient overload capacity of 1.5 pu.

The RAS is established numerically by fixing a subset of the states and performing a linear search along the remaining states for the minimum value required of those states to maintain stability. More detail on this algorithm can be found in Appendix A. The RAS was established for 5 different loads within the unit circle in the PQ plane. Due to the dimensionality of the system, the RAS can be difficult to visualize and interpret.

To view the four-dimensional RAS's discussed in this chapter, it is necessary to display projections of the RAS's, since displaying the data in all four dimensions is

impossible. Therefore, it is necessary to define what a three-dimensional projection of a four-dimensional region R is. Such a projection is defined as

$$R_{(i,j,k)} = \{(x_{(i)}, x_{(j)}, x_{(k)}) \forall x \in R\} \quad (4.22)$$

and a three-dimensional slice of a four-dimensional region R is defined as

$$R_{(i,j,k)} \Big|_{x_{(l)} \text{ specified}} = \{(x_{(i)}, x_{(j)}, x_{(k)}) \forall x \in R : x_{(l)} \text{ specified for } l \neq i, j, k\} \quad (4.23)$$

Similarly, a two-dimensional projection of a four-dimensional region R is defined as

$$R_{(i,j)} = \{(x_{(i)}, x_{(j)}) \forall x \in R\} \quad (4.24)$$

A projection of the RAS for the ac system corresponding to a real power load of 0.5 pu and a reactive load of 0 is shown in Figure 4.5. Within the figure, the areas within each arch have been filled in to improve visualization. The “wall” of the resulting tunnel represents a projection the boundary of the RAS, with the projection of the RAS itself being the space above the boundary along the v_q axis. It is important to note that points entirely above the projected boundary are always within the RAS regardless of the remaining state that is not displayed. Similarly, points within the tunnel are always outside of the RAS regardless of the remaining state. Points within the wall may or may not be within the RAS depending on the value of the last state. It is possible for projections of state trajectories to appear to enter the walls of the tunnel, which might appear to contradict a key property of an RAS, which is that state trajectories starting within the RAS always remain within the RAS. Even if a projection of a trajectory enters the wall representing the projection of the RAS boundary, it remains impossible for the trajectory to leave the RAS, and so the state that was not displayed in the projection is known to have a value such that a slice of the RAS boundary at that fixed value would remain below the trajectory.

After each individual arch is established, the projection of the RAS boundary can be established by finding the boundary of the set of arches to form a “tunnel” with thick walls. The projection of the RAS itself if the hyper-volume above these walls

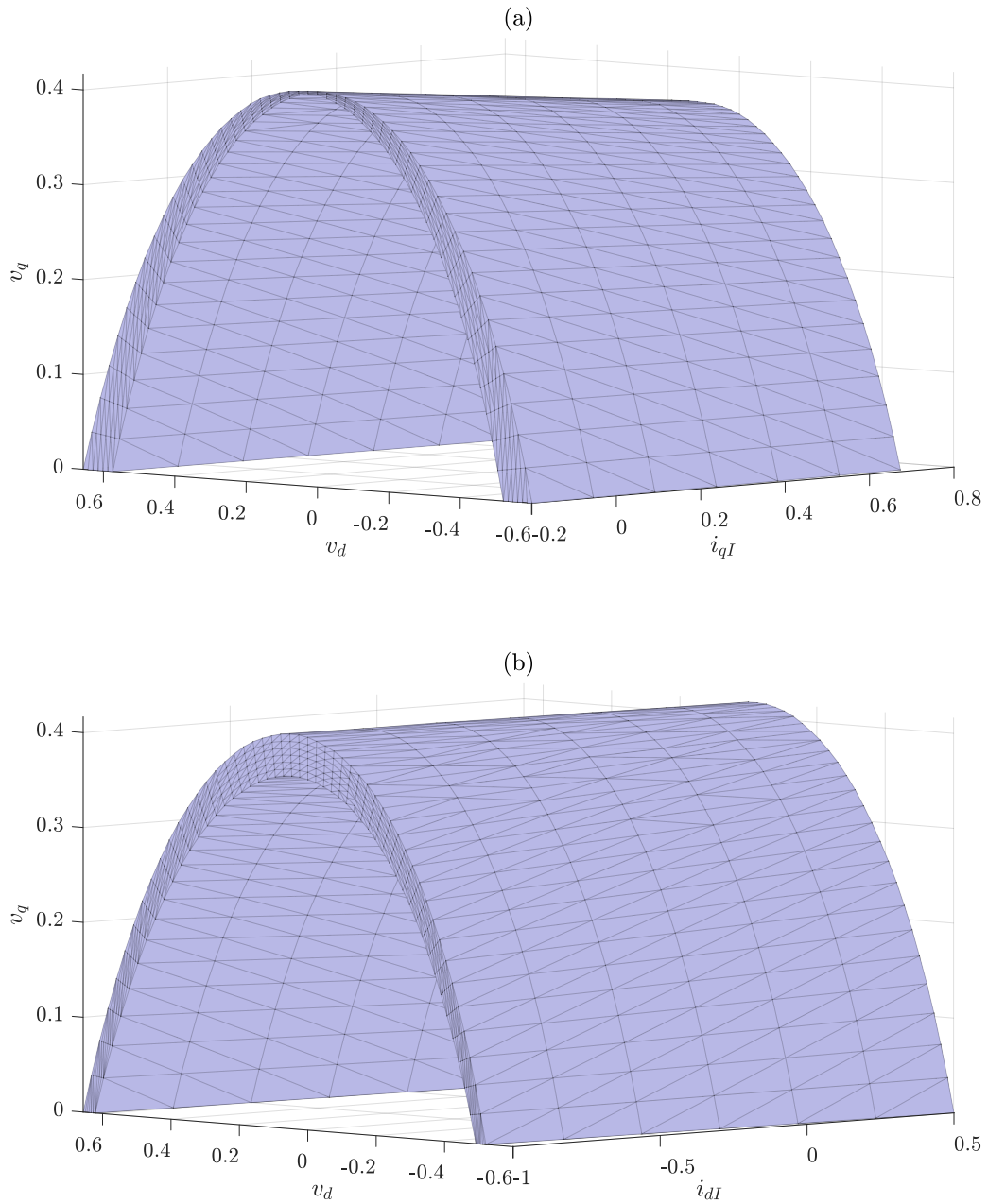


Fig. 4.5.: Projections of the RAS for the ac system with a load of $P = 0.5$ pu, $Q = 0$ pu, projected into (a) v_q, v_d, i_{qI} space and (b) v_q, v_d, i_{dI} space. The region above the tunnel is guaranteed to be inside the RAS, while the region inside the tunnel is guaranteed to be outside the RAS.

along the v_q axis. To consider a 3-dimensional slice of the space, one arch can be fixed from each collection of arches making up the tunnel wall, keeping the individual arch corresponding to the value of interest. The rough shape of the tunnel is preserved, but it can be seen that the walls become infinitely thin, and move side-to-side (in the case of the projection into v_q, v_d, i_{qI} space) or up-and-down (in the case of the projection into v_q, v_d, i_{dI} space) as the value of the fixed state is fixed to other values.

This process was repeated for 5 loads around the unit circle. These projections can be seen in Figures 4.5 through 4.9. It can be seen that as the load moves closer and close to the Q axis, the minimum necessary voltage magnitude decreases along both voltage axes. This implies that it is most difficult to maintain stability for a step change in purely real constant apparent power load.

It can be seen in Figure 4.10 that there is an intersection of the surface corresponding to the RAS associated with a load of $P = 0.5$ pu, $Q = 0$ and the surfaces corresponding to $P = \sqrt{2}/4$ pu, $Q = \pm\sqrt{2}/4$ pu. The surfaces are close to one another in both figures, and based on experience in exercising the simulation used to generate these surfaces, it is extremely unlikely (impossible, as will be demonstrated in the next section) that the state trajectory ever lead to that part of the state-space. Therefore, for the sake of simplicity, the RLDS can be approximated by the RAS corresponding to an input power of $P = 0.5$ pu, $Q = 0$, as the volume above that surface is common to all RAS's.

4.4 RSS Estimation

To estimate the boundary of the RSS, a brute-force recursive search can be implemented, similar to the algorithm implemented in Chapter 3 for the 2- and 3-dimensional systems studied therein. Similarly to those cases, a wide array of inputs are simulated along each trajectory resulting from each input. The state-space is discretized into a set of hyperrectangular domains, each initially marked with a logical 0. As each simulated trajectory traverses the state-space, each domain it traverses is

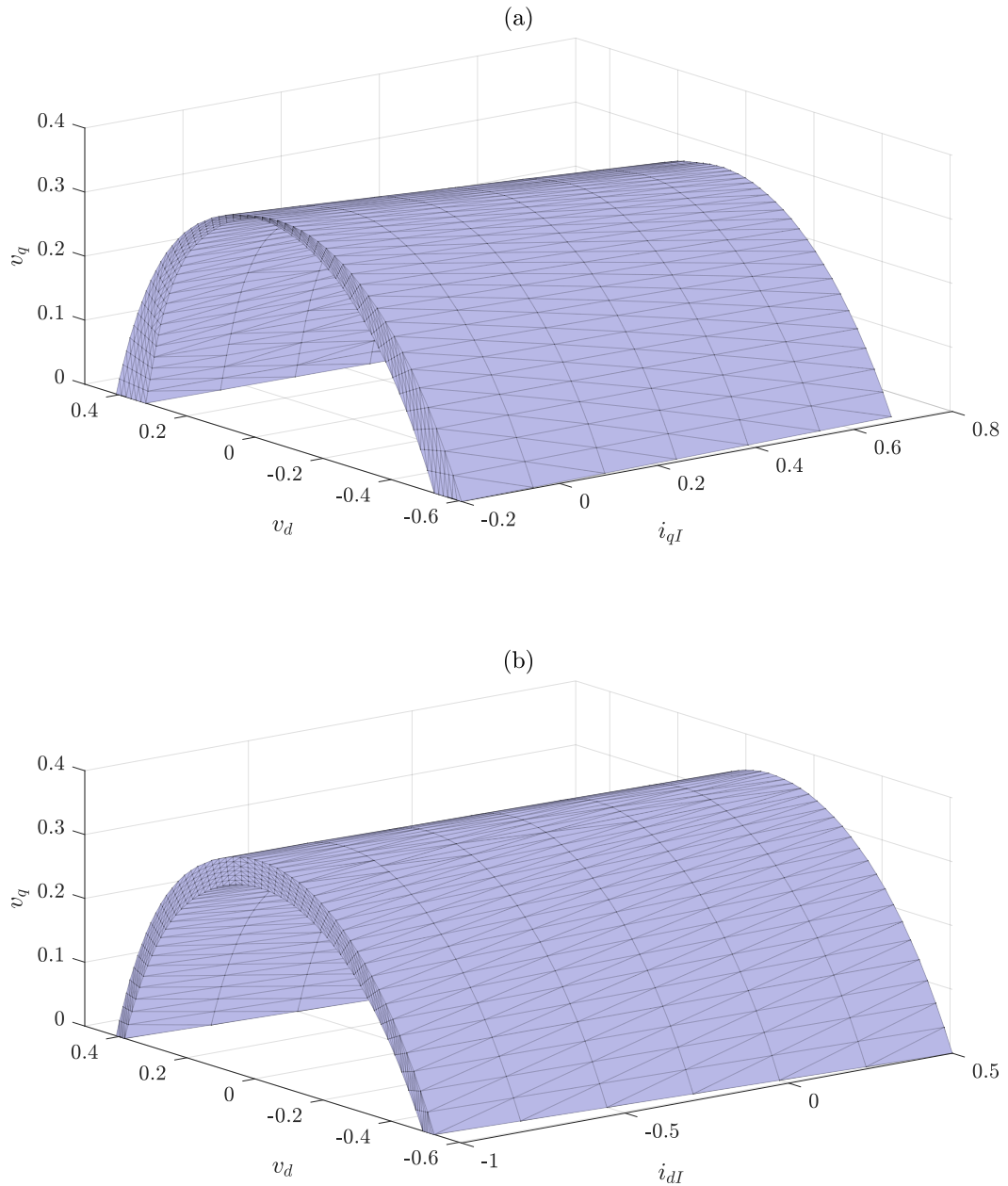


Fig. 4.6.: Projections of the RAS for the ac system with a load of $P = \sqrt{2}/4$ pu, $Q = \sqrt{2}/4$ pu, projected into (a) v_q, v_d, i_{qI} space and (b) v_q, v_d, i_{dI} space. The region above the tunnel is guaranteed to be inside the RAS, while the region inside the tunnel is guaranteed to be outside the RAS.

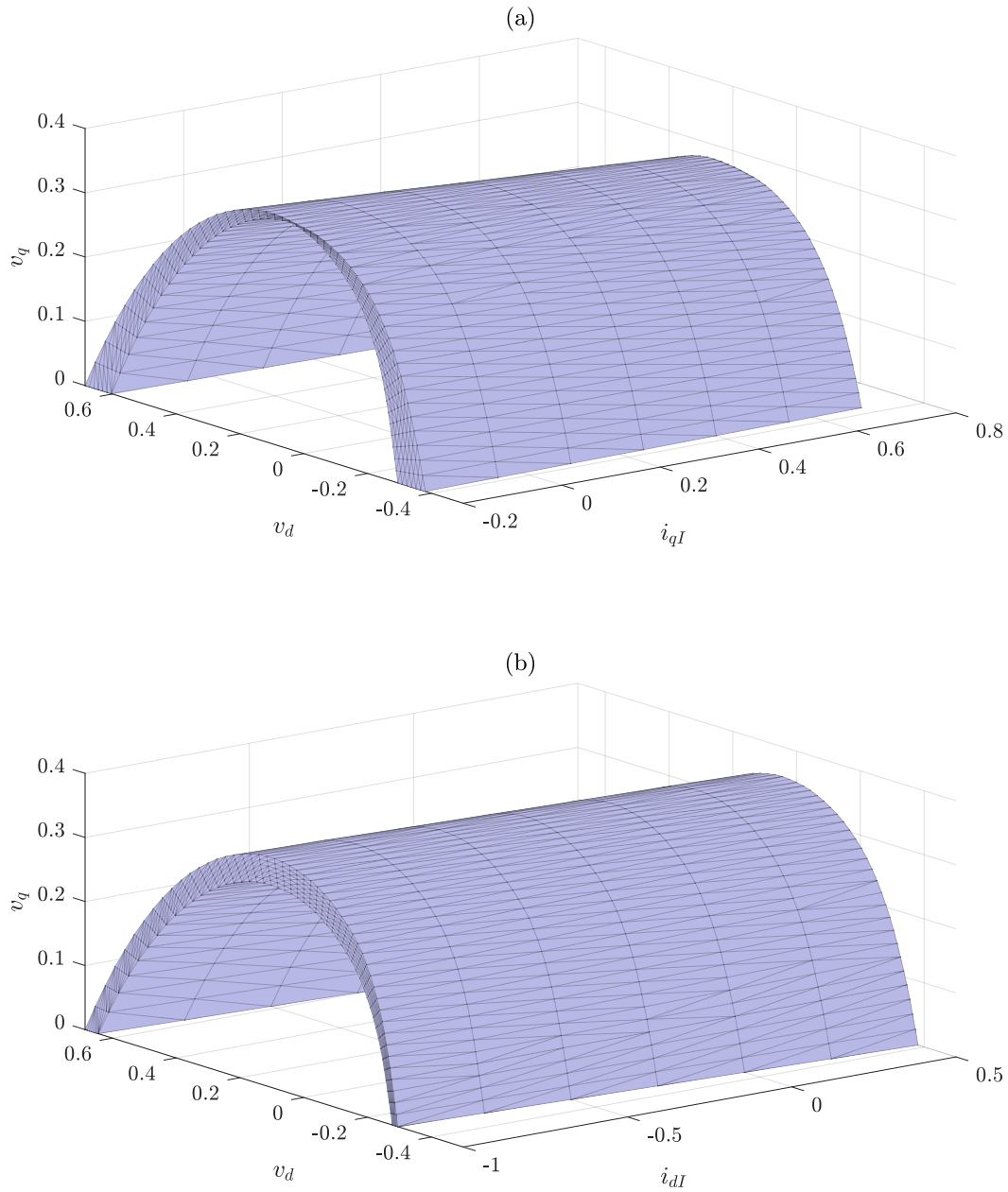


Fig. 4.7.: Projections of the RAS for the ac system with a load of $P = \sqrt{2}/4$ pu, $Q = -\sqrt{2}/4$ pu, projected into (a) v_q, v_d, i_{qI} space and (b) v_q, v_d, i_{dI} space. The region above the tunnel is guaranteed to be inside the RAS, while the region inside the tunnel is guaranteed to be outside the RAS.

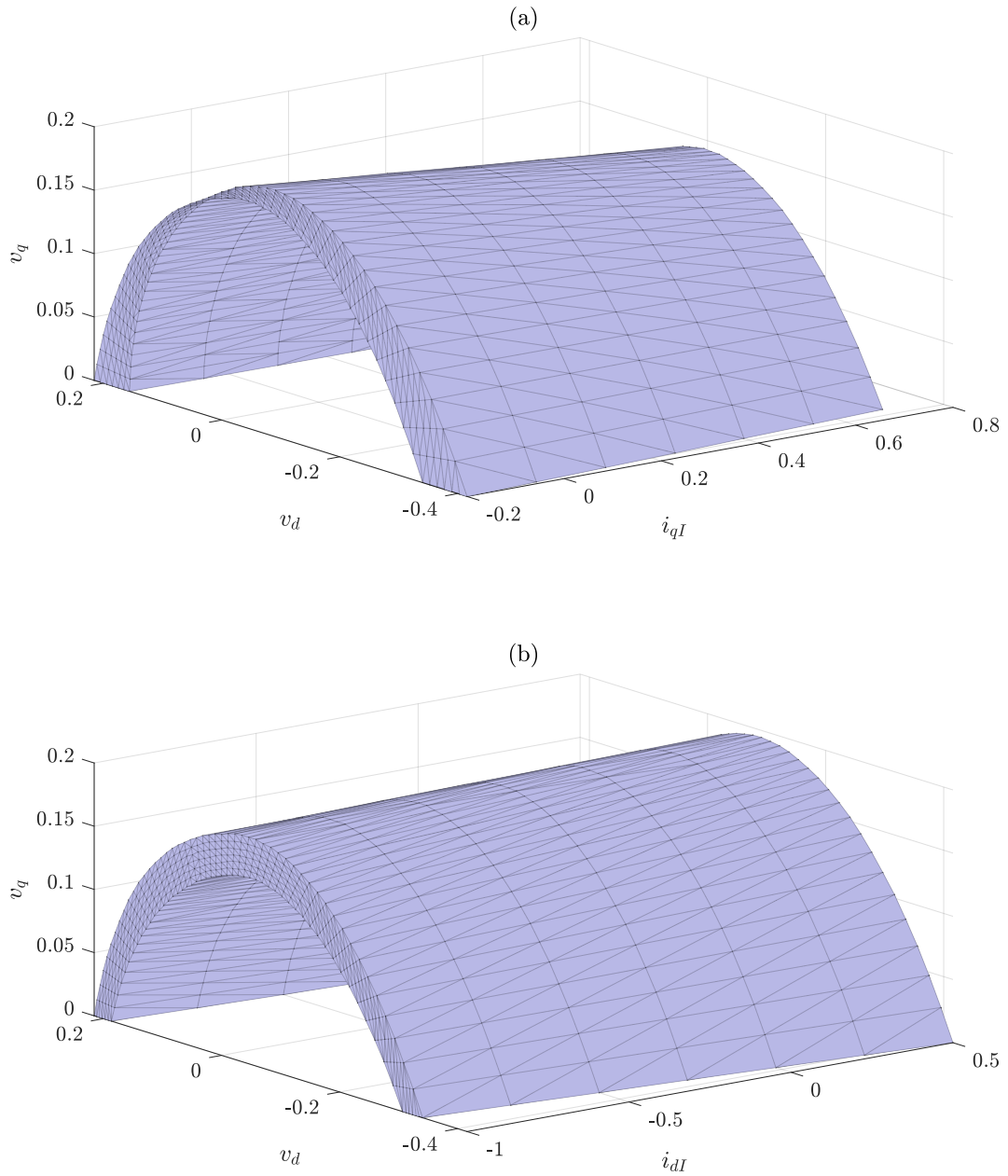


Fig. 4.8.: Projections of the RAS for the ac system with a load of $P = 0$ pu, $Q = 0.5$ pu, projected into (a) v_q, v_d, i_{qI} space and (b) v_q, v_d, i_{dI} space. The region above the tunnel is guaranteed to be inside the RAS, while the region inside the tunnel is guaranteed to be outside the RAS.

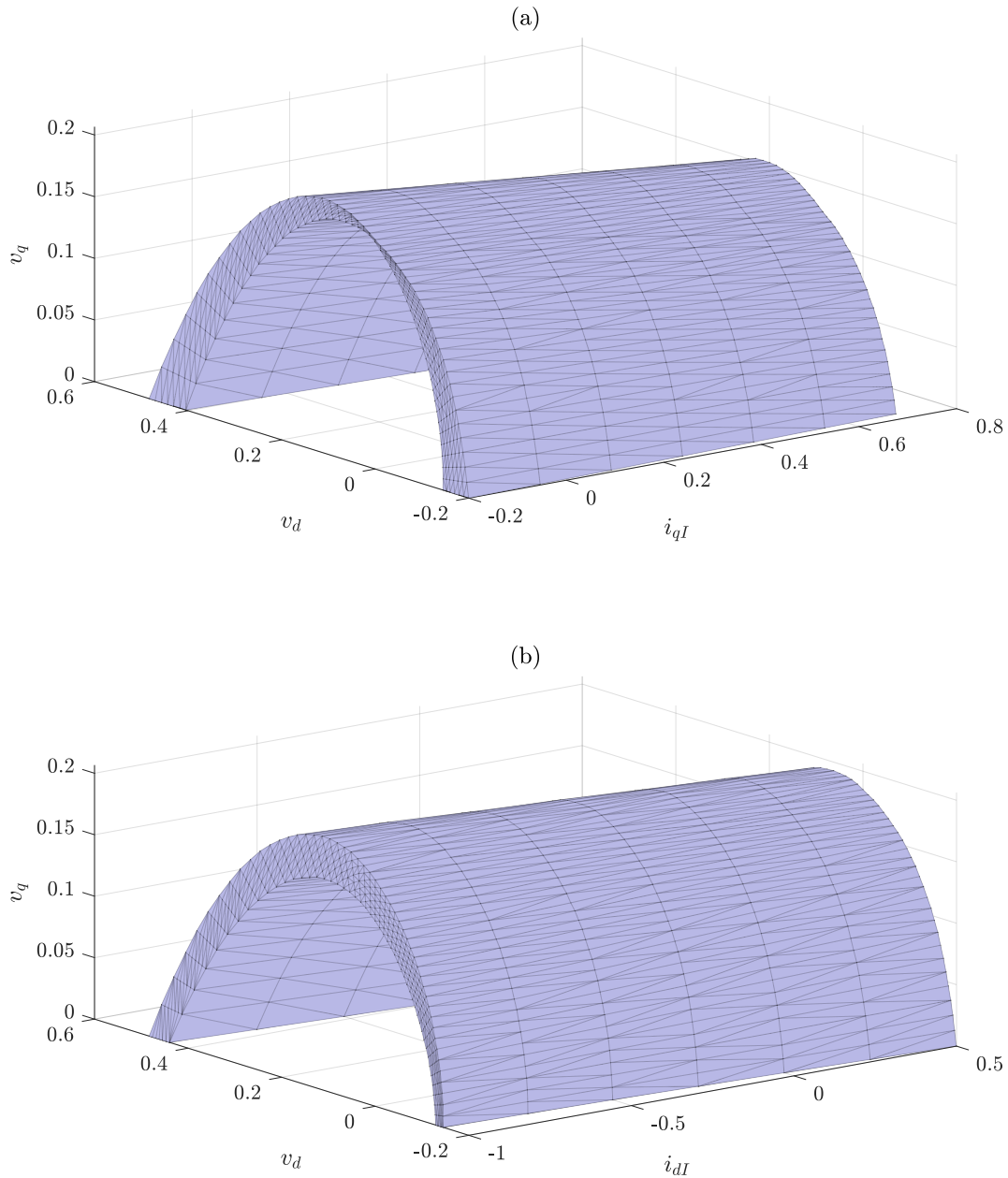


Fig. 4.9.: Projections of the RAS for the ac system with a load of $P = 0$ pu, $Q = -0.5$ pu, projected into (a) v_q, v_d, i_{qI} space and (b) v_q, v_d, i_{dI} space. The region above the tunnel is guaranteed to be inside the RAS, while the region inside the tunnel is guaranteed to be outside the RAS.

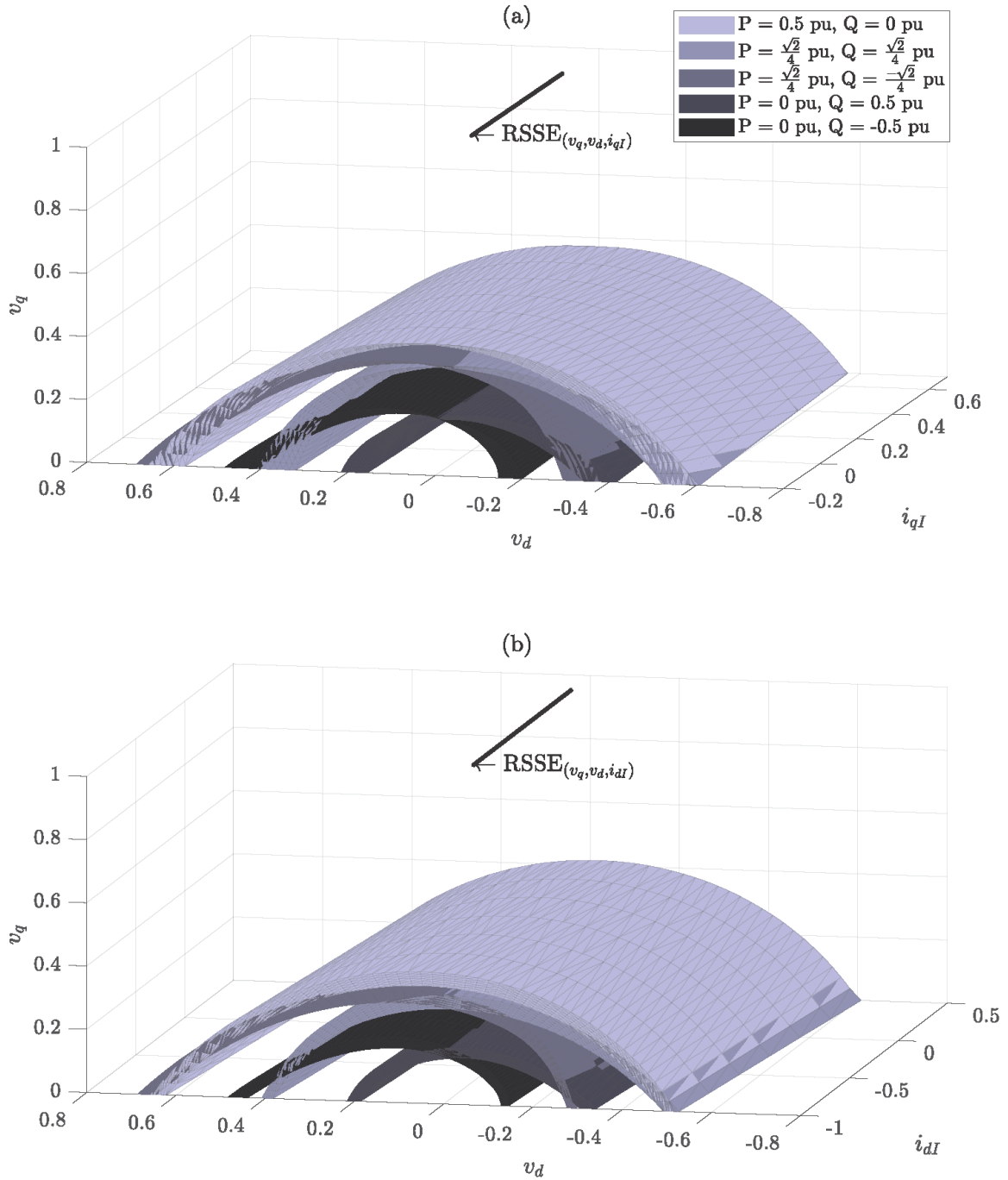


Fig. 4.10.: A projection of the intersections of conservative over-approximations of the RAS's for 5 loads around the PQ -plane into (a) v_q, v_d, i_{qI} space and (b) v_q, v_d, i_{dI} space.

marked a logical 1. When the trajectory arrives at the equilibrium point corresponding to the input which drives it, the search algorithm terminates. The key difference between the searches performed in Chapter 3 and the search performed here is that there are two possible inputs bounded by an apparent power of 0.5 pu and an angle between $-\pi/2$ and $\pi/2$ in the PQ plane with respect to the positive P axis. This process is summarized in Algorithms 3 and 4.

Algorithm 3 Main function to search for the reachable state-space

reachable_set = false($N_{i_q}, N_{i_d}, N_{v_q}, N_{v_d}$)

$x \leftarrow x_{eq}$

search_statespace(x, u_1)

search_statespace(x, u_2)

search_statespace(x, u_3)

search_statespace(x, u_4)

search_statespace(x, u_5)

search_statespace(x, u_6)

It is important to test a wide array of inputs over the two-dimensional input space. It is noted that the approximation of other loads over longer time horizons as discussed in Chapter 3 still applies, though approximating loads between two selected inputs along the outer edge of the input space suffers a minor loss in accuracy. For example, if it is desired to approximate a load with a real component of $P = 0.9239$ pu and an imaginary component of $Q = 0.3827$ (corresponding to a load of magnitude 1 pu with an angle of $\pi/8$ radians with respect to the positive P axis), an average could be taken of a load of $P = 1$ pu, $Q = 0$ pu and a load of $P = 0.7071$ pu and $Q = 0.7071$ pu (each corresponding to a load with magnitude 1, the first with an angle of 0 with respect to the positive P axis, the second with an angle of $\pi/4$). However, it can be seen that these two loads average to $P = 0.8536$ pu and $Q = 0.3536$ pu, which corresponds to a load of magnitude 0.9239 with an angle of $\pi/8$ with respect to the positive P axis, not a magnitude of 1. Due to the small difference in magnitude,

Algorithm 4 search_statespace(x, u)

```
update  $x_{eq}$ 
while  $\|x - x_e\| > \epsilon$  do
     $px \leftarrow \text{state\_derivative}(x, u)$ 
     $x \leftarrow x + h px$ 
     $i, j, k, l \leftarrow \text{quantize}(x)$ 
    if reachable_set( $i, j, k, l$ ) = false then
        reachable_set( $i, j, k, l$ ) = true
        search_statespace( $x_k, u_1$ )
        search_statespace( $x_k, u_2$ )
        search_statespace( $x_k, u_3$ )
        search_statespace( $x_k, u_4$ )
        search_statespace( $x_k, u_5$ )
        search_statespace( $x_k, u_6$ )
    end if
end while
```

this difference is noted, however for the sake of approximation, the loss in accuracy is accepted.

The increased number of inputs exacerbates the memory usage of the algorithm, thus limiting the resolution of the final answer. This limited resolution means that there is a degree of uncertainty in the final result. After the routine terminates, the each domain index is mapped to the center of its corresponding hyperrectangle in the state-space, regardless of the path the trajectory took through that domain. The true boundary of the RSS, should it exist, will be within one domain-width of the final result obtained by the recursive search. In order to minimize uncertainty, a large number of domains and a small time-step is required. Taking this to extremes, however, will put a great strain on the program being used to execute this search, and so a balance is required. The maximum error produced by this method can be expressed:

$$\text{error} = \frac{1}{2} \sqrt{x_{1,\text{dom}}^2 + x_{2,\text{dom}}^2 + x_{3,\text{dom}}^2 + x_{4,\text{dom}}^2} \quad (4.25)$$

where $x_{i,\text{dom}}$ is the width of a domain along the i_{th} axis.

For the system designed in this chapter, this search was executed with parameters shown in Table 4.2, in which N_x refers to the number of domains along the x axis, and f_{\min} and f_{\max} refer to the upper and lower search bounds along the respective axes. With these search boundaries and domains, the maximum error between the estimated RSS and the true RSS boundary is 0.0116 pu. The RSS was estimated with six loads, including $P = 0.5$ pu, $Q = 0$ pu; $P = \frac{\sqrt{2}}{4}$ pu, $Q = \pm \frac{\sqrt{2}}{4}$ pu; $P = 0$ pu, $Q = \pm 0.5$ pu; and $P = 0$ pu, $Q = 0$ pu.

Projections of the estimated reachable state-space and projections of the RLDS can be seen in Figure 4.11. In Figure 4.11(a), it can be seen that there is a large degree of separation between the two boundaries, and that these boundaries take all possible values of i_{dI} into account, indicating that the system is highly stable. The same is true for Figure 4.11(b), which takes into account all possible values of i_{qI} .

Within each projection, the projected boundaries appear to be closer or further apart from one another at different values of state. The trajectory is always guar-

Table 4.2.: RSS search parameters for the 50 kHz system

Parameter	Value
N_{i_q}	135
N_{i_d}	100
N_{v_q}	75
N_{v_d}	75
$i_{qI,\max}$ (pu)	0.7
$i_{qI,\min}$ (pu)	-0.2
$i_{dI,\max}$ (pu)	0.5
$i_{dI,\min}$ (pu)	-0.9
$v_{q,\max}$ (pu)	1.2
$v_{q,\min}$ (pu)	0.8
$v_{d,\max}$ (pu)	0.3
$v_{d,\min}$ (pu)	-0.3

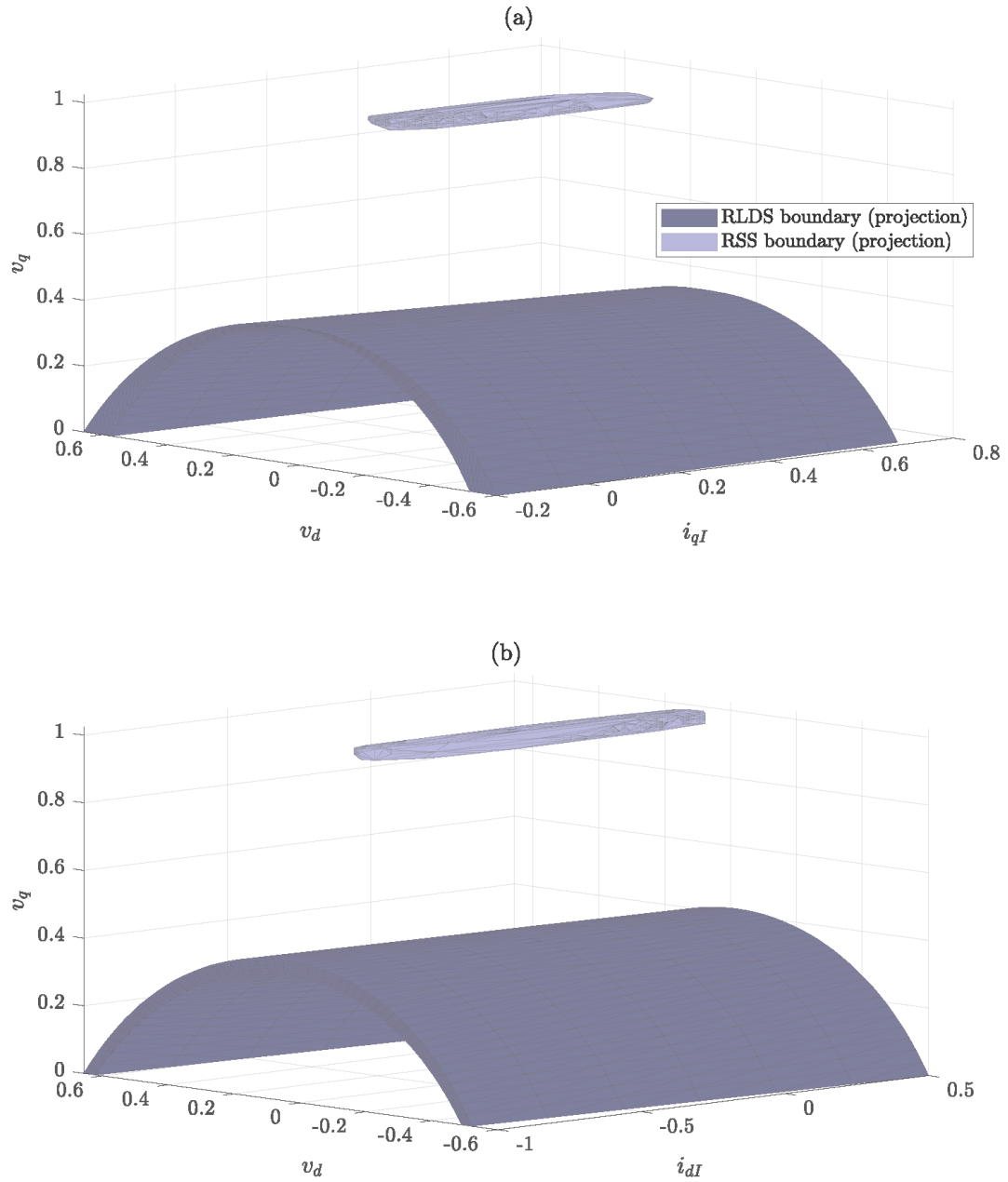


Fig. 4.11.: The RSS and RLDS projected into (a) i_{qI} , v_d , v_q space, and (b) i_{dI} , v_d , v_q space with inputs bounded by 0.5 pu.

anteed to be within the lighter region in each projection, regardless of the value of the state that has been “projected away”. As previously discussed, the volume above the darker “tunnel” is the portion of the projection of the RLDS where the state is guaranteed to be within the RLDS regardless of the value of the fourth state. The volume enclosed by the darker region corresponds to the portion of the projection of the RLDS in which the value of the fourth state determines whether or not the state is within the RLDS or outside of the RLDS. Therefore, if a similar study were performed on a system and results were obtained such that the projection of the boundary of the RSS appears to intersect with the projection of the boundary of the RLDS, the results need not be discarded. As was noted previously, the RSS is bounded if and only if it is wholly contained by the RLDS. Therefore if the situation arises in which the projections of the boundary intersect, yet the RSS boundary was still found, the system is still LDS.

To calculate the Large-Displacement Stability Margin (LDSM), a brute-force search was implemented to take the norm of the difference of each point on the boundary of the RSS and each point on the boundary of the RLDS, keeping track of the smallest result at each combination. This process was not completed using projections of data, but rather the 4-dimensional data generated by each respective search algorithm. Using this brute-force search, the LDSM was found to be 0.5762. Assuming conservatively that the true boundary of the RSS is a full 0.0116 pu away from the estimated boundary shown in Figure 4.12, the LDSM for the system shown in Figure 4.1 is 0.5646 pu.

As previously stated, this system was designed for loads bounded in magnitude by 0.5 pu and in angle by $-\pi/2$ to $\pi/2$ in the PQ plane. If, however, it is desired to have a system for which it is possible to apply 1 pu step changes, the same algorithms utilized in this chapter can be utilized to show that such a system is realizable. In the results shown earlier in this chapter, a switching frequency of 50 kHz was used, but in order to achieve a LDS system for this larger input set, it is necessary to increase f_{sw} to 100 kHz. X_{Cac} and i_{lim} were both kept the same.

Table 4.3.: RSS search parameters for the 100 kHz system

Parameter	Value
N_{i_q}	80
N_{i_d}	40
N_{v_q}	80
N_{v_d}	80
$i_{qI,\max}$ (pu)	1.5
$i_{qI,\min}$ (pu)	-0.5
$i_{dI,\max}$ (pu)	1
$i_{dI,\min}$ (pu)	-1.5
$v_{q,\max}$ (pu)	1.2
$v_{q,\min}$ (pu)	0.8
$v_{d,\max}$ (pu)	0.1
$v_{d,\min}$ (pu)	-0.1

Figure 4.12 shows the projections of the RSS and RLDS of the 4d system with a switching frequency of 100 kHz. It can be seen that there is still a large degree of separation between the two boundaries when projected into 3d space. Once again, a brute force search was implemented to establish the LDSM. For the RSS search parameters in Table 4.3, the discretization error is 0.0203, and the norm of the maximum distance between the boundaries was found to be 0.2755 pu, resulting in an LDSM of 0.2552 pu.

4.5 Small-Displacement Criterion

A common criticism of small-displacement stability criteria is that several lead to overly conservative designs. In this research, a new perspective on stability is taken

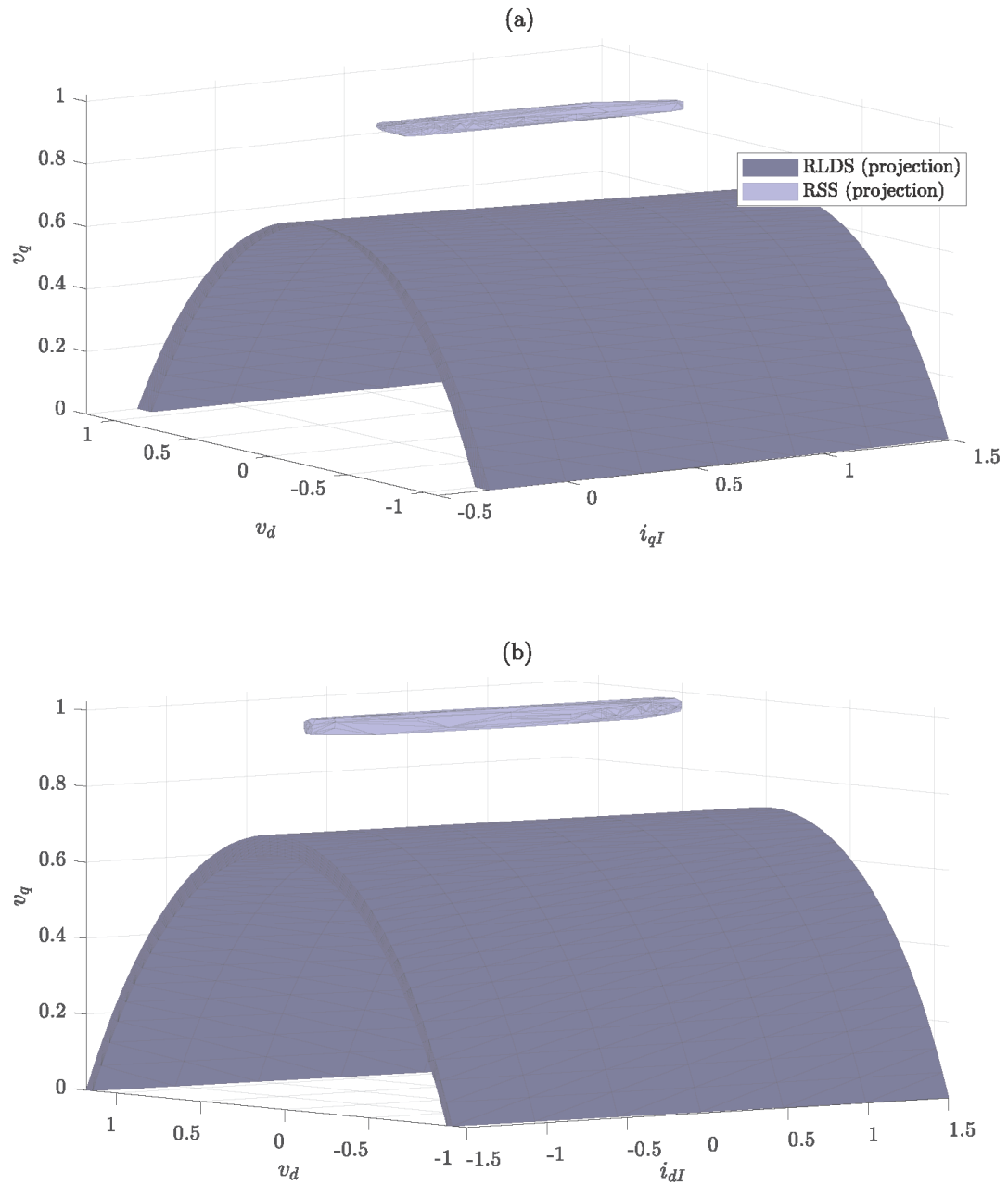


Fig. 4.12.: The RSS and RLDS projected into (a) i_{qI} , v_d , v_q space, and (b) i_{dI} , v_d , v_q space with inputs bounded by 1 pu.

which does not rely on linearity or linear approximations of systems. In light of this new framework, it is of interest to analyze the stability of the system from traditional small-displacement perspectives to determine whether or not the criteria are overly conservative.

As described in Chapter 1, the ac system studied in this chapter can be represented as a Thevenin equivalent source in the synchronous reference frame with equivalent impedance matrix $\mathbf{Z}_S \in \mathcal{C}^{2 \times 2}$ feeding a Norton equivalent load with equivalent admittance matrix $\mathbf{Y}_L \in \mathcal{C}^{2 \times 2}$. If the product of the largest singular values of these matrices is less than 1 for all frequencies, then the system is said to be stable.

To represent this system in that form, current command limits are neglected, and the current source dynamics found in (4.15) and capacitor dynamics found in (4.20) are put into state-space form, substituting the control law (4.17) into (4.15). The load currents are not expressed as functions of power, but left as general inputs. The linear state-space equations describing the internal dynamics are

$$\begin{aligned}
 p \begin{bmatrix} v_q \\ v_d \\ i_{qI} \\ i_{dI} \end{bmatrix} &= \begin{bmatrix} 0 & -\omega_e & \omega_b X_{Cac} & 0 \\ \omega_e & 0 & 0 & \omega_b X_{Cac} \\ -\frac{k_{pv}}{\tau} & \frac{1}{\tau X_{Cac}} & -\frac{1}{\tau} & 0 \\ -\frac{1}{\tau X_{Cac}} & -\frac{k_{pv}}{\tau} & 0 & -\frac{1}{\tau} \end{bmatrix} \begin{bmatrix} v_q \\ v_d \\ i_{qI} \\ i_{dI} \end{bmatrix} \\
 &+ \begin{bmatrix} 0 & 0 \\ 0 & 0 \\ \frac{k_{pv}}{\tau} & 0 \\ 0 & \frac{k_{pv}}{\tau} \end{bmatrix} \begin{bmatrix} v_q^* \\ v_d^* \end{bmatrix} + \begin{bmatrix} -\omega_b X_{Cac} & 0 \\ 0 & -\omega_b X_{Cac} \\ \frac{1}{\tau} & 0 \\ 0 & \frac{1}{\tau} \end{bmatrix} \begin{bmatrix} i_{qL} \\ i_{dL} \end{bmatrix}
 \end{aligned} \tag{4.26}$$

where, the vector containing the qd voltages and currents is the state vector \mathbf{x} , the matrix pre-multiplying the state vector is denoted \mathbf{A} , the matrix pre-multiplying the q - and d -axis voltage commands is denoted \mathbf{B}_1 , and the matrix pre-multiplying the

load currents is denoted \mathbf{B}_2 . The outputs of the source are the q - and d -axis voltages. The outputs are expressed

$$\mathbf{y} = \begin{bmatrix} 1 & 0 & 0 & 0 \\ 0 & 1 & 0 & 0 \end{bmatrix} \begin{bmatrix} v_q \\ v_d \\ i_{qI} \\ i_{dI} \end{bmatrix} \quad (4.27)$$

where the matrix pre-multiplying \mathbf{x} is denoted \mathbf{C} . To establish the Thevenin equivalent representation of the source, the Heaviside operator p is replaced with $j\omega$, and (4.26) is solved for \mathbf{x} . The results are substituted into (4.27). Symbolically, the final result is expressed

$$\begin{bmatrix} v_q \\ v_d \end{bmatrix} = \mathbf{C} (j\omega \mathbf{I}_4 - \mathbf{A})^{-1} \left(\mathbf{B}_1 \begin{bmatrix} v_q^* \\ v_d^* \end{bmatrix} + \mathbf{B}_2 \begin{bmatrix} i_{qL} \\ i_{dL} \end{bmatrix} \right) \quad (4.28)$$

where \mathbf{I}_4 is the identity matrix of size 4. The impedance matrix as described by Chapter 1 is

$$\mathbf{Z}_S = \mathbf{C} (j\omega \mathbf{I}_4 - \mathbf{A})^{-1} \mathbf{B}_2 \quad (4.29)$$

and the \mathbf{H} matrix is

$$\mathbf{H} = \mathbf{C} (j\omega \mathbf{I}_4 - \mathbf{A})^{-1} \mathbf{B}_1 \quad (4.30)$$

To establish the load admittance, (4.21) can be linearized about a point of interest. For this research, (4.21) was linearized about the equilibrium point, and so \mathbf{Y}_L is

$$\mathbf{Y}_L = \begin{bmatrix} -P & -Q \\ Q & -P \end{bmatrix} \quad (4.31)$$

To evaluate the so-called Belkhat Criteria as described in Chapter 1, the parameters used to generate the RSS and RLDS of the 50 kHz system were used to generate \mathbf{Z}_S and \mathbf{Y}_L . Then, the singular values of these matrices were found at a broad range of frequencies and a broad range of loads, and their product was taken. The results can be seen in Figure 4.13. Only two loads were tested, since the singular values of the admittance matrix are maximized when the load is entirely real or entirely reactive, and minimized when the load is evenly split between both axes.

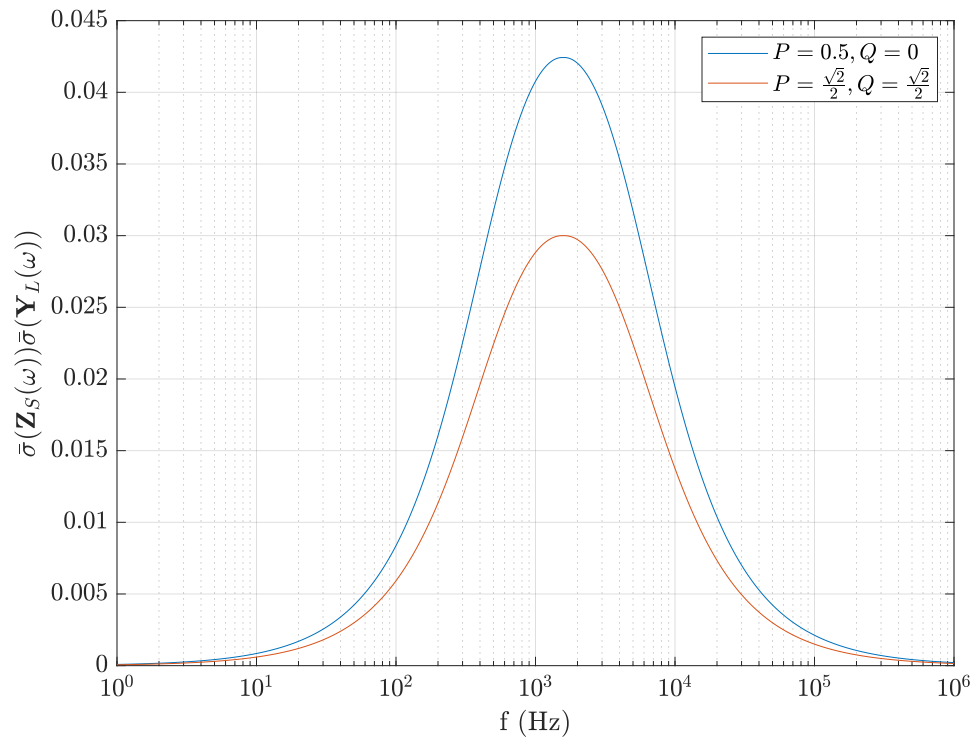


Fig. 4.13.: The Belkhayat contours of the LDS system over a broad range of frequencies.

It can be seen that the largest that the product of the two singular values gets is less than 0.045. Given that the product is required to be less than 1 for all frequencies, the Belkhat criteria is easily satisfied. With the results produced within the framework set forth in this thesis, it is apparent that any concerns over of the conservatism of this small-displacement criterion are not relevant.

5. DETAILED SYSTEM STUDY

Due to their computational complexity, detailed system studies cannot be used to generate regions of interest, such as the RLDS or RSS, since the methods discussed in this research rely on performing hundreds, if not thousands of simulations. Some accuracy is lost in the conversion of detailed models which incorporate switching effects to average-value models which do not. Therefore, once the regions of interest have been established using average-value models, it is important to validate average-value model results against more detailed system studies. In this chapter, a detailed model of an inverter is set forth to emulate the three-phase current source described in Chapter 4, and studies are conducted to illustrate the large-displacement response.

5.1 Detailed Inverter Model

As noted in Chapter 4, from a stability perspective, there is no difference between a current-regulated voltage source converter and the current source behavioral model studied in Chapter 4, as long as the base ac voltage is sufficiently lower than the base dc voltage. For this study, a current-regulated voltage source converter was developed with a control law of the same form as (4.14). A circuit/block diagram of the source model can be seen in Figure 5.1. The various components depicted in Figure 5.1 are described in the following paragraphs.

The commanded inverter voltages \mathbf{v}_{qdl}^* are fed into a sine-triangle modulator with third harmonic injection to produce voltages at the output of the converter [33]. In this modulation strategy, switching signals are generated by comparing sinusoidal duty cycles d_a , d_b , and d_c to a triangle wave oscillating at f_{sw} . When the duty cycle

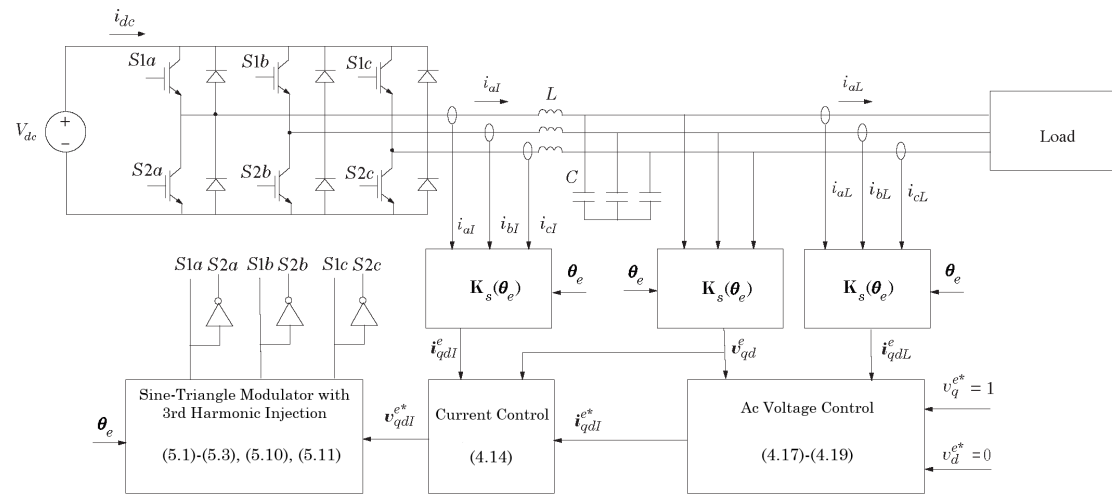


Fig. 5.1.: Detailed model of the source converter.

exceeds the triangle wave, the corresponding switch state becomes 1, and is otherwise 0. After applying the third harmonic injection, these duty cycles can be expressed

$$d_a = d \cos \beta - d_3 \cos 3\beta \quad (5.1)$$

$$d_b = d \cos \left(\beta - \frac{2\pi}{3} \right) - d_3 \cos 3\beta \quad (5.2)$$

$$d_c = d \cos \left(\beta + \frac{2\pi}{3} \right) - d_3 \cos 3\beta \quad (5.3)$$

Precluding overmodulation, the duty cycles are limited to values between 0 and 1. Consequently, the amplitude of the fundamental component of each duty cycle d must not exceed $2/\sqrt{3}$ and d_3 set to $d/6$. The moving temporal average of the line-to-neutral voltages applied to the filter will be of the form [33]

$$\hat{v}_{aI} = \frac{1}{2} dv_{dc} \cos \beta \quad (5.4)$$

$$\hat{v}_{bI} = \frac{1}{2} dv_{dc} \cos \left(\beta - \frac{2\pi}{3} \right) \quad (5.5)$$

$$\hat{v}_{cI} = \frac{1}{2} dv_{dc} \cos \left(\beta + \frac{2\pi}{3} \right) \quad (5.6)$$

where the moving temporal average is defined

$$\hat{v}_{xI} = \frac{1}{T} \int_{t-T}^T v_{xI}(\tau) d\tau \quad (5.7)$$

where $T = 1/f_{sw}$ is the switching period.

By setting β to $\theta_e + \phi_v$ and subsequently transforming these voltages into the synchronous reference frame, it can be seen that the temporal average of the q and d components of the voltages are

$$\hat{v}_{qI} = \frac{1}{2} dv_{dc} \cos \phi_v \quad (5.8)$$

$$\hat{v}_{dI} = -\frac{1}{2} dv_{dc} \sin \phi_v \quad (5.9)$$

For notational simplicity, the carrot will be omitted in subsequent equations.

Finally, the desired voltages expressed in (4.14) are used to determine d and ϕ_v by applying the following relationships:

$$d = \frac{2\sqrt{v_{qI}^2 + v_{dI}^2}}{v_{dc}} \quad (5.10)$$

$$\phi_v = \tan^{-1} \left(\frac{-v_{dI}}{v_{qI}} \right) \quad (5.11)$$

The duty cycle amplitude d and phase ϕ_v are then used to generate the three phase duty cycle waveforms and compared to the triangle wave to produce the inverter output voltages. In this work, to prevent overmodulation, the duty cycle is limited using a `sat` function similar to the one used in (4.18) and (4.19) to be less than or equal to $\sqrt{3}/3$ and greater than or equal to 0.

The switches in the inverter itself are considered to be ideal. The inverter subsystem takes the switch states generated by the modulator subsystem to determine the line-to-ground voltages in the inverter, v_{ag} , v_{bg} , and v_{cg} . To extract the line-to-neutral voltages, it is assumed that the sum of the abc voltages is zero, and that there is a voltage developed between the neutral point of the wye-connected capacitor bank and the bottom rail of the inverter, referred to as v_{ng} . By applying Kirchoff's Voltage Law, the following relationships can be established:

$$v_{ag} = v_{as} + v_{ng} \quad (5.12)$$

$$v_{bg} = v_{bs} + v_{ng} \quad (5.13)$$

$$v_{cg} = v_{cs} + v_{ng} \quad (5.14)$$

As noted previously, the carrot above each variable has been omitted. These equations can be summed, and since the line-to-neutral voltages v_{as} , v_{bs} , and v_{cs} sum to zero, it can be shown that

$$v_{ng} = \frac{v_{ag} + v_{bg} + v_{cg}}{3} \quad (5.15)$$

To express the line-to-neutral voltages in terms of line-to-ground voltages, (5.15) can be substituted into (5.12)-(5.14) to find:

$$v_{as} = 2/3v_{ag} - 1/3v_{bg} - 1/3v_{cg} \quad (5.16)$$

$$v_{as} = -1/3v_{ag} + 2/3v_{bg} - 1/3v_{cg} \quad (5.17)$$

$$v_{as} = -1/3v_{ag} - 1/3v_{bg} + 2/3v_{cg} \quad (5.18)$$

The remainder of the source model closely follows the equations represented in Chapter 4. The desired inverter output voltages are calculated from commanded current values, which are determined by (4.17). To calculate the commanded qd currents, the load currents i_{qdL} are measured, as well as the bus capacitor voltages v_{qd} , and these values are used in a feedback-feedforward controller. These commands are then limited by (4.18) and (4.19) to prevent overly large values of instantaneous current command.

In Chapter 4, the inverter was modelled as a current source, but it was noted that the behavior of the inverter controlled as a current-regulated voltage source converter was also discussed. In that discussion, it was assumed that the voltage sources could instantaneously take on the desired value to regulate inductor currents in the LC filter. In practice, however, if the controller gains are aggressive and there is significant ripple present on measured signals, the modulator signal d can undergo large ripple. The assumption that the duty cycle be smooth is integral in the derivation of the average-value model, and as such, filters are placed on the commanded qd inverter output voltages, and the gains were decreased by a factor of 2π to smooth the duty cycle signal in the detailed simulation. The bandwidth of these filters can be set to be large enough with respect to the closed-loop bandwidth of the current and voltage controllers so that they can be neglected in the average-value model while still having the desired effect in the detailed simulation.

The load was not considered to be ideal in the detailed simulation. Instead, an additional converter model was implemented with control set forth to ensure that the load emulated an ideal CPL. The current regulator for the load is defined in the same

fashion as the current regulator of the source, taking the right hand side of (4.21) as commanded current values after converting from per-unit to SI units. The load current commands in SI units are

$$\begin{bmatrix} i_{qL}^* \\ i_{dL}^* \end{bmatrix} = \frac{2}{3} \frac{1}{v_q^2 + v_d^2} \begin{bmatrix} v_q & -v_d \\ v_d & v_q \end{bmatrix} \begin{bmatrix} P \\ Q \end{bmatrix} \quad (5.19)$$

The commanded currents are then fed into a controller to generate commanded rectifier input voltages. The controller is of the same form as (4.14), replacing source inverter currents with load rectifier currents. The load rectifier voltage commands \mathbf{v}_{qdR}^* can be expressed

$$\mathbf{v}_{qdR}^* = k_{pR}(\dot{\mathbf{i}}_{qdL}^* - \dot{\mathbf{i}}_{qdL}) + \mathbf{v}_{qd} + \omega_e L_{\text{load}} \begin{bmatrix} 0 & 1 \\ -1 & 0 \end{bmatrix} \mathbf{i}_{qdL} \quad (5.20)$$

An identical modulator is used, as well as an identical inverter model with ideal switches. Since the load currents are used to generate current commands in the source, a filter inductor is added to each phase of the load to ameliorate switching effects that may have a detrimental impact on the measured value of the load currents. With the inclusion of the load-side inductors, the system order has increased from 4 to 6. Additionally, the bandwidth of the load is now limited by these inductors, while no bandwidth limitations were placed on the load in the average-value model. However, with a fast switching frequency implemented on the load, a very large bandwidth is achievable in the load, and so this nonideality is neglected. A diagram of the load model can be seen in Figure 5.2.

While the average-value model was simulated in per unit, the detailed model was simulated using SI units. The per unit bases and simulation parameters are listed in Table 5.1.

5.2 Simulation results

To validate the average-value model used to generate the regions of interest to determine the large-displacement stability of the source, average-value model and de-

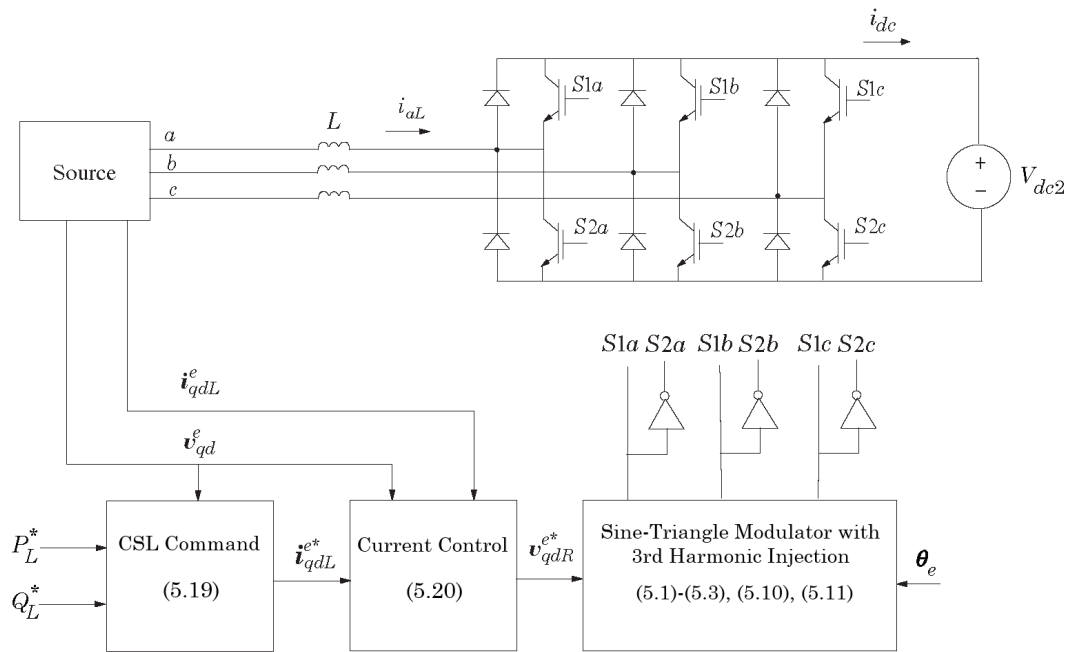


Fig. 5.2.: A diagram of the detailed load model

Table 5.1.: Simulation parameters and per unit bases

Parameter	Value (unit)
P_{base}	1 (kW)
V_{base}	$120\sqrt{2}$ (V_{peak} , line to neutral)
I_{base}	3.9284 (A)
ω_e	$2\pi 60$ (rad/s)
f_{sw}	50 (kHz)
L_{source}	1.5 (mH)
L_{load}	750 (μH)
C	12.25 (μF)
i_{lim}	5.8926 (A)

tailed simulations were exercised over the same load profile. The system is initialized to no load, and at 0.02 seconds, the load is stepped to $P = 0.5$ pu, $Q = 0$ pu. At 0.03 seconds, the load is changed to $P = 0$ pu, $Q = 0.5$ pu, and finally at 0.035 seconds, the load is stepped to $P = \sqrt{2}/4$ pu, $Q = -\sqrt{2}/4$ pu.

It is noted, however, that within the detailed model, there is significant ripple on the duty cycle signal used in the sine-triangle modulator. Though there is good agreement between the average-value model and the detailed model, the derivation of the average-value model is dependent on a duty cycle that does not change significantly over a switching period. As noted previously, to limit changes in the duty cycle, a low-pass filter with bandwidth 50 krad/sec was introduced on the q - and d -axis inverter output voltage command signals used to generate the duty cycle, and the proportional gains in the voltage and current regulator loops were decreased by a factor of 2π , bringing the closed-loop bandwidth of the control loops to be 795.77 radians per second and 79.577 radians per second.

In a practicable converter, it is necessary to filter the inverter output voltage commands to prevent large ripple in the duty cycle of the sine-triangle modulator. The results discussed in Chapter 4 therefore require extension. The numerical values obtained for controller gains are still achievable, though higher switching frequencies are required. Gains such as those described by (4.20) can be expressed in terms of filter bandwidth rather than switching frequency in radians per second.

A comparison of the duty cycle signal in the detailed simulation the simulation without the filter and in the simulation with filters (and decreased gains) can be seen in Figure 5.3. These changes significantly reduce duty cycle ripple, though the transient behavior takes somewhat longer to settle out. Since the dynamics have been changed, it is necessary to not only reestablish the RLDS and RSS, but to determine whether the inclusion of two additional states has any significant impact on the dynamics of the system. The results from the detailed simulation with the additional states are compared to the average-value model simulation results without the inclusion of the additional states in Figures 5.4 through 5.7. As can be seen

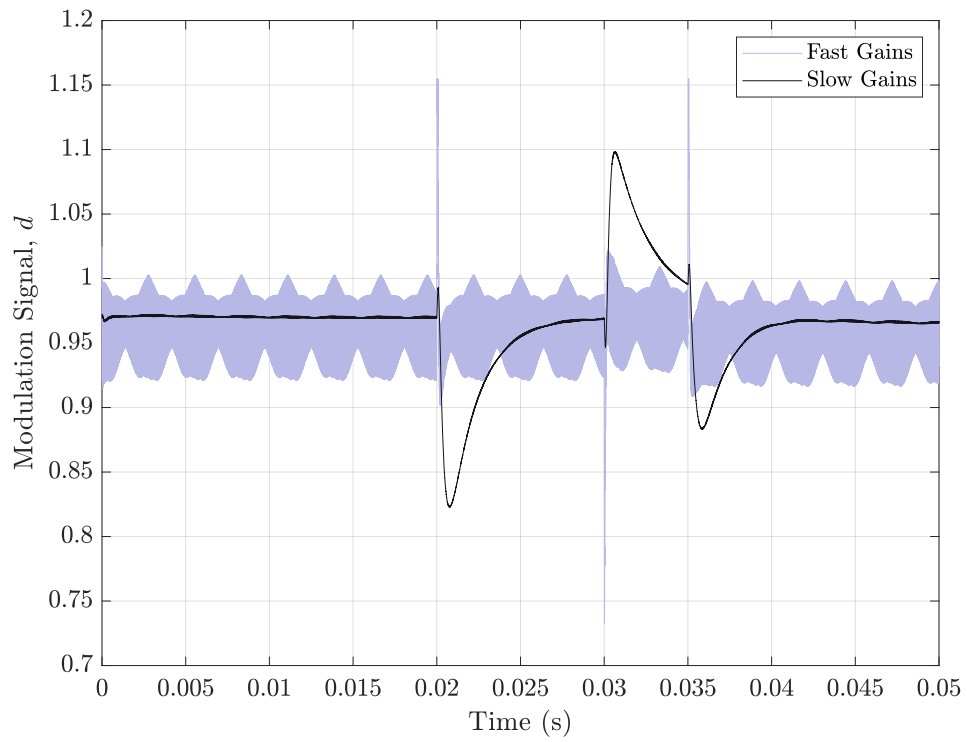


Fig. 5.3.: A comparison of the duty cycle signal, d , in detailed simulations.

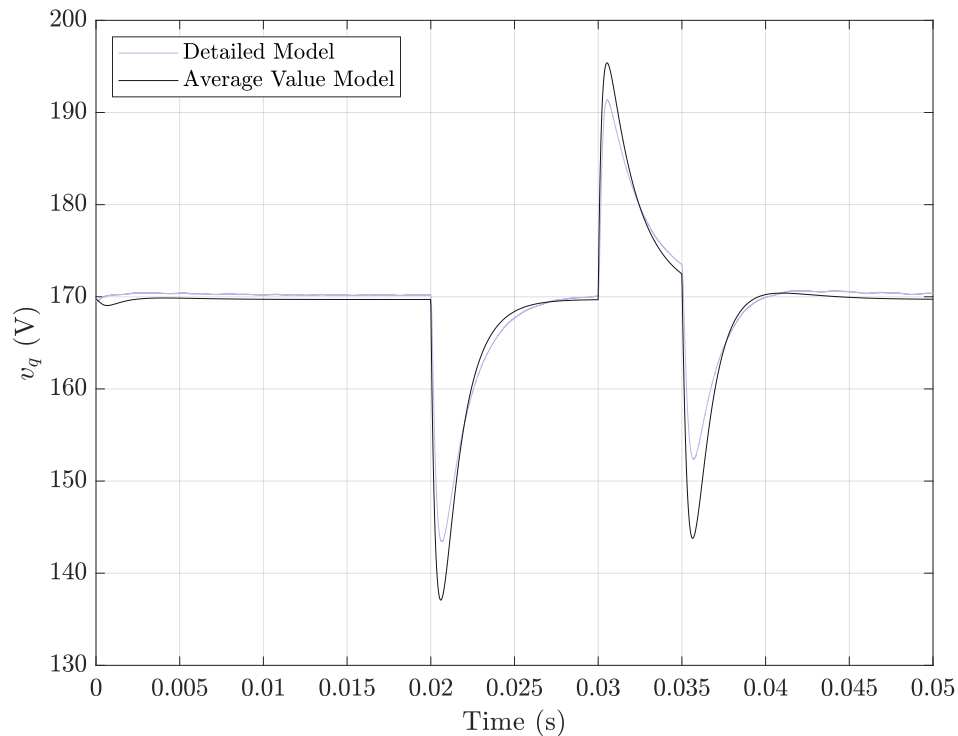


Fig. 5.4.: Comparison of q -axis voltage results from average-value model and detailed simulation including voltage command filters and reduced controller gains.

in these figures, there is generally good agreement between the detailed simulation with additional states and the average-value model without inclusion of the command filters. This is due to the bandwidth of the command filter being so much higher than the fastest control loops.

While the transient behavior of the q -axis voltage in the detailed simulation generally corresponds to the average-value model results, there is a slight difference in the peak and minimum voltages during transients. For the load stepped at 0.035 seconds, there is a difference of 8.6 V, or 0.0507 pu. The steady-state value is within fractions of a volt, and so this small difference is neglected.

Similarly, there are small discrepancies between average-value model and detailed simulation results in the d -axis voltage. The peak difference after the load step at

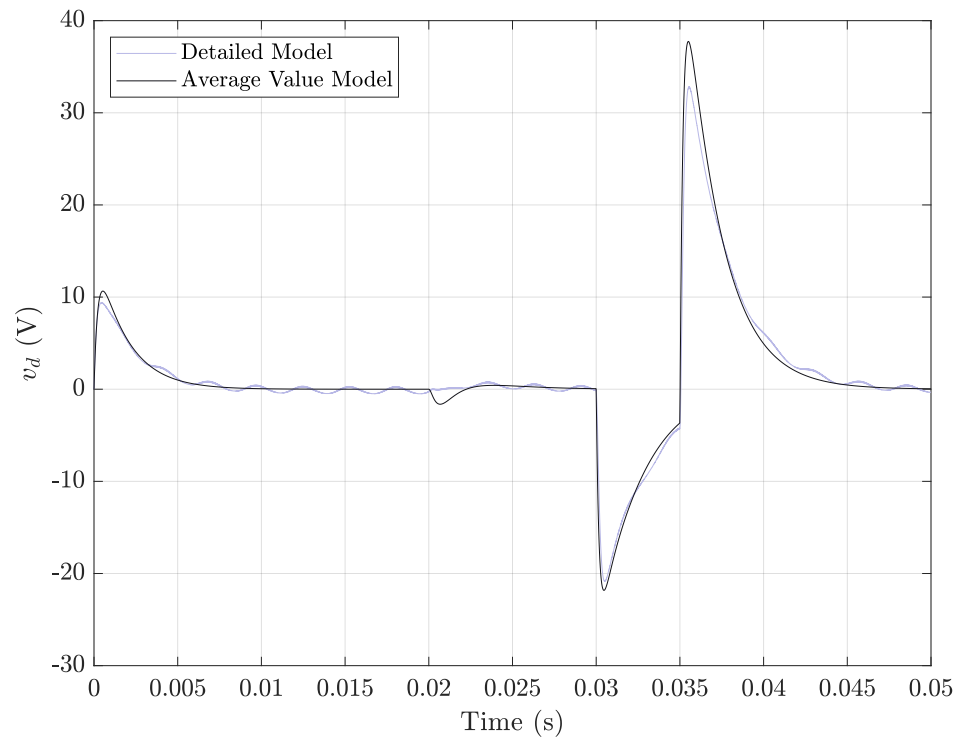


Fig. 5.5.: Comparison of d -axis voltage results from average-value model and detailed simulation including voltage command filters and reduced controller gains.

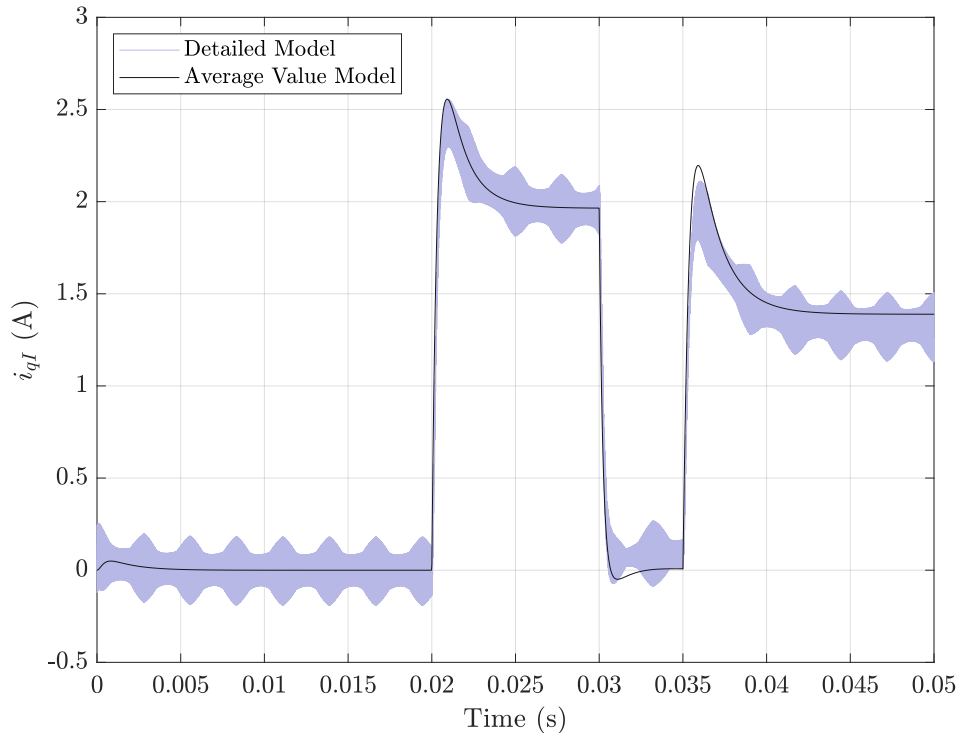


Fig. 5.6.: Comparison of q -axis current results from average-value model and detailed simulation including voltage command filters and reduced controller gains.

0.035 seconds is 4.91 volts, or 0.0289 pu. It can also be seen that the low frequency oscillation present in the original simulation is still present, though greatly reduced in magnitude.

It is difficult to determine the error between the peaks of the currents due to the ripple present on the signals from the detailed simulation. The absolute peaks can be compared for the load step at 0.035 seconds, where the difference is 0.085 A, or 0.0216 pu, but this difference is smaller than the steady-state ripple. For this reason, to conservatively estimate error between the average-value model and detailed simulation, rather than compare differences in peak transient values, the peak ripple present in the detailed model is compared. The peak ripple on the q -axis current is 0.188 A, which is 0.0479 pu.

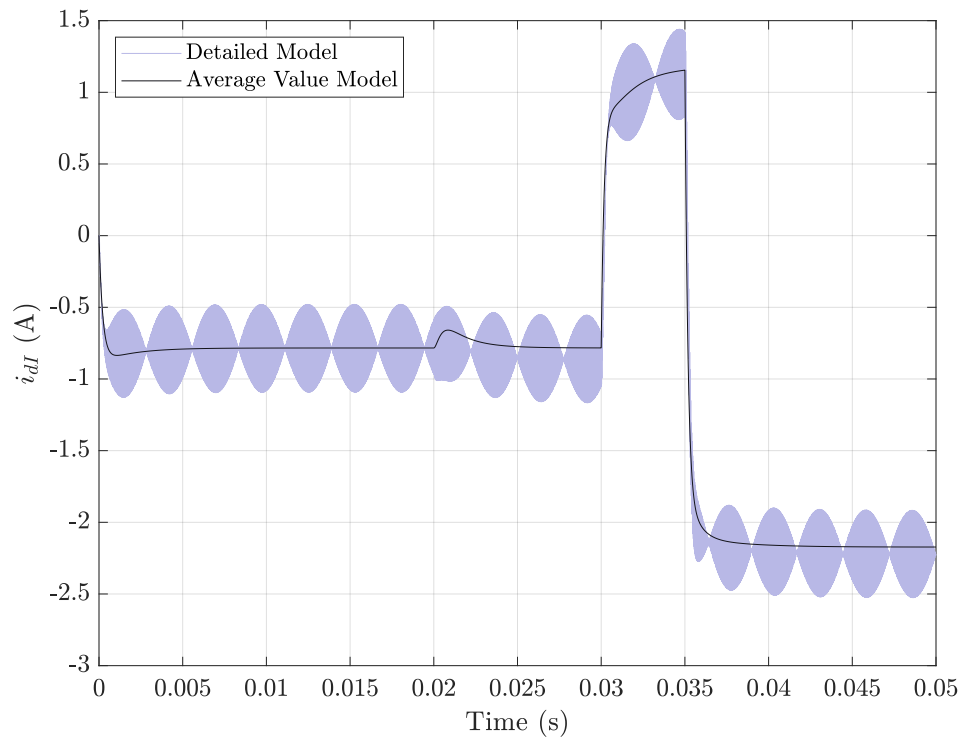


Fig. 5.7.: Comparison of d -axis current results from average-value model and detailed simulation including voltage command filters and reduced controller gains.

The d -axis current does not undergo overshoot in either simulation, error between detailed and average value simulations is expressed in terms of steady-state ripple. The peak ripple of the d -axis current is 0.244 A, or 0.0776 pu. To estimate the peak error between the average-value model and detailed model, the norm of the errors between voltage peaks and peak current ripples is taken, and is calculated to be 0.1083 pu.

Since the parameters of the system have changed, it is necessary to reestablish the RLDS, RSS, and LDSM. Since the average-value model captures the salient features of the detailed simulation results without including additional states from the voltage command filters or finite load bandwidth, the same procedure set forth in Chapter 4 can be used. The RLDS is established by initializing the two currents and the voltage angle in the v_q - v_d plane, and performing a linear search along the magnitude of the qd voltages for the minimum necessary magnitude to maintain stability for a real power load of 0.5 pu. The RSS was established using Algorithms 3 and 4 with search parameters shown in Table 5.2.

It can be seen in Figure 5.8 that the RLDS boundary rises higher along the v_q axis and the RSS encloses a larger space than what was enclosed previously. The maximum error between the estimated boundary of the RSS and the true boundary is 0.0256 pu, and the LDSM was recalculated, and found to be 0.1851 pu assuming the RSS boundary is exact. Subtracting the RSS boundary error from the LDSM estimate, the LDSM is minimally 0.1595. Since the LDSM is larger than the error between detailed and average-value model simulations, the system studied in this research can be claimed to be Large-Displacement Stable.

The capacitor voltages from the detailed simulation can be seen in Figure 5.9. It can be seen that the voltage is smooth relative to the currents and that the voltage recovers quickly from perturbations. The resonant frequency of the source-side inductor and the bus capacitor is 7.377 kHz, which is low enough to eliminate the majority of switching effects on the voltage.

Table 5.2.: RSS search parameters for the 50 kHz system with relaxed gains

Parameter	Value
N_{i_q}	70
N_{i_d}	70
N_{v_q}	60
N_{v_d}	60
$i_{qI,\max}$ (pu)	1
$i_{qI,\min}$ (pu)	-0.5
$i_{dI,\max}$ (pu)	0.8
$i_{dI,\min}$ (pu)	-1.2
$v_{q,\max}$ (pu)	1.5
$v_{q,\min}$ (pu)	0.7
$v_{d,\max}$ (pu)	0.8
$v_{d,\min}$ (pu)	-0.8

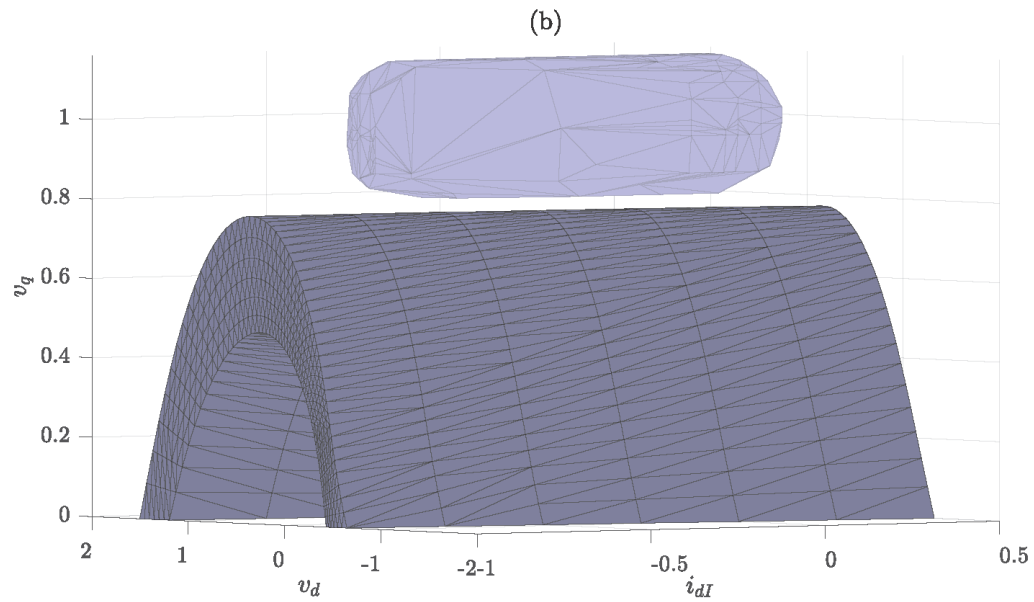
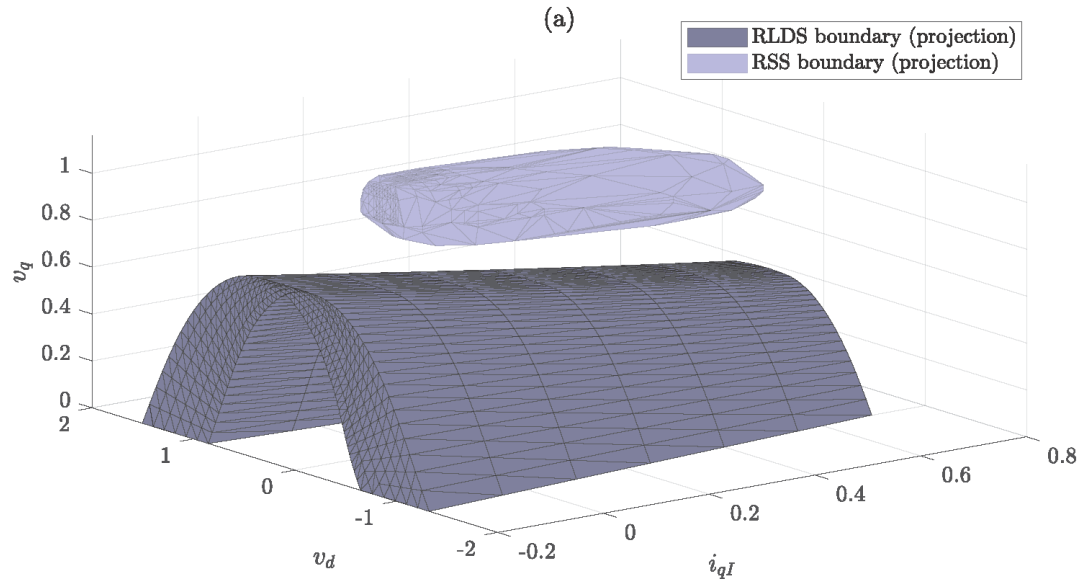


Fig. 5.8.: Projections of the RLDS and RSS projected into (a) i_{qI}, v_d, v_q space and (b) i_{dI}, v_d, v_q space.

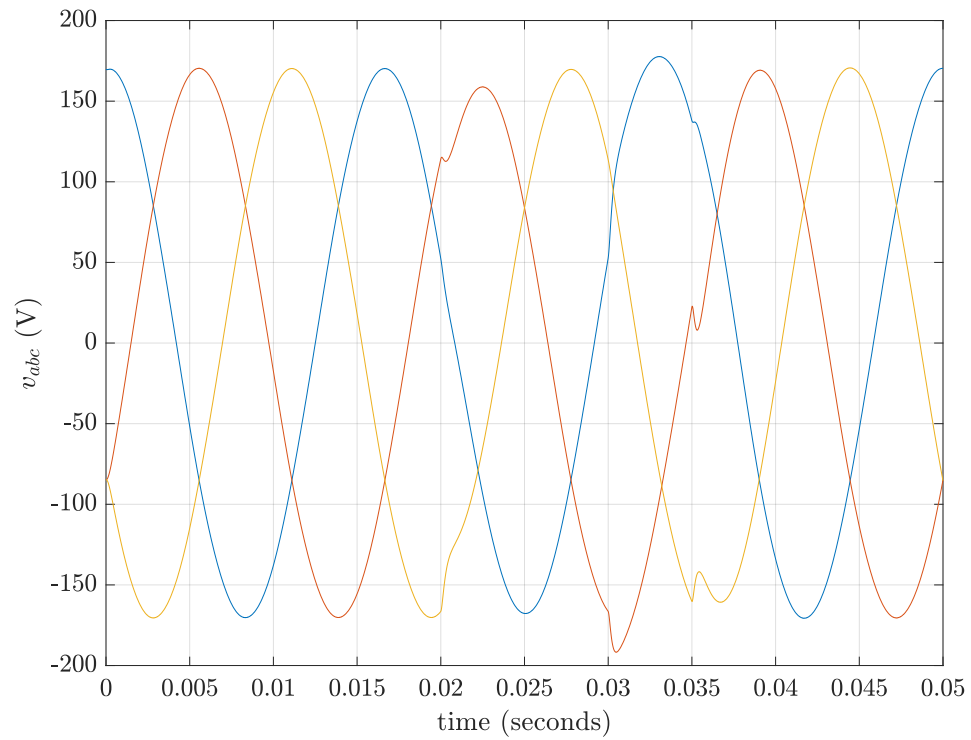


Fig. 5.9.: Ac bus capacitor voltages in physical (abc) variables during load transients.

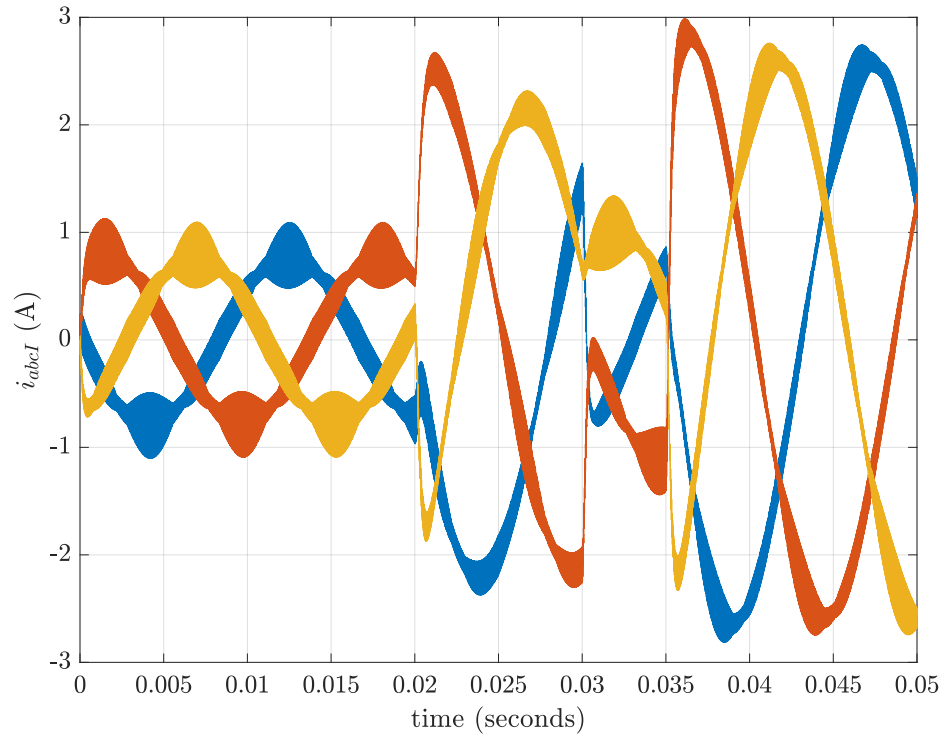


Fig. 5.10.: Inverter output currents in physical (abc) variables during load transients

The inverter output currents from the detailed simulation can be seen in Figure 5.10. It can be seen that there is a large ripple component on the current, though it is small. Additionally, because the capacitor bank sources reactive power, there is a component of current flowing prior to the first load step. Inspecting Figures 5.9 and 5.10, it can be seen that the currents are 90 degrees ahead of the voltage, corresponding to the source sinking reactive power.

The load commands in the detailed simulation are not immediately met, since the load is modelled as having finite bandwidth. Figures 5.11 through 5.13 show the load currents in abc variables as they change with respect to their commands. It can be seen that the currents closely match the commanded values over time, though there is ripple on the currents. The ripple is worse on the load currents than on the source currents due to the smaller inductor used on the load side of the LCL filter.

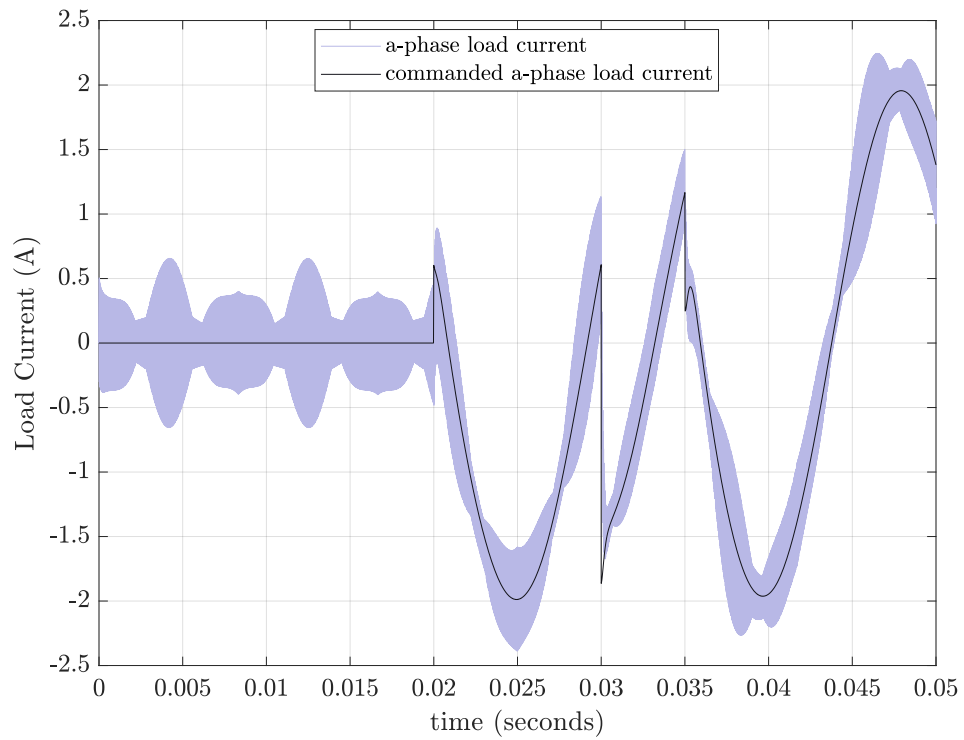


Fig. 5.11.: The a -phase load current and commanded load current.

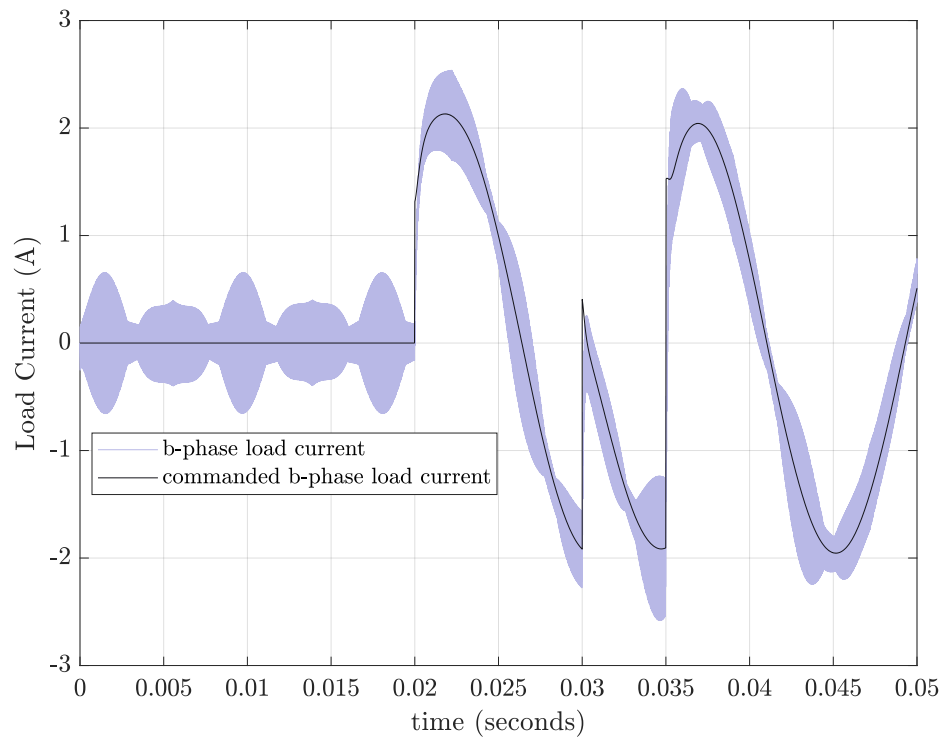


Fig. 5.12.: The *b*-phase load current and commanded load current.

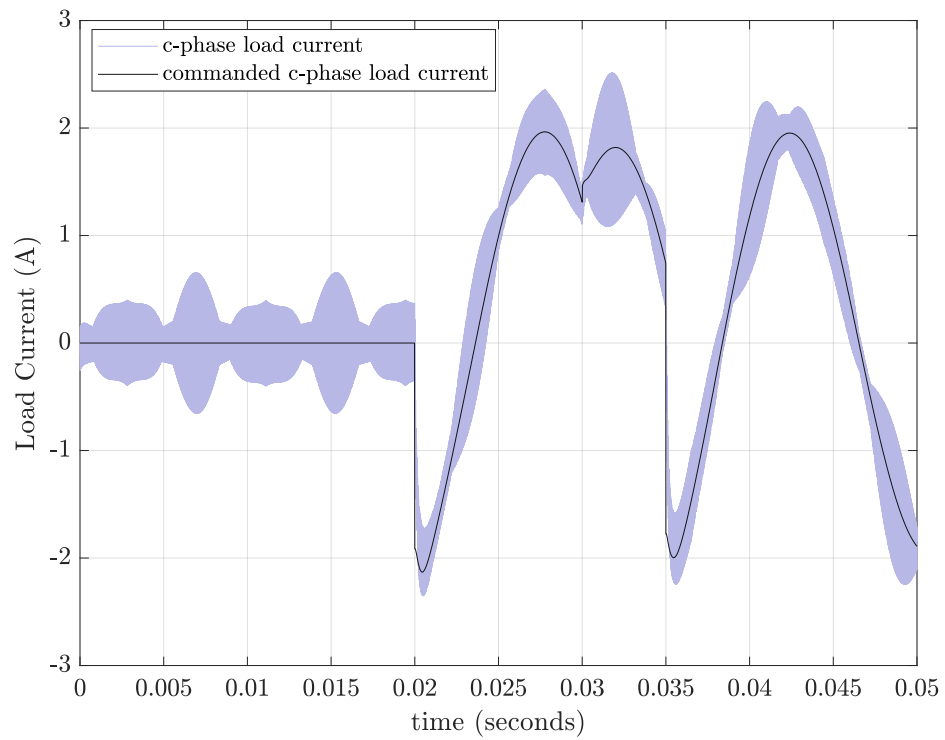


Fig. 5.13.: The c -phase load current and commanded load current.

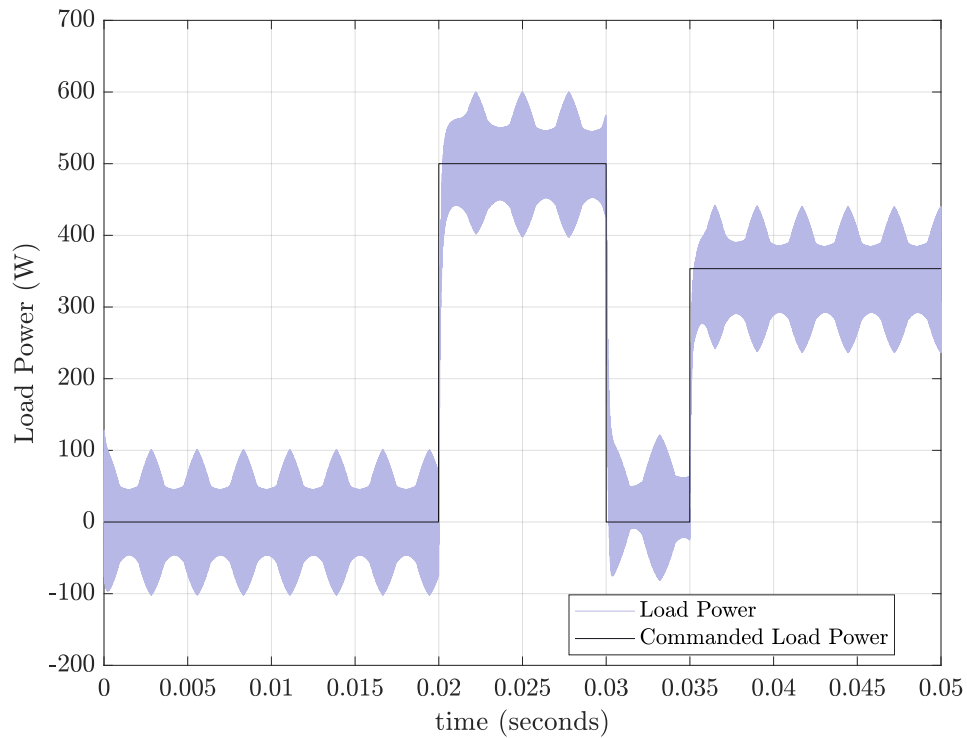


Fig. 5.14.: Simulated and commanded real power consumed by the load.

Finally, the real and reactive power consumed by the load in the detailed simulation are compared to the commanded real and reactive power in Figures 5.14 and 5.15. Since the current undergoes so much ripple, the real and reactive power consumed by the load also includes ripple comparable to the currents. If it were desired to limit the power ripple, larger inductances could be used in the *LCL* filter.

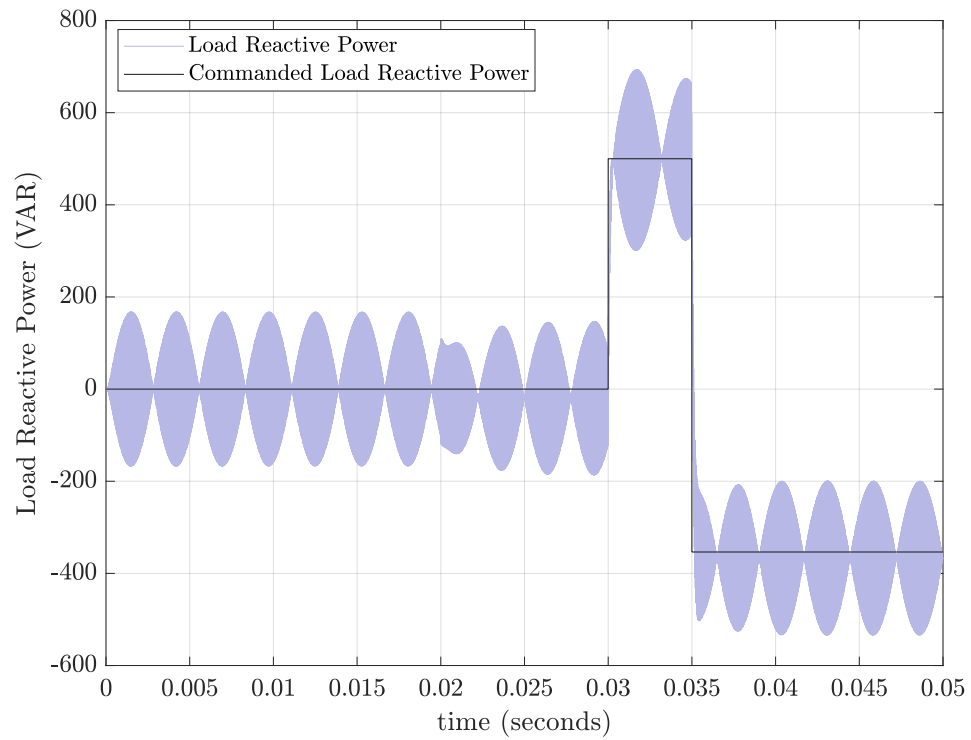


Fig. 5.15.: Simulated and commanded reactive power consumed by the load.

6. SUMMARY, CONCLUSIONS, AND AREAS OF FUTURE RESEARCH

In this chapter, key results and conclusions are summarized and suggested areas of future research are provided.

6.1 Summary and Conclusions

In this research, a definition of Large-Displacement Stability (LDS) was set forth along with a criteria to determine whether or not a system is LDS. A state trajectory of a system that is LDS will always asymptotically approach the equilibrium point for any arbitrary change in input at any arbitrary time as long as the input remains within predetermined bounds. The criteria was applied for several candidate systems, including: (1) a simple two-dimensional dc system consisting of a current source and bus capacitor feeding a constant-power load, (2) an extension of that system that replaces the current source with a permanent-magnet synchronous generator controlled by an active rectifier, and (3) a three-phase current source and wye-connected capacitor bank feeding a constant-apparent-power load.

Each system was designed by selecting a switching frequency, bus capacitance, and transient overload capacity that ensures LDS. The switching frequency was used to select controller gains to place closed-loop poles in the complex plane at decades below the switching frequency. Each parameter was selected to be a practicable value based on readily available components and achievable switching frequencies.

Once system parameters were selected for each system, Regions of Asymptotic Stability (RAS) were established for a wide range in loads. The RAS's were established by a brute force search for, given $n - 1$ fixed values of a state, the minimum necessary value of the remaining state for a trajectory to maintain stability for a fixed

load. Once each RAS was established, they were overlaid to show the Region of Large-Displacement Stability (RLDS). Once it was shown that the RLDS was nonempty and contained the set of equilibrium points, the system was said to be Single-Step Stable.

A recursive, brute-force search algorithm was used to estimate the Reachable State Space (RSS) of a given system. The algorithm consists of first initializing the system to a fixed point in the set of equilibrium points, applying a wide range of inputs, and allowing each ensuing state trajectory to evolve using a fixed-step numerical solver until it arrives at its new respective equilibrium point. Once each trajectory arrives at its equilibrium point, the algorithm goes up a layer of recursion and applies a new input to generate a new trajectory. This procedure continues until all inputs have been applied at all points along all trajectories. The state space is discretized into n -dimensional domains, and domains through which trajectories travel are marked with a logical 1. If the RSS is not bounded, the algorithm finds a combination of inputs to drive the system unstable. If the RSS is bounded, the algorithm terminates and the domains that have been marked 1 are plotted. A maximum error between the true boundary of the RSS and the estimated boundary was determined based on the size of each domain.

The boundaries of the RLDS and the RSS were compared to establish a Large-Displacement Stability Margin (LDSM) by taking the minimum distance between the two boundaries. This LDSM was maximized in the ac system by selecting parameters that would result in the lowest necessary q -axis voltage to maintain stability.

In the case of the ac system, the Belkhat Criteria was evaluated to show that the system satisfies what is considered a conservative small-displacement stability criterion by more than an order of magnitude. Though not a sufficient nor a necessary condition for large-displacement stability, evaluating the Belkhat criteria gives a sense of system robustness.

The ac system results were also validated using a detailed simulation. The current-source model used to determine RAS's and the RSS was compared to a voltage source inverter controlled to have dynamics similar to the current source. The detailed sim-

ulation also incorporates nonideal load characteristics, such as switching effects from the active rectifier controlled to appear as a constant-power load. In the transition of the source and load models from a nonideal current source and ideal CPL to a voltage source converter and switched load, filter inductances and controller gains were selected to limit the ripple introduced by the switching converters. Practicable values were selected, and the error introduced due to switching transients was quantified and shown to be small with respect to the LDSM found in the analysis of the average-value model.

6.2 Hardware Implementation

Detailed simulation results generated in this thesis closely match results generated with average-value model simulations. Though a high degree of confidence is held in the simulation results, it is desirable to implement the ac system studied in this work in a lab setting to further validate the average-value models used to establish the RSS, RLDS, and LDSM of the ac system.

6.3 Improved Algorithms for Estimating Regions of Interest

Brute force search techniques are computationally intensive, and improvements can be made to determine both the RLDS and RSS using searches based on boundary conditions. This approach can be more efficient, as well as more accurate. For example, to establish the RSS, a “front of points” can be defined to tightly wrap the equilibrium set, and the state derivative can be evaluated at each point for a range of inputs. The front is advanced based on the magnitude and direction of the allowable state derivative at each point until the state derivatives are tangential to the boundary or points inside the boundary at each point. This method has recently been implemented in a two-dimensional system [35], and yields similar results to the recursive search, but with a smoother boundary. This work can be extended to higher dimensional systems.

Similarly, the RAS associated with an equilibrium point can be established with a similar advancing front. Where the RSS boundary is the boundary on which each state derivative is tangential or points inside and encloses the smallest area, the RAS boundary is the boundary on which the one state derivative vector is tangential and encloses the largest possible area. Whereas the advancing front in the RLDS case stops when the derivative condition is satisfied, the front in the RAS search would continue until the state derivative begins to point outside the of enclosed space.

6.4 Higher Dimensional Systems

It is of interest to extend the results to higher dimensional systems. With more efficient search algorithms, establishing the regions of interest for microgrids with multiple sources and loads will become possible. The challenges in interpreting 4-dimensional results are exacerbated in higher dimensional systems, including understanding of the projections of higher dimensional spaces into 2 or 3 dimensions.

6.5 Examining Load Characteristics

It is of interest to determine if a non-LDS system can be made LDS by imposing bandwidth constraints on the input. Achieving Large-Displacement Stability in a microgrid might not be possible for some systems if the load is modelled as a large constant-power step input. However, physical loads do change instantaneously in general, and therefore it is desirable to understand the impact that a non-zero rise time on the input might have on the LDS of the system as a whole. A designer may also be forced to impose bandwidth limitations on the load if the requirements on the source are too restrictive, and so it is of interest to establish the trade between source and load bandwidths.

REFERENCES

REFERENCES

- [1] J. Carrol, "An input impedance stability criterion allowing more flexibility for multiple loads which are independently designed," *Naval Air Warfare Center, Aircraft Division, Indianapolis, B/812*, 1992.
- [2] S. D. Sudhoff, S. F. Glover, P. T. Lamm, D. H. Schmucker, and D. E. Delisle, "Admittance space stability analysis of power electronic systems," *IEEE Transactions on Aerospace and Electronic Systems*, vol. 36, no. 3, pp. 965–973, Jul 2000.
- [3] M. Gries, O. Wasynczuk, B. Selby, and P. T. Lamm, "Designing for large-displacement stability in aircraft power systems," *SAE International Journal of Aerospace*, vol. 1, no. 1, pp. 894–902, nov 2008. [Online]. Available: <https://doi.org/10.4271/2008-01-2867>
- [4] A. Riccobono and E. Santi, "Comprehensive review of stability criteria for dc power distribution systems," *IEEE Transactions on Industry Applications*, vol. 50, no. 5, pp. 3525–3535, Sept 2014.
- [5] M. Belkhat, "Stability criteria for ac power systems with regulated loads," Ph.D. dissertation, Purdue University, 1997.
- [6] M. Belkhat and O. Wasynczuk, "Stability analysis of ac power systems with regulated electronic loads," SAE Technical Paper, Tech. Rep., 1998.
- [7] S. D. Sudhoff, K. A. Corzine, S. F. Glover, H. J. Hegner, and H. N. Robey, "Dc link stabilized field oriented control of electric propulsion systems," *IEEE Transactions on Energy Conversion*, vol. 13, no. 1, pp. 27–33, March 1998.
- [8] S. D. Sudhoff, S. Pekarek, B. Kuhn, S. Glover, J. Sauer, and D. Delisle, "Naval combat survivability testbeds for investigation of issues in shipboard power electronics based power and propulsion systems," in *IEEE Power Engineering Society Summer Meeting*, vol. 1, July 2002, pp. 347–350 vol.1.
- [9] R. D. Middlebrook and S. Cuk, "A general unified approach to modelling switching-converter power stages," in *1976 IEEE Power Electronics Specialists Conference*, June 1976, pp. 18–34.
- [10] K. Ogata, *Modern control engineering*, 5th ed., ser. Instrumentation and controls series. Boston, MA: Prentice-Hall, 2010.
- [11] S. D. Sudhoff, "Dc system stability and the the dc stability toolbox," in *2017 IEEE Electric Ship Technologies Symposium (ESTS)*, Aug 2017, pp. 1–56.

- [12] C. M. Wildrick, F. C. Lee, B. H. Cho, and B. Choi, "A method of defining the load impedance specification for a stable distributed power system," in *Power Electronics Specialists Conference, 1993. PESC '93 Record., 24th Annual IEEE*, Jun 1993, pp. 826–832.
- [13] X. Feng, Z. Ye, K. Xing, F. C. Lee, and D. Borojevic, "Impedance specification and impedance improvement for dc distributed power system," in *30th Annual IEEE Power Electronics Specialists Conference. Record. (Cat. No.99CH36321)*, vol. 2, 1999, pp. 889–894 vol.2.
- [14] —, "Individual load impedance specification for a stable dc distributed power system," in *Applied Power Electronics Conference and Exposition, 1999. APEC '99. Fourteenth Annual*, vol. 2, Mar 1999, pp. 923–929 vol.2.
- [15] X. Feng, J. Liu, and F. C. Lee, "Impedance specifications for stable dc distributed power systems," *IEEE Transactions on Power Electronics*, vol. 17, no. 2, pp. 157–162, Mar 2002.
- [16] S. D. Sudhoff and J. M. Crider, "Advancements in generalized immittance based stability analysis of dc power electronics based distribution systems," in *2011 IEEE Electric Ship Technologies Symposium*, April 2011, pp. 207–212.
- [17] X. Wang, R. Yao, and F. Rao, "Three-step impedance criterion for small-signal stability analysis in two-stage dc distributed power systems," *IEEE Power Electronics Letters*, vol. 1, no. 3, pp. 83–87, Sept 2003.
- [18] A. Riccobono and E. Santi, "A novel passivity-based stability criterion (pbsc) for switching converter dc distribution systems," in *2012 Twenty-Seventh Annual IEEE Applied Power Electronics Conference and Exposition (APEC)*, Feb 2012, pp. 2560–2567.
- [19] W. Li, J. Llibre, and X. Zhang, "Extension of floquet's theory to nonlinear periodic differential systems and embedding diffeomorphisms in differential flows," *American Journal of Mathematics*, vol. 124, no. 1, pp. 107–127, 2002. [Online]. Available: <http://www.jstor.org/stable/25099108>
- [20] C.-T. Chen, *Linear system theory and design*, 3rd ed., ser. Oxford series in electrical and computer engineering. New York: Oxford University Press, 1999.
- [21] I. Postlethwaite, J. Edmunds, and A. MacFarlane, "Principal gains and principal phases in the analysis of linear multivariable feedback systems," *IEEE Transactions on Automatic Control*, vol. 26, no. 1, pp. 32–46, February 1981.
- [22] B. P. Loop, "Estimating regions of asymptotic stability of nonlinear systems with applications to power electronics systems," 2005.
- [23] D. Karimipour and F. R. Salmasi, "Stability analysis of ac microgrids with constant power loads based on popov's absolute stability criterion," *IEEE Transactions on Circuits and Systems II: Express Briefs*, vol. 62, no. 7, pp. 696–700, July 2015.
- [24] L. J. Rashkin, "Large-displacement stability of ac microgrids," Ph.D. dissertation, Purdue University, 2014.

- [25] S. H. Zak, *Systems and control*. Oxford University Press New York, 2003, vol. 174.
- [26] O. de Oliveira, “The implicit and inverse function theorems: Easy proofs,” *Real Anal. Exchange*, vol. 39, no. 1, pp. 207–218, 2013. [Online]. Available: <https://projecteuclid.org:443/euclid.rae/1404230147>
- [27] B. P. Loop, S. D. Sudhoff, S. H. Zak, and E. L. Zivi, “Estimating regions of asymptotic stability of power electronics systems using genetic algorithms,” *IEEE Transactions on Control Systems Technology*, vol. 18, no. 5, pp. 1011–1022, 2010.
- [28] O. Wasynczuk, T. Craddock, J. Thompson, and C. Miller, “Ensuring large-displacement stability in aircraft and shipboard dc power systems,” in *2019 IEEE Electric Ship Technologies Symposium (ESTS)*, Submitted, pp. –.
- [29] M. Althoff and N. Kochdumper, *CORA 2018 Manual*, Technische Universität München.
- [30] H. Villegas Pico, “Advances to the dynamic analysis of power converter-based systems under uncertainty: A reachability approach,” Ph.D. dissertation, Purdue University, 2016.
- [31] H. N. Villegas Pico, “Advances to the dynamic analysis of power converter-based systems under uncertainty: A reachability approach,” 2016.
- [32] H. N. V. Pico and D. C. Aliprantis, “Voltage ride-through capability verification of dfig-based wind turbines using reachability analysis,” *IEEE Transactions on Energy Conversion*, vol. 31, no. 4, pp. 1387–1398, Dec 2016.
- [33] P. C. Krause, *Analysis of electric machinery and drive systems*, 3rd ed., ser. IEEE Press series on power engineering ; 75. Wiley, 2013.
- [34] J. J. Grainger, *Power system analysis*, ser. McGraw-Hill series in electrical and computer engineering. Power and energy. New York: McGraw-Hill, 1994.
- [35] C. Olthoff, “Computation of large-displacement stability metrics in dc power systems,” Master’s thesis, Purdue University, 2019.

APPENDICES

A. SEARCH ALGORITHM

Computer simulations were constructed for each system to search for the RAS's of different input loads. The simulations were exercised at an array of points to establish the RAS for a given load.

In the case of the 3-phase ac system, the 4-dimensional RAS was established by sweeping initial conditions in the converter's synchronous reference frame, and checking if the state vector returns to the equilibrium point. The states which are being checked are the q - and d -axis capacitor voltages and the q - and d -axis source currents.

The initial conditions were swept in nested for-loops. First, the q - and d -axis currents were initialized to fixed values. After the currents were initialized, the voltages were initialized. Searching the space in a grid is computationally intensive, and can fall short of finding the entire boundary. For smaller slices of the RAS, it is necessary to begin searching at a relatively large value of v_d in order to establish the full boundary. As the slices grow, however, the boundary falls closer and closer to the origin, and so starting with a large v_d wastes time. And so, rather than sweep voltage initial conditions in a Cartesian grid, the voltages were transformed into polar coordinates, and a linear search for the PRAS boundary was performed using the bisection method. That is to say, a line was defined between the origin of the v_q - v_d plane and some fixed point away from the origin along a certain angle with respect to the positive v_d axis is defined as θ . A bisection-search is performed along that line for a fixed number of iterations, and the resulting point is then transformed back into Cartesian coordinates and stored in a matrix along with the initial currents. The angle is then incremented, and the search is performed again. This search is performed at a fixed number of different angles, ranging from 0 to π radians. This search was noticed to be much more efficient than sweeping Cartesian coordinates, and can find the point

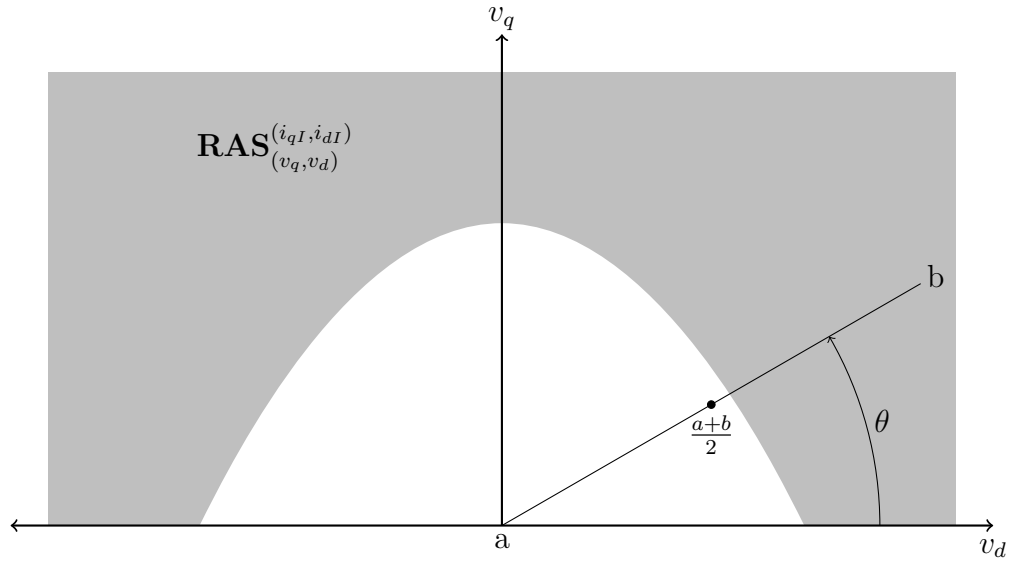


Fig. A.1.: Visualization of the linear search being performed

on the PRAS curve within an accuracy proportional to $2^{(n-1)}$, where n is the number of bisections performed. After finding all of the initial voltages that comprise the curve, the currents are incremented, and the search begins again.

VITA

VITA

Thomas Craddock received his BSECE and MSECE from Purdue University in the Spring of 2014 and the Fall of 2015, respectively. He taught and helped to rebuild the electromechanical motion devices laboratory for undergraduates for four years while in the graduate program, for which he received the Magoon Award for Excellence in Teaching and the Teaching Academy Graduate Teaching Award, as well as being nominated by the College of Engineering for the Graduate School Excellence in Teaching Award. He has interned at John Deere Electronic Solutions and PC Krause & Associates, and is currently pursuing his Ph.D. in Electrical and Computer Engineering at Purdue.

Thomas' research interests include microgrid stability, microgrid control, and high-frequency characterization of power electronic and motor drive systems.